An Assessment of U(VI) Adsorption at Multiple Scales

by

Vijay Anand Loganathan

A dissertation submitted to the Graduate Faculty of
Auburn University
in partial fulfillment of the
requirements for the Degree of
Doctor of Philosophy

Auburn, Alabama
December 13, 2010

Keywords: Adsorption, Uranium, Scaling, Surface Complexation Modeling,
Iron oxide-coated sand, Biochar

Approved by

Mark O. Barnett, Chair, Professor of Civil Engineering
T. Prabhakar Clement, Professor of Civil Engineering
Yucheng Feng, Associate Professor of Agronomy and Soils
Ahjeong Son, Assistant Professor of Civil Engineering

Abstract

Iron (III) (oxyhydr)oxide coatings on soils and sediments are one of the most important factors in controlling the adsorption and transport of U(VI) in the subsurface. In this study, iron-coated sands were prepared via two common protocols, a precipitation method, where Fe was precipitated directly onto the sand in a single step, and an adsorption method, where pure goethite was prepared in the first step and then adsorbed onto the sand in a second step (Chapter 2). The coated sands from both the systems were characterized using scanning electron microscopy, energy dispersive spectroscopy, x-ray diffraction, and selective Fe extraction. Although neither of the methods produced a completely crystalline Fe coating, the precipitation method produced sands with larger portions of amorphous Fe than the adsorption method, with the fraction of amorphous Fe decreasing with increasing Fe content.

U(VI) adsorption isotherms and pH adsorption edges were measured on three coated sands with Fe contents ranging from 0.04 to 0.3% (Chapter 3). Experimentally, the adsorption of U(VI) onto the three sands was more comparable when normalized to surface area than when normalized to Fe content. A surface complexation model, although originally developed for U(VI) adsorption onto amorphous Fe oxide, captured the differences in adsorption when adjusted for the surface area of the coated sand.

One of the most perplexing and yet unresolved problems is the discrepancy observed between batch derived and column derived adsorption capacities. Several studies indicate the existence of the above phenomena, especially when U(VI) has been

used as an adsorbate. One of the goals of this study was to understand the causatives of the above problem using both natural heterogeneous geomedia and a homogeneous synthetic adsorbent (Chapter 4). The uncontaminated natural geomedia was obtained from the Oak Ridge Reservation (OR) and the synthetic media, iron oxide-coated sand (IOCS), was meticulously prepared in the laboratory.

The OR soil and IOCS were used to perform adsorption experiments with U(VI) as a solute in both batch and column modes. In the case of batch scale, adsorption experiments were conducted by varying the solid-to-solution ratio (SSR) over an order of magnitude at a fixed pH. The results indicated that the adsorption isotherms were scalable in iron oxide-coated sand system but not in OR soil system. Based on our theoretical analysis, and also supported by recent literature, the observed phenomenon occurring in natural soils could be due to a competing solute (e.g. Phosphate) that could affect the speciation of surface complexes by forming ternary species with U(VI). Hence, our study underscores the serious implications of transferring adsorption data obtained from experiments performed at different scales. Although the interactions of U(VI) and Fe-coated sands were used as representative adsorbate and adsorbent, the general principles may be applicable to other adsorbate-adsorbent systems as well.

The ever increasing growth of biorefineries is expected to produce huge amounts of lignocellulosic biochar as a byproduct. The hydrothermal carbonization (HTC) process to produce biochar from lignocellulosic biomass is getting more attention due to its inherent advantage of using wet biomass. In the present study, biochar was produced from switchgrass at 300°C in subcritical water (Chapter 5). The physiochemical properties indicated that biochar could serve as an excellent adsorbent to remove uranium

from groundwater. A batch adsorption experiment at the natural pH (~ 3.8) of biochar indicated an H-type isotherm with a maximum sorption capacity of 2 mg/g. The adsorption process was highly dependent on the pH of the system. An increase towards circumneutral pH resulted in the maximum U(VI) adsorption of ca. 4 mg g^{-1}. The results indicated a strong relationship between the speciation of U(VI) and its adsorption onto biochar. Our study demonstrates that biochar could be used as an effective adsorbent medium for U(VI). Overall, the biochar produced via HTC is environmentally benign, carbon neutral, and efficient in removing U(VI) from groundwater.

Abstract (Tamil)

பொழிப்பு: மணல்/படிவங்களின் மீதான அயப்பூச்சானது நிலத்தின் உட்பரப்பில் அடரியம்(VI)ன் புறத்துறிஞ்சல் மற்றும் கடத்தல் ஆகியவற்றை தீர்மானிக்கும் முக்கிய காரணியாக விளங்குகிறது. இந்த ஆய்வில் மண்ணின் மீது அயத்தை படலமாக பூச இரண்டு வெவ்வேறு செயன்முறைகள் கையாளப்பெற்றன. அவையாவன முறையே (அ) மண் மீது அயத்தை நேரடியாக வீழ்படியச்செய்தல் மற்றும் (ஆ) தூய கோயிதைட் தயாரித்தபின் அயத்தினை அதன் மீது புறத்துறியச்செய்தல் ஆகும் (உட்பிரிவு-2). இவ்விரு முறைமைகள் வழியாகவும் மேற்படலம் அமையப்பெற்ற மண்களின் பண்பியல்புகள் மின்னியல் நுண்பெருக்கி, சக்திவளத்தை சிதறவைத்து செய்யும் நிறமாலையியல், ஊடுகதிர் அலைவளைவு, மற்றும் தேர்வுமுறையில் அயத்தினை பிரித்தல் ஆகிய முறைகளில் அறியப்பட்டன. இவ்விரு முறைகளுமே முற்றிலும் பளிங்குறுவுள்ள அயப்பூச்சினை உருவாக்கவில்லை. ஆயினும், வீழ்படிவு முறையைக் காட்டிலும் புறத்துறிஞ்சல் முறை பெருமளவு உருவற்ற அயத்துடனான மண்ணை உற்பத்தி செய்தது. மேலும் அயத்தின் உள்ளீட்டு அளவை அதிகரிக்கும் போது உருவற்ற அயப்படிவத்தின் விகிதம் குறைவதை காணமுடிகிறது.

மூன்று வெவ்வேறு உள்ளீட்டு அளவுகளில் (0.04 - 0.3 விழுக்காடு) அயப்பூச்சு மேற்கொள்ளப்பட்ட மணலானது (IOCS), அடரியம்(VI)ன் புறத்துறிஞ்சல் வெப்ப படிவம் மற்றும் அமிலத்தன்மை வரப்புகள் ஆகிய சோதனைகளுக்குட்படுத்தப்பெற்றன (உட்பிரிவு - 3). ஆய்வின் அடிப்படையில் நோக்குகையில் அடரியம்(VI)ன் புறத்துறிஞ்சல் ஆனது அயத்தின் உள்ளீட்டளவினை விடவும் மண்ணின் மேற்பரப்பினைக் கொண்டு பொதுப்படுத்தும் போது ஒப்பிட எளிதாயிருப்பதைக் காண முடிகிறது. ஒச்சியேற்றம் பெற்ற, உருவற்ற அயத்தின் அடரியம்(VI)ன் புறத்துறிஞ்சல் தன்மையை அறிய ஏற்கனவே உருவாக்கப்பட்ட பரப்பு சிக்கற்சேர்வை மாதிரி வடிவமைப்பால், தற்போதைய ஆய்வில் காணப்படும் மணலின் பரப்பிற்கும் புறத்துறிஞ்சல் திறத்திற்கும் உள்ள ஒற்றுமையை எளிதில் விளக்க முடிகிறது.

இவ்வகை ஆய்வில் நூதனமாகவும் தீர்வு காணப்பட முடியாததாகவும் நிலைபெற்றிருப்பது யாதெனில், தொகுதி மற்றும் நிரல் முறைகளின் புறத்துறிஞ்சல் திறனில் காணப்படும் வேறுபாடேயாகும். அடரியம்(VI)-ஐ புறத்துறிஞ்சுபடுபொருளாக பயன்படுத்துகையில் இவ்வாறு வேறுபாடு உள்ளதை பல ஆய்வு முடிவுகள் கண்டுணர்ந்துள்ளன. இந்த ஆராய்ச்சியின் முக்கிய நோக்கமானது மேற்கூறிய சிக்கலினை இருவேறு மூலப்பொருட்களைக் (பன்மைக்கூறுள்ள இயற்கை மண் மற்றும் ஒருமைக்கூறுள்ள செயற்கை உறிஞ்சி) கொண்டு சிக்கலின் காரணங்களை

தெளிவுபட அறிவதே (நோக்குக உட்பிரிவு - 4). ஓக் ரிட்ஜ் ரிசர்வேஷன்(OR)-லிருந்து கொணரப்பட்ட, அடரியம்(VI)அற்ற இயற்கை மண், மற்றும் மிக நுட்பமான முறையில் ஆய்வுக்கூடத்தில் தயாரிக்கப்பட்ட அயப்பூச்சிட்டமண் ஆகியவை மேற்கூறிய ஆய்வில் பயன்படுத்தப்பட்டன.

அடரியம்(VI)ஐ கரையமாகக் கொண்டு தொகுதி மற்றும் நிரல் முறைகளில் OR மற்றும் IOCS-களின் புறத்துறிஞ்சல் திறன் ஆயப்பட்டது. அமிலத்தன்மையை நிலையாகவும் திண்ம கரைசல் விகிதாச்சாரத்தினை ஒரு தசம அளவு வரையிலான மாறிலியாகவும் கொண்டு தொகுதி முறை புறத்துறிஞ்சல் சோதனைகள் மேற்கொள்ளப்பட்டன. IOCS மணலினது புறத்துறிஞ்சல் வெப்ப படிவமானது OR மணலினைக் காட்டிலும் மடங்கிடப் படக்கூடியதாக உள்ளதை முடிவுகள் மூலம் அறிய இயலும். அடரியம்(VI)ஆனது மணலுடன் சிக்கற்சேர்வையாக இனம் பூணும் அதே வேளையில் மற்றுமொரு கரையத்துடன் (எ.கா. நாலுயிரகத்தீமுறி மின்னூட்டணு) மும்மைச்சேர்வை மூலம் இனம் பூணுதலே, இயற்கை மணலிடம் காணப்படும் புறத்துறிஞ்சல் வேறுபாடுகளுக்கு காரணமென கருத இடமுண்டு என்பதனை இந்த ஆய்வு மட்டுமின்றி ஏனைய அண்மைக்கால ஆய்வுகளும் வலியுறுத்துகின்றன. ஆகையினால், புறத்துறிஞ்சல் திறனை கணக்கிடும்போழுது ஒரு மடங்கில் செய்யப்பட்டதைக் கொண்டு மற்றொரு மடங்கிற்கான திறனை நிறுவ இயலாது என்பதனை இங்கு சுட்ட

விரும்புகிறோம். இவ்வாய்வானது அடரியம்(VI)ஐ புறத்துறிஞ்சுபடுபொருளாகவும் அயப்பூச்சிட்ட மணலினை புறத்துறிஞ்சியாகவும் முன்னிறுத்தி செய்யப்பட்டிருப்பினும் ஏனைய புறத்துறிஞ்சுபடுபொருள்-புறத்துறிஞ்சி அமைப்புகளுக்கும் இந்த செயற்பாடுகள் பொதுவானதே.

வளர்ந்து வரும் எண்ணிக்கையிலான உயிரிசுத்திகரிப்பு நிலையங்கள் பெருமளவில் மரநார் உயிரிபறப்பத்தினை (Biochar) உபபொருளாக வெளிவிடும் என்று எதிர்பார்க்கப்படுகிறது. உயிரித்திணிவிலிருந்து உயிரிபறப்பம் தயாரிக்கும் நீர்சார்ந்த வெப்பவியற் கரியமாக்கல் (HTC) முறையானது ஈரமான உயிரித்திணிவை பயன்படுத்துகிறதாதலால் மிக்க நன்மைகளைப் பயக்கும். இங்கு மேற்கொள்ளப்பட்ட ஆய்வில் 300 சதம அளவை (degree C) வெந்நீரில் ஒருவகை கோரைப்புல்லிலிருந்து (switchgrass) உயிரிபறப்பம் தயாரிக்கப்பட்டது (நோக்குக உட்பிரிவு - 5). நிலத்தடி நீரிலிருந்து அடரியத்தினை புறத்துறிய தேவையான தன்மைகள் உயிரிபறப்பத்தில் உள்ளதென அதனின் இயல்-வேதி பண்புகள் உணர்த்துகின்றன. ஏறத்தாழ 3.8 அமிலத்தன்மை கொண்ட உயிரிபறப்பத்தினை பயன்படுத்தி தொகுதி முறை புறத்துறிஞ்சல் சோதனை செய்யப்பட்டது. அதிகபடியாக 2 mg g^{-1} உறிஞ்சல் திறனுள்ள H-ரக வெப்ப படிமங்கள் கண்டறியப்பட்டன. மேலும் இவ்வாறான உறிஞ்சல் திறன் அமைப்பின் அமிலத்தன்மையினை பெருமளவில் சார்ந்திருப்பது தெரியவந்துள்ளது. நீரினை ஒத்த அமிலத்தன்மை குறியீட்டினை

நெருங்குகையில் அதிக்கப்படியான அடரியம்(VI) (ஏறத்தாழ 4 mg g^{-1}) புறத்துறியப்படுவதை காண இயலும். அடரியம்(VI)ன் இனம் பூணுதலுக்கும் உயிரிபற்பத்தின் புறத்துறிதிறனுக்கும் இடையே வலுமிக்க உறவு இருப்பதனை இவ்வாய்வு முடிவுகள் தெரிவிக்கின்றன. உயிரிபற்பமானது அடரியம்(VI)இனை திறம்பட புறத்துறியும் ஊடகம் என்பதை மேற்கூறிய சோதனைகள் தெளிவுபடுத்துகின்றன. நீர்சார்ந்த வெப்பவியற் கரியமாக்கல் முறையில் உற்பத்தி செய்யப்பட்ட உயிரிபற்பம் சூழியலுக்கு இயைந்ததாகவும், கரிய முனைப்பற்றதும், நிலத்தடி நீரிலிருந்து அடரியம்(VI)ஐ மிகுதியாக நீக்கும் திறனுள்ளதாகவும் அமையப்பெற்று விளங்குகிறது.

Acknowledgments

I would like to express my sincere gratitude to my advisor Dr. Mark O. Barnett, for his guidance and continued support throughout my dissertation work. It would have been impossible for me to complete this work without his advice. I would like to express my sincere thanks to Dr. T. Prabhakar Clement, for without his support, my goal of pursuing higher education at the United Sates would have been a much harder task.

I would like to whole-heartedly acknowledge the support of my committee members, Dr. Yucheng Feng and Dr. Ahjeong Son, for their willingness to be a part this work. Their suggestions greatly helped improve this dissertation. My sincere thanks to Dr. Anne Gordon, for readily accepting my request to be the outside reader. I would always remain thankful for her support in helping me get a graduate teaching assistantship in the Department of Chemistry during the last year of my research work. A mere acknowledgement in few sentences would definitely not suffice for the efforts and support given by my family members all through my life, especially in this undertaking. Also, I would like to express my sincere appreciation to all my friends for their constant support in this endeavor. Especially, I would like to appreciate Mr. Mahendran Balasubramanian and Mr. Karthikeyan Balasubramanian for their quality translation of the dissertation's abstract in Tamil language.

I would like to extend my acknowledgment to all the people, especially my teachers, who inspired and helped me to pursue higher studies. A subset of them includes Dr. Nagabhushana Rao, Dr. Jacob Dane, Dr. Albrecht Schmitt, and Dr. Usha Natesan. I would also like to thank Dr. Jeffrey Fergus, Dr. John Gordon for spending their valuable time in providing insightful suggestions.

My sincere thanks to Dr. Sandeep Kumar's whose support and understanding helped in carrying-out a collaborative study. Also, I would like to extend my thanks to Dr. Ram B. Gupta and his research group for their support in the above collaboration. I would like to express my gratitude to Dr. Zhao and Dr. Michael Miller for offering their laboratory equipment and facilities, respectively. I greatly appreciate Mr. Jinling Zhung for being an ever-helpful laboratory supervisor, and Ms. Sherry Smith for her help with administrative support. Also, I would like to thank Mr. Roy Howard, Mr. Thomas Carrington, Mr. William Wills, and Mr. Allen Screws for their training and support.

I greatly appreciate all the various funding sources that helped me to carry-out this research work. The funding sources include Office of Science (BER), U.S. Department of Energy Grant No. DE-FGO2-06ER64213, Sustainable Water Resources Research Center of Korea's 21st Century Frontier Research Program via Seoul National University, Department of Civil Engineering via the start up Grant support of Dr. T. Prabhakar Clement, Department of Civil Engineering's Graduate Teaching Assistantship, Dr. Barnett's research grant with Office of Science (BER), U.S. Department of Energy.

My special thanks to Dr. Vince Cammarata, Mr. Steve Swann, and Ms. Lynn Walker in Department of Chemistry and Biochemistry for supporting me with the graduate teaching assistantship for the last four semesters that allowed me to finish my research as planned. Finally, I would like to thank all the office personnel in Graduate School, and the Office of International Education that always welcomed me and made my stay and study in Auburn a memorable one to cherish, overall.

Table of Contents

List of Figures

List of Tables

1. Introduction and Objectives

1.1 Background

The element uranium, represented by the chemical symbol U, is the heaviest element found naturally on earth. With an atomic number of 92, natural uranium exists in three isotopes, that include U-234, U-235, and U-238. It is estimated that the earth's crust contains about 2.4 ppm of U (Kaltsoyannis and Scott, 1999). The major sources of uranium includes uraninite (U_3O_8), coffinite ($USiO_4$), and carnotite ($K_2(UO_2)_2(VO_4)_2.3H_2O$). Of the three natural isotopes of uranium, about 99.27% exists in the form of U-238. The less abundant (0.72%) U-235 is fissile and hence can be exploited to produce energy or to make nuclear weapons. Hence, the uranium used for the above processes needs to be enriched in U-235 to carry out continuous fission. An enrichment of U-235 to about 5% is used in nuclear reactors for producing energy, whereas ~90% enrichment in U-235 is required to make weapons. In the early 1940's, uranium was heavily used in the nuclear weapons program and energy production. Ever since, the vast use of uranium has left a legacy of contaminants in the subsurface environment especially at most of the U.S. Department of Energy sites (Gee et al., 2007). The processes of uranium extraction from ores, uranium enrichment for energy and weapons production, and the eventual disposal of spent nuclear fuel results in large amount uranium wastes. In the United States, the uranium containing wastes contained/disposed of at Department of Energy sites are of serious concern to the environment both because of their quantity and the nearby environment (e.g. adjoining water bodies). Hence an understanding of the subsurface speciation of uranium is pivotal to assess the fate of uranium in the environment. The speciation of uranium and its mobility in the subsurface is determined by some of the common subsurface interactions of U with the geomedia such as sorption-desorption, precipitation-dissolution, redox reaction etc.

1.2 Fundamental U(VI) Reactions

Although uranium can exist in four different valence states (+3, +4, +5, +6), the tetravalent and hexavalent forms of uranium are the predominant species encountered in subsurface anoxic and oxic environments, respectively (Clark et al., 1995). Both the tetravalent and hexavalent forms of uranium are commonly found as dioxo linkages, UO_2, and UO_2^{2+}, respectively. The uranyl cation species (UO_2^{2+}) has a linear structure that contains two oxygen atoms in its axial position, with each oxygen atom forming a double bond with the central uranium atom (Kaltsoyannis and Scott, 1999). The higher solubility of U(VI) when compared to U(IV) in the presence of oxygen in the subsurface makes U(VI) the most prevalent form of U in groundwater. The sorption of U(VI) in the subsurface is dominated by its interaction with soil minerals, especially metal oxides and oxyhydroxides of Fe, Al, etc., (Hsi and Langmuir, 1987, Schmeide et al., 2000, Davis et al., 2004). The sorption of U is determined by its speciation and is highly sensitive to the pH of the subsurface environment (Waite et al., 1994).

Aqueous speciation of U(VI):

The aqueous speciation of 4.2E-6 M (ca. 1 mg L^{-1}) U(VI) with respect to pH is shown in figure 1.1. The simulation was performed using the chemical speciation software Visual MINTEQ ver. 3.0 (Gustafsson, 2009). In the absence of any complexing ligands other than H_2O and OH^-, the aqueous speciation of uranium is dominated by uranyl cation and uranyl hydroxides (Figure 1.1). At lower pH's (3.00 - 5.25) the uranyl cation tends to predominate the aqueous speciation. About 5% of U(VI) is complexed by nitrate ion at pH < 4.00 (not shown in the plot). An increase in pH beyond 4, results in the appearance of uranyl hydroxides, in the form of monomeric uranyl hydroxides viz. UO_2OH^+, $UO_2(OH)_{2\,(aq)}$, $UO_2(OH)_3^-$.

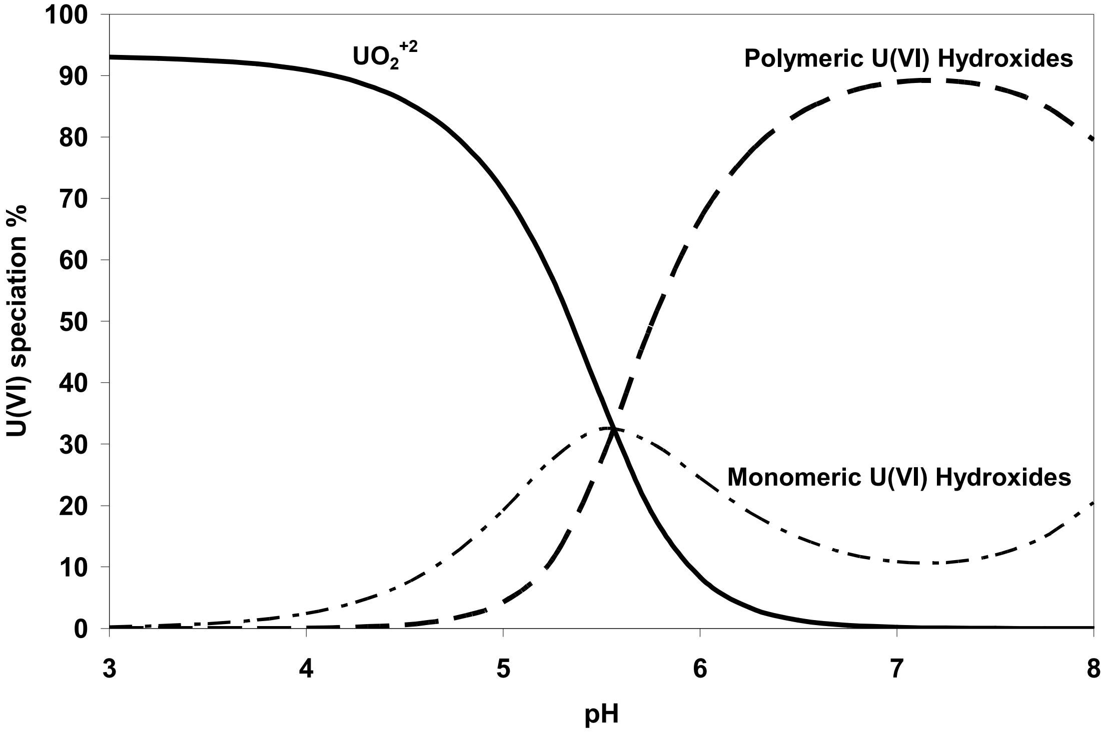

Figure 1.1 Aqueous speciation of U(VI) with respect to pH in the absence of complexing ligands. Simulation conditions -Total U(VI): 4.2E-6M, I:0.1 M $NaNO_3$.

A further increase in pH (5.00 – 7.00) favors the formation of polymeric uranyl hydroxide species viz. $(UO_2)_2(OH)_2^{2+}$, $(UO_2)_2OH^{3+}$, $(UO_2)_3(OH)^{5+}$, $(UO_2)_3(OH)_4^{2+}$, $(UO_2)_4(OH)^{7+}$, $(UO_2)_3(OH)_7^{-}$, $(UO_2)_3(OH)_4^{2+}$. The reversal in the trend of polymeric uranyl hydroxides beyond pH 7.25 was due to the appearance of uranyl hydroxide anion in the form of monomeric $UO_2(OH)_3^{-}$.

Uranium is a "Hard" Lewis acid and readily forms aqueous complexes with "Hard" Lewis bases (F^{-}, CO_3^{2-}, SO_4^{2-} etc.). The most common aqueous U(VI)-Carbonate reactions are as follows (Phillippi et al., 2007):

$$\mathbf{UO_2^{2+} + H_2CO_3^{*} \leftrightarrow UO_2CO_3^{0} + 2H^{+}} \quad (1.1)$$

$$\mathbf{UO_2^{2+} + 2H_2CO_3^{*} \leftrightarrow UO_2(CO_3)_2^{2-} + 4H^{+}} \quad (1.2)$$

$$\mathbf{UO_2^{2+} + 3H_2CO_3^{*} \leftrightarrow UO_2(CO_3)_3^{4-} + 6H^{+}} \quad (1.3)$$

$$\mathbf{2UO_2^{2+} + 3H_2O + H_2CO_3^{*} \leftrightarrow (UO_2)_2CO_3(OH)_3^{-} + 5H^{+}} \quad (1.4)$$

The aqueous U(VI) speciation of a system equilibrated with atmospheric CO_2 is shown in figure 1.2. Similar to figure 1.1, the aqueous speciation is dominated by uranyl and uranium hydroxides in the lower pH range (pH 3.00-5.00). The increase in pH beyond 5.00 resulted in the formation of U-carbanato complexes. The three major forms of the U-cabonato species identified in the simulation were $UO_2CO_{3(aq)}$, $UO_2(CO_3)_2^{2-}$, $UO_2(CO_3)_3^{4-}$.

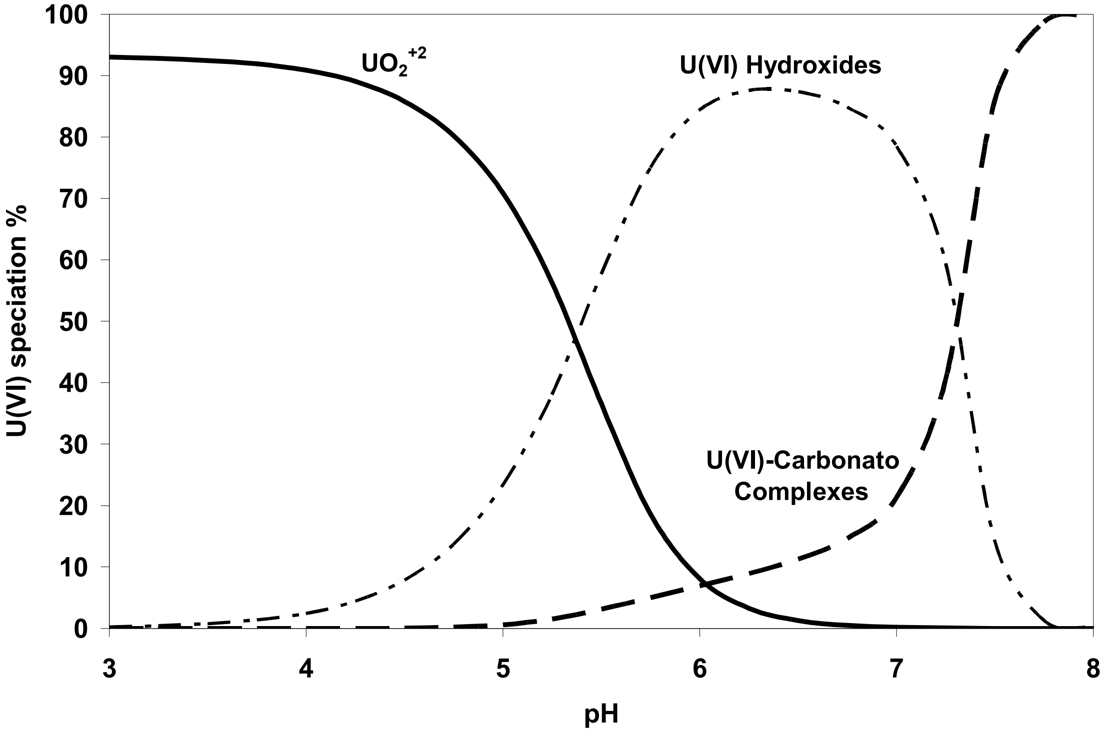

Figure 1.2 Aqueous speciation of U(VI) with respect to pH in the presence of atmospheric CO_2. Simulation conditions -Total U(VI): 4.2E-6M, I:0.1 M $NaNO_3$, P_{CO_2}: $10^{-3.5}$ atm.

Adsorption of U(VI) onto geomedia:

In the absence of any complexing ligands, the pH versus sorption relationship takes a sigmoidal shape with sorption increasing with increasing pH (Figure 1.3). The data for the above plot was derived from Barnett et al. (2002) for illustrative purposes, wherein the adsorption of U(VI) onto a natural geomedia rich in iron oxides is showed. The reason for the above adsorption trend is due to the positive charge on the uranyl ion and the charge reversal of the adsorbing surfaces with respect to pH. Assuming the point of zero charge of the geomedia is around circumneutral pH (a valid assumption for common iron oxides found in the subsurface), at low pH the geomedia possesses a positive charge resulting in the repulsion of the positively charged uranyl ion by the adsorbing surface and the contrary happens at higher pH. Moreover, the decline in sorption beyond pH 9 may be due to the existence of U in the form of negatively charged uranium hydroxide [$UO_2(OH)_3^-$)] species.

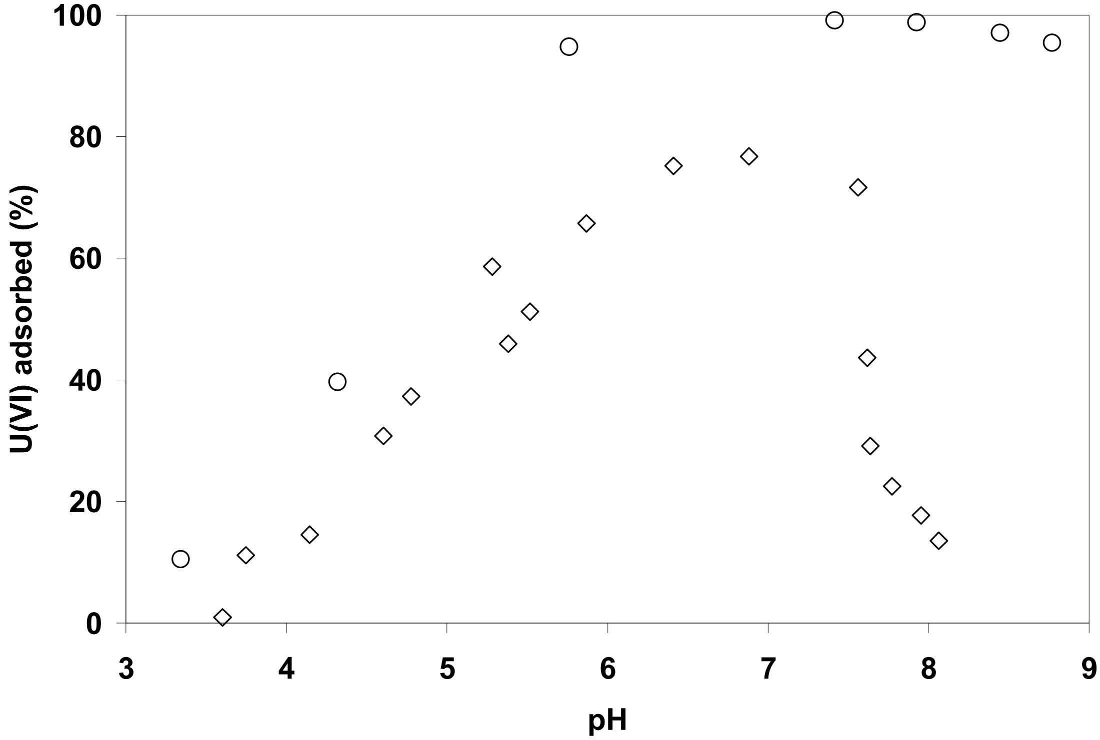

Figure 1.3 Sorption of U(VI) as a function of pH onto a natural geomedia in the presence (◊, P_{CO_2}= $10^{-3.5}$ atm.) and absence of carbonate (○). Data source: Barnett et al., 2002.

In the case of systems equilibrated with atmospheric CO_2, the sorption of U(VI) onto natural geomedia is influenced by the U-carbonato species as shown in figure 1.3. The aqueous U(VI)-carbonato complexes (reactions 1.1-1.4) influence the uranium sorption to the geomedia beyond circumneutral pH in the presence of dissolved carbonates. When compared to the system without carbonate, carbonate-containing systems indicate a decrease in the sorption of U(VI) beyond pH 7.00 which is caused due to the formation of aqueous uranium-carbanato complexes. Apart from carbonates, the presence of other halides (e.g. fluoride), humic acids from natural organic matter (Lenhart and Honeyman, 1999), and alkaline earth metals like Ca^{2+}, Mg^{2+} in the subsurface could form aqueous complexes with U(VI). These aqueous complexes were shown to be one of the major causes for the mobility of U(VI) in the subsurface and its far-field transport (Clark et al., 1995; Fox et al., 2006).

As mentioned before, the sorption of U(VI) to geomedia is dominated by the presence of metal oxides and oxyhydroxides. Moreover, these adsorption reactions are conceptualized as surface complexation reactions (reactions 1.5 and 1.6) wherein the aqueous U is complexed by the oxides present on the surface of the geomedia. For example, in the case of U adsorption to Fe-oxides in carbonate-containing systems, the following reactions are considered (Phillippi et al., 2007):

$$\mathbf{2 > Fe_sOH \quad + \quad UO_2^{2+} \quad \leftrightarrow \quad (> Fe_sO)_2 UO_2^0 \quad + \quad 2H^+} \tag{1.5}$$

$$\mathbf{2 > Fe_sOH + UO_2^{2+} + H_2CO_3^* \quad \leftrightarrow \quad (> Fe_sO)_2 UO_2CO_3^{2-} + 4H^+} \tag{1.6}$$

The above reactions show that U is adsorbed as an inner sphere bidentate surface complex with two different U-O equatorial bond distances (Figure 1.4) that has been conformed by x-ray spectroscopy (Waite et al., 1994). Hence the mobility of U in the subsurface is greatly influenced by the interplay between the sorption of uranium to the surface oxides/oxyhydroxides and the ability of U to be complexed by aqueous species.

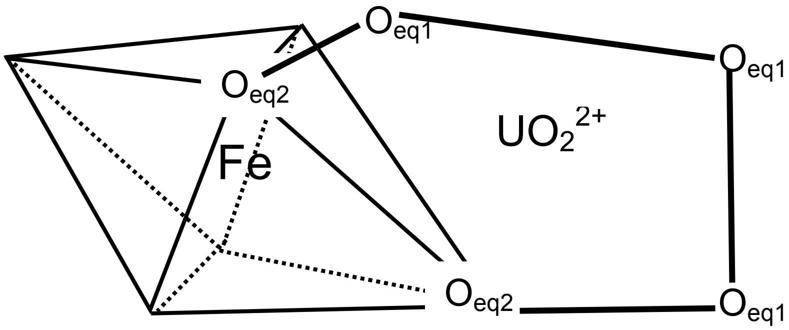

Figure 1.4 Model structure showing U(VI) adsorption onto Ferrihydrite. Oeq1 and Oeq2 are equatorial oxygen atoms of uranyl ion. Adapted from: Waite et al. (1994).

1.3 Precipitation-Dissolution and Redox Reactions

The precipitation-dissolution reactions and the redox reactions of uranium in the subsurface are strongly coupled. Both the reactions are additionally significant since the major remediation strategies to control the mobility of uranium are based on these processes. The solubility of U(IV) in the form of uraninite (UO_2) is lesser than U(VI) and hence U(IV) is the preferred pathway to immobilize U in most subsurface U remediation strategies. The above process can be triggered by both abiotic or by biotic (microbially mediated) means. In the subsurface environment, the abiotic process of U(VI) to U(IV) reduction is coupled with the Fe(II) to Fe(III) oxidation reaction as follows (Zielinski and Meier, 1988):

$$UO_2^{2+} + 2Fe^{2+} \rightleftharpoons UO_2 + 2Fe^{3+} \quad (1.7)$$

The above redox reaction was generally shown to occur on Fe^{2+} minerals or Fe^{2+} adsorbed onto other mineral surfaces and not by aqueous Fe^{2+} (Fendorf and Hansel, 2002). On the contrary, the reaction can also be mediated by common dissimilatory metal reducing bacteria and sulfate reducing bacteria in the subsurface. In the microbially mediated process, the concentration of Fe^{2+} and the form of Fe oxides/oxyhydroxides (crystalline or amorphous) dictates the stability of biogenic UO_2 precipitates (Ginder Vogel., 2008). Moreover the presence of NO_3^-, Ca^{2+} and CO_3^{2-} favors the oxidation of U(IV) to U(VI) and could potentially influence the precipitation process.

Since the dynamic chemical environment in the subsurface favors the oxidized species of U, the solubility of U(VI) is of higher importance. The solubility of U(VI) in aqueous solution is controlled by the uranyl oxide hydrates [e.g. schoepite ($UO_2(OH)_2.2H_2O$)] which is a function of pH (Giammar and Hering, 2001). Apart from the redox control on uranium precipitation, the reaction between U(VI) and phosphate results in autunite (X_{1-2} $[(UO_2)(PO_4)]_{2-1}.nH_2O$], where X is a monovalent or a divalent cation), and under aerobic conditions, is used as a reactive barrier strategy to control U(VI) mobility (Wellman et al., 2007). Although the above precipitation reactions are useful reactions for U immobilization, the precipitate of U(VI) with Fe oxides show the formation of U-Fe colloids that could enhance U mobilization (Duff et al., 2002).

1.4 Surface Complexation Modeling

Since the semi-empirical isotherm models viz. Linear, Freundlich, Langmuir etc. fail to describe the adsorption of a solute onto the sorbent under changing chemical conditions (pH, co-solutes, ionic strength etc.), the concept of surface complexation models (SCM) was formulated (Goldberg and Criscenti, 2008). The SCM approach aids in bridging the macroscopic contaminant transport processes to the molecular level physico-chemical interactions of the contaminant with the subsurface material. Some of the earlier approaches used in SCM includes constant capacitance model, diffuse double layer model, triple layer model. These models differ in their conceptualization of charge versus potential relationships of the electrical double layer. One of the major concepts introduced to the field of surface complexation modeling in 1990's was the CD-MUSIC (charge distribution- multisite complexation) approach. The multisite concept precedes the charge distribution concept both of which continue to evolve under the CD-MUSIC framework to model adsorption processes (Hiemstra et al., 1989a,b; Hiemstra et al., 1996). In the CD-MUSIC approach the molecular level structural details of the adsorbing surfaces and the interacting aqueous phase ions are incorporated. Until 1990, the charge-potential relationship was the only primary factor that used to differentiate the conceptualizations of the electrical double layer (constant capacitance, diffuse double layer, triple layer etc.). The concept of structure-charge-potential relationship was introduced in the form of CD and MUSIC approaches.

Multisite complexation:

The multisite concept was based on the bond-valence theory proposed by the late Nobel laureate Linus Pauling. Using bond-valence theory, the strength of the electrostatic bond of surface groups (O, OH etc.) is calculated as follows: $s = z / CN$, wherein s = bond-valence, z = charge of the metal, CN = coordination number (Pauling, 1929). For example, in the case of goethite, the bond valence is $+3/6 = +0.5$, wherein '+3' is the charge of Fe in goethite, with Fe being octahedrally coordinated to six oxygen atoms. Each oxygen atom in the bulk goethite is coordinated to three Fe atoms. Hence, in the case of goethite, the surface oxygen that forms the sorption interface, could have three different types of Fe sites (≡Fe, $≡Fe_2$, $≡Fe_3$). But the appropriate sites were found to be the following four surface site types: $≡FeOH^{-0.5}$, $≡FeOH_2^{+0.5}$, $≡Fe_3OH^{+0.5}$, $≡Fe_3O^{-0.5}$, based on the protonation characteristics of goethite in the environmentally relevant pH range of 3-10 (Venema et al., 1996). The same procedure can be used for other metal oxide surfaces as well. Thus, the rationale for the inclusion of multiple site types in CDMUSIC instead of the typical three sites used by other modeling approaches ($≡FeO^-$, ≡FeOH, $≡FeOH_2^+$) was justified. In the case of goethite, a single protonation constant was used for both (Fe and Fe_3) site types based on the one pKa approach. One of the major advantages of the 1-pKa approach is that it allows obtaining the protonation constant independently using the point of zero charge measurement instead of following a fitting exercise.

The multisite concept was implemented using the three plane model (TPM) that contains the 0, β, and d planes (Figure 1.5). The TPM consist of mineral surface, the Stern layer and the diffuse layer. The surface contains protonated or deprotonated, O or OH species that carries the residual charge. The Stern layer includes the inner (β) and outer (d) Helmholz planes with capacitances of C1, and C2, respectively. The value of the inner Helmholz plane (C1) is derived based on the inner-sphere surface complex formation of the solute with the surface sites. In the case of the outer Helmholz plane, a typical value of 0.2 F m^{-2} was used. But recently, this value has been modified to 1 F m^{-2} since the previous value of 0.2 F m^{-2} indicated an overestimation of the distance of H_2O molecule from the surface (van Riemsdijk and Hiemstra, 2006). The Stern layer was followed by the diffuse layer that contains the charge neutralizing outer-sphere electrolyte ion complexes ions that eventually terminates at the bulk solution interface. In the case of adsorption of Cu^{2+} to the surface site ($FeOH^{-0.5}$) the adsorption process results in $FeOHCu^{+1.5}$ surface species as an inner-sphere surface complex formed in the inner Helmholz plane. The electrolyte ions (e.g. nitrate) were coordinated as outer-sphere complexes in the diffuse layer.

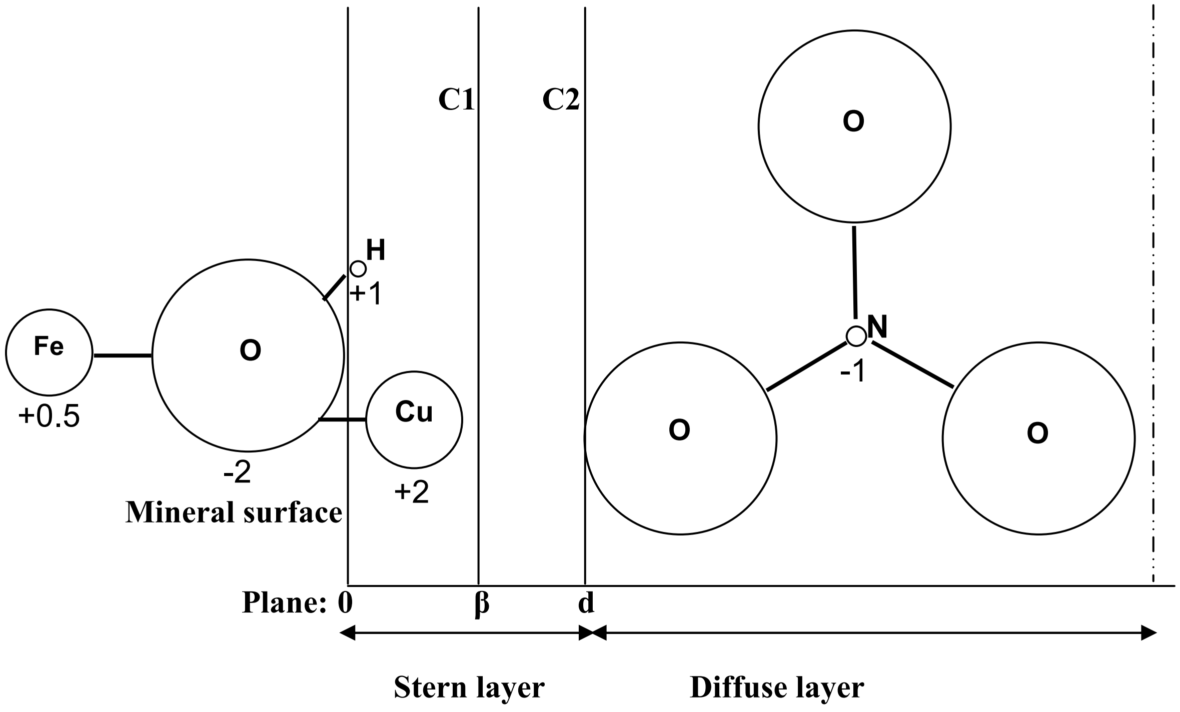

Figure 1.5 Conceptual framework of the electrical double layer as used in the CD-MUSIC model.

Charge Distribution (CD):

In the conventional modeling approach, the charge of the inner-sphere surface complexes are treated as point charges and the whole charge is assigned to either the mineral surface plane (0) or the adjacent plane (β). In the CD approach, the charge is distributed over the distance between the 0-β planes, which is a more realistic representation, especially for larger ions like PO_4^{3-}, CO_3^{2-} etc. that could form bi-dentate inner-sphere surface complexes with metal oxides/(oxy)hydroxides (Rahnemaie et al., 2006). Moreover, the aqueous complexes of certain electrolyte ions can also influence the surface charge at very high ionic strength (>0.5 M). To accommodate these effects, the concept of charge distribution has been used and the value is calculated based on charge neutralization as explained in Rahnemaie et al. (2006).

Application of the CD-MUSIC Model:

The adsorption of most of the metal ions (Th, U, Pu, Np etc.,) on to the surface of metal oxides/(oxy)hydroxides (Goethite, Hematite, Gibbsite, Rutile) is highly influenced by pH. The pH versus adsorption curves of these metals typically indicate a sigmoidal profile with adsorption increasing with pH. The CD-MUSIC model can explain this surface charging behavior by correlating it to the protons bound/desorbed by the surface sites. A review of the literature indicates that the CD-MUSIC model can simulate the adsorption of a suite of environmentally relevant anions (PO_4^{3-}, CO_3^{2-}, SO_4^{2-}), and trace metals (Cd, Co, Cu, Ni, Pd, Zn, U etc.) onto metal oxides/(oxy)hydroxide surfaces, in both single solute, and competitive multi-solute systems [e.g. As/HCO_3^- interaction with goethite] (Geelhoed et al., 1997; Ponthieu et al., 2006; Stachowicz et al., 2007; Gustafsson et al., 2009). Above all, the information obtained from the model has contributed to a better characterization of surface species. For example, the carbonate species adsorption was previously believed to be monodentate, whereas the CD-MUSIC approach predicted it to be a bidentate inner-sphere complex (Hiemstra et al., 2004). Later spectroscopic (EXAFS) data of the above system supports the CD-MUSIC prediction of the carbonate surface species (Bargar et al., 2005).

1.5 Scaling

Scaling is defined as the process of using observations made at one set of spatial and temporal scales to understand processes or postulate behaviors at another set of scales (Science and Technology for Environmental Cleanup at Hanford, 2001). The magnitude of various scales operative at a typical U(VI) contaminated site is shown in figure 1.4. The experimental scales include the biogeochemical studies (microbial, colloidal), bench scale experiments (batch, transport scenarios in 1D column, and 2D box, and 3D tank experiments) in the laboratory and the field scale vadose zone experiments. Whereas in the case of a contaminated field site, various processes are operative over a continuum of spatial scales that spans over 15 orders of magnitude (e.g. Hanford site).

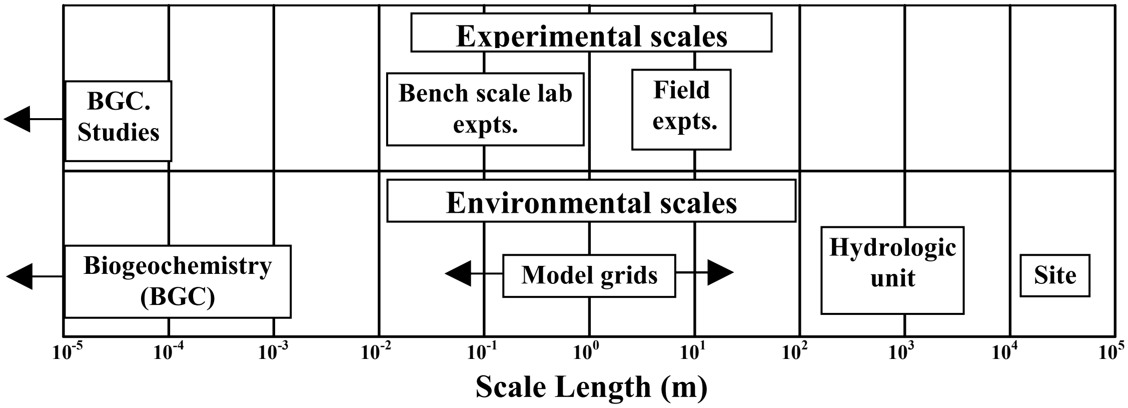

Figure 1.4 Schematic of various scales applicable at field and laboratory setting for a typical U(VI) contaminated site. ***Source: Science and Technology for Environmental Cleanup at Hanford (Whipple et al., 2001).***

The data obtained from the laboratory experiments and the sparse field experiments are often used interchangeably without considering the nature and scale of the experiments performed. Moreover, these complex scenarios are simulated using computational models that often use the assumption of physical and chemical homogeneity over three orders of magnitude.

1.6 Research Objectives

The primary objective of this research is to focus on the scaling of adsorption reactions using uranium and Fe oxide-coated sand as a model system. The rationale for the research objectives and the tasks associated with them were approached as outlined below:

- *Rationale: Natural media is highly heterogeneous and could contain pre-sorbed contaminants that might influence adsorption.*

  Task 1: Synthesize and characterize Fe oxide-coated sand and use it as a model system to perform U(VI) adsorption experiments.

- *Rationale: Understanding the adsorption of U(VI) onto coated sands is an important step towards developing scalable reaction models that can ultimately describe and predict the fate and transport of U(VI) in the subsurface.*

  Task 2: Design and perform batch adsorption experiments and identify the key scaling parameters.

  Task 3: Implement the scaling procedure in surface complexation models and predict experimental results.

- *Rationale: The scaling discrepancy observed in simple systems (centimeter/meter scale) in the laboratory should be addressed before solving large scale field transport problems (kilometer/mile scale).*

Task 4: Perform batch adsorption and 1D-transport experiments using a model system and scale the sorption parameters.

Task 5: Transfer the knowledge obtained from the model system to a heterogeneous natural geomedia.

1.7 Organization of the Dissertation

A brief introduction leading towards the objectives is given in Chapter 1. In Chapter 2, the synthesis protocols of iron oxide-coated sand and its characterization procedure is discussed in detail. Chapter 3 describes the experimental and predictive modeling approaches for U(VI) adsorption onto iron oxide-coated sand in batch systems. Chapter 4 details the experimental and predictive modeling approaches for U(VI) adsorption onto iron oxide-coated sand in 1D transport conditions. In Chapter 5, the use of hydrothermally obtained biochar for U(VI) remediation is discussed. This was a collaborative work performed along with Mr. Sandeep Kumar, Department of Chemical Engineering. Lastly, the summary of all the chapters, the implication and recommendations of this study are given in Chapter 6.

Chapters 2 and 3 are extended versions of the paper published previously by the author in *Applied Geochemistry* (Loganathan et al., 2009), which is reprinted in part here. Chapter 4 is a draft manuscript to be submitted for publication. Chapter 5 has been submitted for publication.

1.8 References

Bargar JR, Kubicki JD, Reitmeyer R, Davis JA. ATR-FTIR spectroscopic characterization of coexisting carbonate surface complexes on hematite. Geochim Cosmochim Acta 2005; 69: 1527-1542.

Barnett, M.O., Jardine, P.M. and Brooks, S.C., 2002. U(VI) adsorption to heterogeneous subsurface media: Application of a surface complexation model. Environ. Sci. Technol. 36, 937-942.

Bickmore BR, Rosso KM, Mitchell SC, 2006. Is there hope for multisite complexation modeling? In: Johannes Lutzenkirchen (Ed.), Surface complexation modeling. Elsevier, The Netherlands. pp. 269-283.

Clark, D.L., Hobart, D.E., Neu, M.P., 1995. Actinide carbonate complexes and their importance in actinide environmental chemistry. Chem. Rev. 95, 25-48.

Davis, J.A., Meece, D.E., Kohler, M., Curtis, G.P., 2004. Approaches to surface complexation modeling of uranium (VI) adsorption on aquifer sediments. Geochim. Cosmochim. Acta 68, 3621-3641.

Duff MC, Coughlin JU, Hunter DB., 2002. Uranium co-precipitation with iron oxide minerals. Geochim Cosmochim Acta 66: 3533-3547. Fendorf, S., Hansel, C.M., 2002. Operative pathways of chromate and uranyl reduction within soils and sediments. In: Zhang, P.C. and Brady, P.V. (Ed.), Geochemistry of soil radionuclides. pp111-130.

Fox PM, Davis JA, Zachara JM., 2006. The effect of calcium on aqueous uranium(VI) speciation and adsorption to ferrihydrite and quartz. Geochim Cosmochim Acta 70: 1379-1387.

Gee, G.W., Oostrom, M., Freshley, M.D., Rockhold, M.L., Zachara, J.M., 2007. Hanford site vadose zone studies: An overview. Vadose Zone J. 6, 899-905.

Geelhoed JS, Hiemstra T, VanRiemsdijk WH. Phosphate and sulfate adsorption on goethite: Single anion and competitive adsorption. Geochim Cosmochim Acta 1997; 61: 2389-2396.

Giammar, D.E., Hering, J.G., 2001. Time scales for sorption-desorption and surface precipitation of uranyl on goethite. Environ. Sci. Technol. 35, 3332-3337.

Ginder-Vogel, M., Fendorf, S., 2008. Biogeochemical uranium redox transformations: Potential oxidants of uraninite. In: Barnett, M.O. and Kent, D.B. (Ed.), Adsorption of metals by geomedia II: Variables, mechanism, and model applications. 293-320.

Goldberg, S., and Criscenti, L.J., 2008. Modeling adsorption of metals and metalloids by soil components. In: Violntem A., Hunag, P.M., and Gadd, G.M. (Ed.), Biophysico-chemical processes of heavy metals and metalloids in soil environments. 215-264.

Gustafsson JP, Dassman E, Backstrom M. Towards a consistent geochemical model for prediction of uranium(VI) removal from groundwater by ferrihydrite. Appl Geochem 2009; 24: 454-462.

J.P. Gustafsson, Visual MINTEQ, v.3.0, http://www.lwr.kth.se/English/OurSoftware/vminteq. Retrieved: 6/2010.

Hiemstra T, Dewit JCM, van Riemsdijk WH. Multisite Proton Adsorption Modeling at the Solid-Solution Interface of (Hydr)Oxides - a New Approach .2. Application to Various Important (Hydr)Oxides. J Colloid Interface Sci 1989a; 133: 105-117.

Hiemstra T, van Riemsdijk WH, Bolt GH. Multisite Proton Adsorption Modeling at the Solid-Solution Interface of (Hydr)Oxides - a New Approach .1. Model Description and Evaluation of Intrinsic Reaction Constants. J Colloid Interface Sci 1989b; 133: 91-104.

Hiemstra T, van Riemsdijk WH. A surface structural approach to ion adsorption: The charge distribution (CD) model. J Colloid Interface Sci 1996; 179: 488-508.

Hiemstra T, Rahnemaie R, van Riemsdijk WH. Surface complexation of carbonate on goethite: IR spectroscopy, structure and charge distribution. J Colloid Interface Sci 2004; 278: 282-290.

Hsi, C.K.D., Langmuir, D., 1985. Adsorption of uranyl onto ferric oxyhydroxides - application of the surface complexation site-binding model. Geochim. Cosmochim. Acta 49, 1931-1941.

Kaltsoyannis, N, Scott, P, 1999. The f elements. Oxford science publication.

Pauling L. The principles determining the structure of complex ionic crystals. J. Am. Chem. Soc. 1929; 51: 1010-1026.

Phillippi, J.M., Loganathan, V.A., McIndoe, M.J., Barnett, M.O., T.P. Clement, E.E. Roden. 2007. Theoretical solid/solution ratio effects on adsorption and transport: Uranium(VI) and carbonate. Soil Sci. Soc. Am. J. 71, 329-335.

Ponthieu M, Juillot F, Hiemstra T, van Riemsdijk WH, Benedetti MF. Metal ion binding to iron oxides. Geochim Cosmochim Acta 2006; 70: 2679-2698.

Rahnemaie R, Hiemstra T, van Riemsdijk WH. A new surface structural approach to ion adsorption: Tracing the location of electrolyte ions. J Colloid Interface Sci 2006; 293: 312-321.

Schmeide K, Pompe S, Bubner M, Heise KH, Bernhard G, Nitsche H., 2000.Uranium(VI) sorption onto phyllite and selected minerals in the presence of humic acid. Radiochim. Acta. 723-728.

Science and Technology for Environmental Cleanup at Hanford. 2001. Committee on the Review of the Hanford Site's Environmental Remediation Science and Technology Plan, Board on Radioactive Waste Management, National Research Council.185-193.

Stachowicz M, Hiemstra T, Van Riemsdijk WH. Arsenic-bicarbonate interaction on goethite particles. Environ Sci Technol 2007; 41: 5620-5625.

van Riemsdijk WH and Hiemstra T, 2006. The CD-MUSIC model as a framework for interpreting ion adsorption on metal (hydr)oxide surfaces. In: Johannes Lutzenkirchen (Ed.), Surface complexation modeling. Elsevier, The Netherlands. pp. 251-268.

Venema P, Hiemstra T, van Riemsdijk WH. Comparison of different site binding models for cation sorption: Description of pH dependency, salt dependency, and cation-proton exchange. J Colloid Interface Sci 1996; 181: 45-59.

Waite, T.D., Davis, J.A., Payne, T.E., Waychunas, G.A., Xu, N., 1994. Uranium(VI) adsorption to ferrihydrite - application of a surface complexation model. Geochim. Cosmochim. Acta 58, 5465-5478.

Waite, T.D., Davis, J.A., Fenton, B.R. and Payne, T.E., 2000. Approaches to modelling uranium(VI) adsorption on natural mineral assemblages. Radiochim. Acta 88, 687-693.

Wellman DM, Pierce EM, Valenta MM., 2007. Efficacy of soluble sodium tripolyphosphate amendments for the in-situ immobilisation of uranium. Environ Chem. 4: 293-300.

Whipple, C.G., D.W. Berman, S.B. Clark, J.C. Fountain, L.W. Gelhar, L.C. Green, R.O. Hall, E.E. Herricks, B.D. Honeyman, S. Levy, J.K. Mitchell, L.T. Silver, L. Smith, and D.A. Stonestrom, Science and Technology for Environmental Cleanup at Hanford, National Academy Press, 2001. Review of the Hanford Site's Environmental Remediation Science and Technology Plan, Board on Radioactive Waste Management, National Research Council.185-193.

Zielinski, R.A., and Meier, A.L., 1988. The association of uranium with organic matter in Holocene peat: an experimental leaching study. Appl. Geochem.3, 631-643.

2. Synthesis and Characterization of Iron Oxide-Coated Sand

2.1 Introduction

Iron (III) (oxyhydr)oxide coatings on soils and sediments are one of the most important factors in controlling the adsorption and transport of U(VI) in the subsurface (Um et al., 2007; Davis et al., 2004; Barnett et al., 2002). Various forms of Fe(III) oxides occur in nature and can be broadly classified into crystalline (e.g. goethite, hematite) and amorphous forms (e.g. hydrous ferric oxide, ferrihydrite). Amorphous and crystalline Fe oxides differ significantly in their structure and properties. Crystalline Fe oxides exhibit lower specific surface area and microporosity compared to the non-crystalline, amorphous Fe oxides (Schwertmann and Cornell, 2000). Though much work has been reported on the interaction of U(VI) with pure Fe oxides (Bruno et al., 1995; Giammar and Hering, 2001; Hsi and Langmuir, 1985; Waite et al., 1994), fewer reports are available in which Fe oxide-coated media was used as the adsorbent. At U(VI)-contaminated sites, Fe oxides often appear as coatings on other geomedia rather than discrete minerals (Davis et al., 2004; Payne et al., 1994; Um et al., 2007). However, Fe-oxide coatings exhibit different adsorption properties than pure Fe oxides (Xu and Axe, 2005).

The purpose of this chapter, which has been published in part in Loganathan et al. (2009), is to assess the various synthesis protocols to produce iron oxide-coated sands that could be used as a surrogate to natural geomedia found in U(VI) contaminated sites.

Two different methods have typically been used for the synthesis of Fe-coated sand, the precipitation method and the adsorption method (Xu and Axe, 2005; Schwertmann and Cornell, 2000; Scheidegger et al., 1993). In the precipitation method, sometimes called the homogenous method, sand is initially mixed with soluble Fe(II). Reaction conditions favorable for goethite (α-FeOOH) precipitation are then maintained, and goethite particles are in principle coated onto the sand as the Fe precipitates. The adsorption method is a two-step process, in which pure goethite is synthesized in the first step and the coating occurs in the second step, where the goethite prepared in the first step is adsorbed onto the surface of the sand. This method of coating sand is also referred to as the heterogeneous suspension method (Scheidegger et al., 1993). The coated sands obtained from both of these methods have been used as surrogates for subsurface materials to study trace metal or anion adsorption (Gabriel et al., 1998; Meeussen et al., 1996; Roden et al., 2000; Xu and Axe, 2005). Previous studies indicate that the reactive transport processes can be successfully modeled using known amount of sand and iron oxide in the system irrespective of the coating method (Scheidegger et al., 1994; Meeussen et al., 1999; Cheng et al., 2004).

2.2 Materials and Methods

Synthesis of iron oxide-coated sand:

All chemicals used were certified analytical grade and obtained from Fisher Scientific (Pittsburgh, PA) unless otherwise noted. Iron oxide-coated sand was synthesized using two common protocols, the precipitation method and the adsorption method. Pure medium-sized crystalline white quartz (confirmed by X-ray diffraction) obtained from Sigma-Aldrich, MO, with a particle size ranging between 0.210 and 0.297 mm, was chosen as the substrate. In addition to being a common subsurface mineral, quartz was chosen as the substrate because at the coating pH of 7, quartz carries a negative charge whereas goethite carries a positive charge (Scheidegger et al., 1993), resulting in a stronger binding between the two minerals.

The schematic of the precipitation method is given in figure 2.1. In this method, 1 kg of sand was added to 0.05 M of Fe(II) source (ferrous chloride or ferrous sulphate) in 1 M sodium bicarbonate buffered at pH 7 (Schwertmann and Cornell, 2000). Atmospheric oxygen was vigorously added to the system using a jumbo stirrer. Under these conditions, the Fe(II) was oxidized to Fe(III), which was marked by a series of color changes before finally forming a reddish-brown coating (Fig. 2.1). After 1.5 hours of mixing, the coated sand was washed using deionized water (18.2 MΩ.cm). The supernatant was analyzed for conductivity using an ion chromatograph and the washing was continued until the conductivity of the supernatant reached the DI water conductivity. The sands were then oven dried at 110°C for 24 hours. The precipitation method was repeated sequentially to produce three coated sands (PT–1, PT–2, and PT–3) with increasing Fe content (0.04 – 0.32%). A batch experiment was performed at pH 3 to check for the residual Fe(II) adsorption on the coated sand. At the end of 24 hour equilibration period, samples were analyzed using flame atomic absorption spectrophotometer and no residual Fe(II) was observed in the solution.

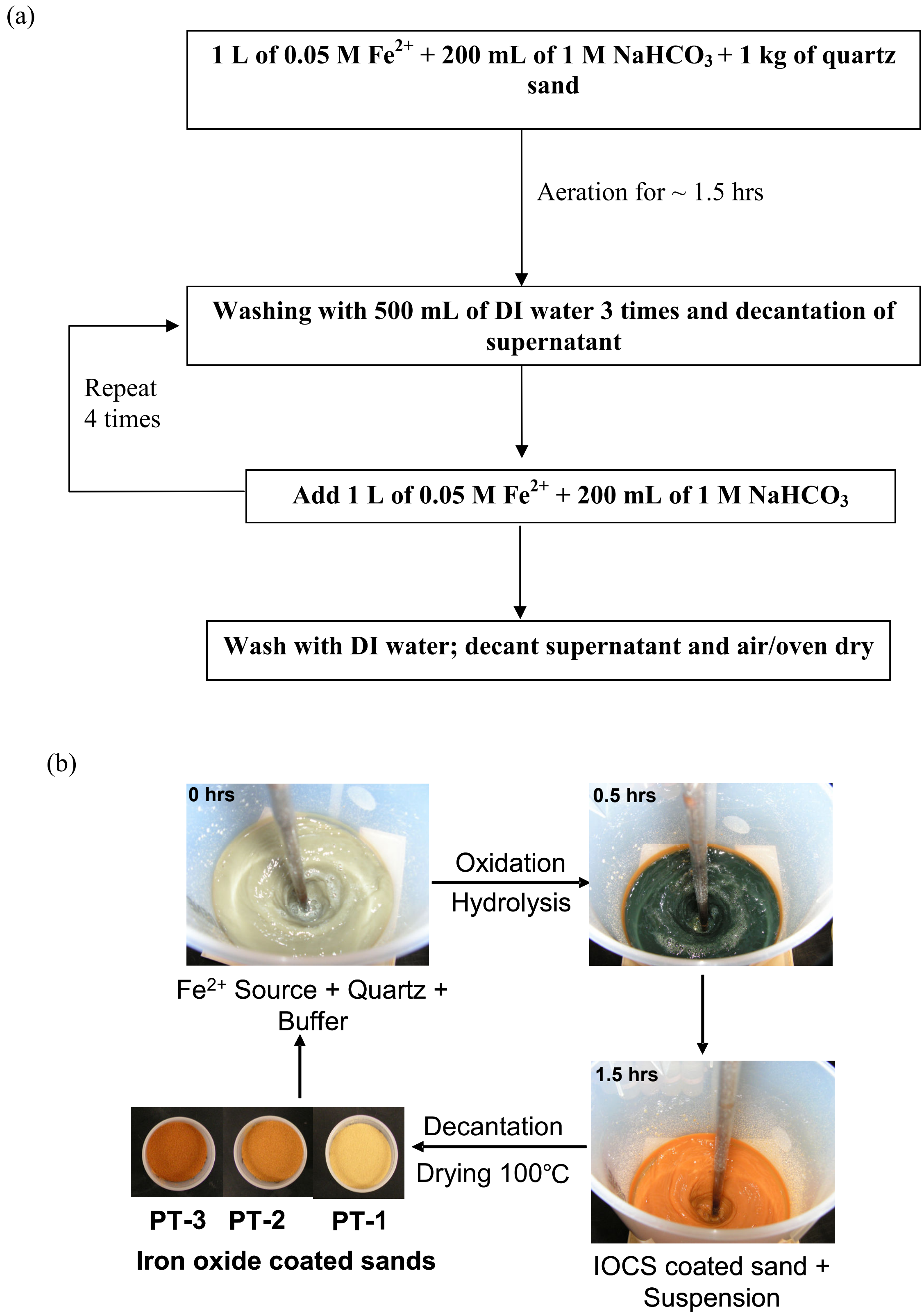

Figure 2.1 Schematic of the synthesis of iron oxide-coated sand using precipitation method.

Another common method for synthesizing coated sand is the adsorption method (Scheidegger et al., 1993), where pure goethite is synthesized first and then coated onto the sand in a subsequent step. The overall schematic of the above process is given in figure 2.2. In this process, 1 M Fe(III) nitrate served as the Fe source, which under rapid hydrolysis resulted in amorphous ferrihydrite (Schwertmann and Cornell, 2000). The ferrihydrite was converted to goethite under alkaline conditions (pH 12) maintained by 5 M potassium hydroxide at 65°C for at least 60 hours. The yellow-colored goethite precipitate was placed in dialysis tubing (MWCO 2000) and suspended in a deionized water bath for approximately one week as described by Anschutz and Penn (2005). The supernatant was then decanted and the pure goethite was freeze dried. In the second (coating) step, ~100 grams of goethite was suspended in 10 liters of 0.01 M sodium nitrate for 24 hours at room temperature and a pH of ~7 was maintained. Approximately 2.5 kg of quartz sand that had been washed with 1 M HCl and dried at 110° C was added to the suspension and mixed slowly. After 24 hours, the sand was washed with 0.01 M sodium nitrate solution that was adjusted to pH 3 (Scheidegger et al., 1993) to remove weakly bound goethite and then washed with copious deionized water until the pH stabilized at ~5.8. The initial Fe content of the sand coated in this manner was ~0.02%. The efficiency of this coating method was low (only 0.8% to 1.2% of the available Fe was coated on to the sand grains).

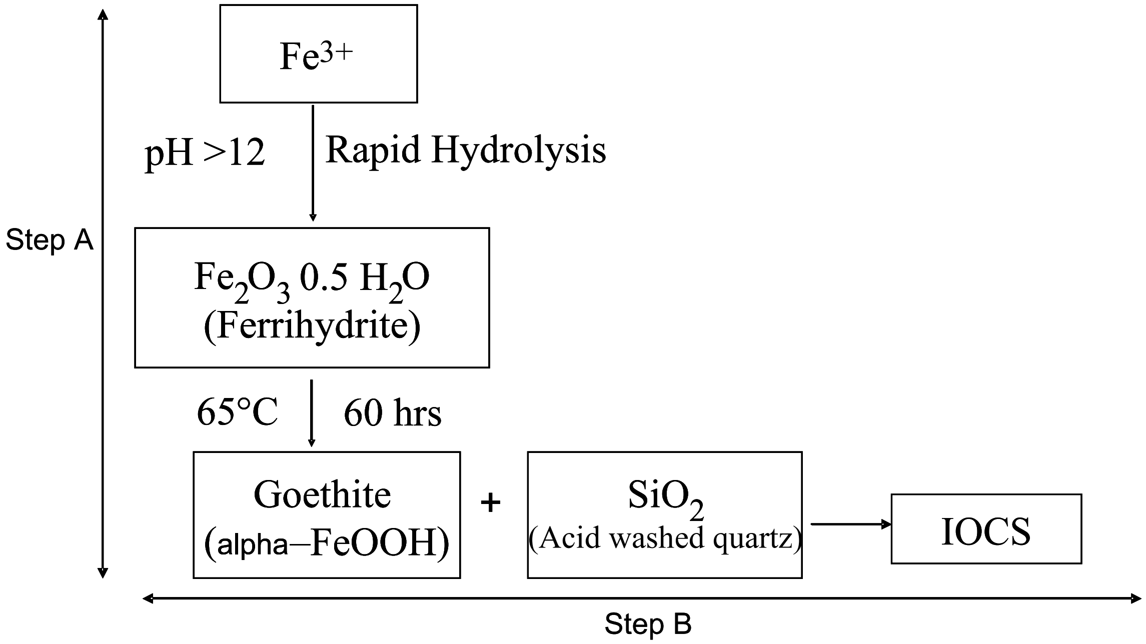

Figure 2.2 Schematic of the synthesis of iron oxide-coated sand using adsorption method.

Characterization:

Scanning electron microscopy (SEM) along with energy-dispersive spectroscopy (EDS) and powder x-ray diffraction (XRD) were used for characterizing the morphology and identifying the specific phases present. The SEM imaging was performed using a field emission high resolution JEOL 7000F scanning electron microscope under a 20 kV accelerating voltage. X-ray diffraction was performed with a Rigaku MiniFlex powder X-ray diffractometer under Cu-Kα radiation at 30 kV and 15 mA. Data were collected in a continuous scan mode at a rate of 0.5° 2θ per minute. The XRD patterns were obtained from 0° to 80° and compared with the standard goethite peaks using Jade (Materials Data, Inc.) software. Selective Fe extractions were performed to quantify the amount of amorphous and crystalline Fe (Fuller et al., 1996). The amorphous Fe was extracted using

0.2 M ammonium oxalate in the dark (AOD) for ~3 hours (Jackson et al., 1986), and a dithionate-citrate-bicarbonate (DCB) extraction was used to dissolve both crystalline and amorphous Fe oxides (Mehra and Jackson, 1960). The difference between the DCB Fe and AOD Fe nominally represents the crystalline Fe. The extracted Fe was measured using a flame atomic absorption spectrophotometer with calibration standards prepared in the extractant solution. Surface area was measured using the multipoint BET (Brunauer, Emmet, and Teller) method using $N_2(g)$ and / or Kr(g) (Micromeritics Analytical services, GA). Selected samples were analysed in duplicates and the results agreed within 10%.

2.3 Results and Discussion

SEM images of the coated sand synthesized by the precipitation method did not show the expected acicular structures of goethite on the surface (Fig. 2.3a), suggesting the presence of non-crystalline Fe minerals. Hence, a sample of the precipitate collected during the coating process was analyzed directly. The SEM image of a sample of the pure precipitate collected during the coating process showed typical acicular particles characteristic of goethite (Fig. 2.3b). Moreover, the SEM image of the coated sand after a partial DCB Fe extraction (to remove the outermost layer of iron oxide) revealed acicular goethite structures, confirming the presence of goethite in the coated sand (Fig. 2.3c). Thus we believe the sands prepared using the precipitation method consisted of a mixture of both amorphous Fe oxides and crystalline goethite. Specific surface area measurements intermediate between goethite and HFO supported this interpretation (Table 2.1). Moreover, the amorphous Fe content was dependent on the Fe(II) source. As the coating cycle increased, the sand synthesized starting with ferrous chloride as the Fe(II) source showed more amorphous Fe when compared to when ferrous sulphate was used as Fe(II) source (Fig. 2.4).

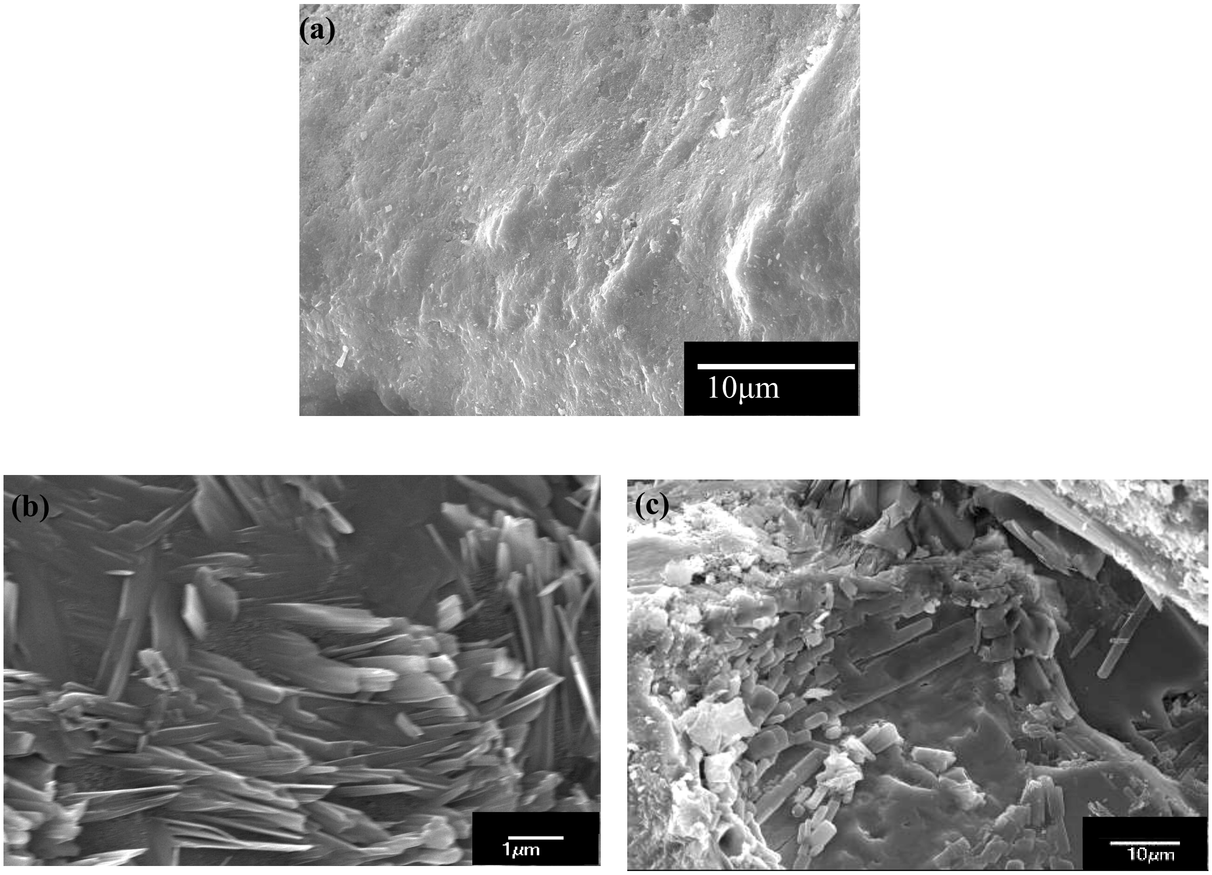

Figure 2.3 SEM images of (a) surface of a sand grain coated by the precipitation method; (b) a sample of the pure precipitate collected during the coating process, and (c) the surface of a sand grain after a partial Fe extraction.

Table 2.1 Iron content and surface area of coated sands

System	DCB Fe content (% of sand)	AOD Fe content (% of sand)	Surface Area $m^2\ g^{-1}$ of FeOOH	Surface Area $m^2\ g^{-1}$ of Fe [a]
AD–1	0.021 ± 0.001	0.0030 ± 0.0003	95.5	152
PT–1	0.040 ± 0.001	0.0063 ± 0.0001	223.1	355
PT–2	0.182 ± 0.005	0.0151 ± 0.0003	135.8	216
PT–3	0.315 ± 0.007	0.0123 ± 0.0003	105.6	168
Quartz	n/a	n/a	n/a	n/a
Goethite	61.4 ± 0.9 (62.8[b])	3.40 ± 0.08	53.3	84.8

a. Ignoring surface area of quartz

b. Theoretical value

AD represents coated sand synthesized using adsorption method

PT represents coated sand synthesized using precipitation method

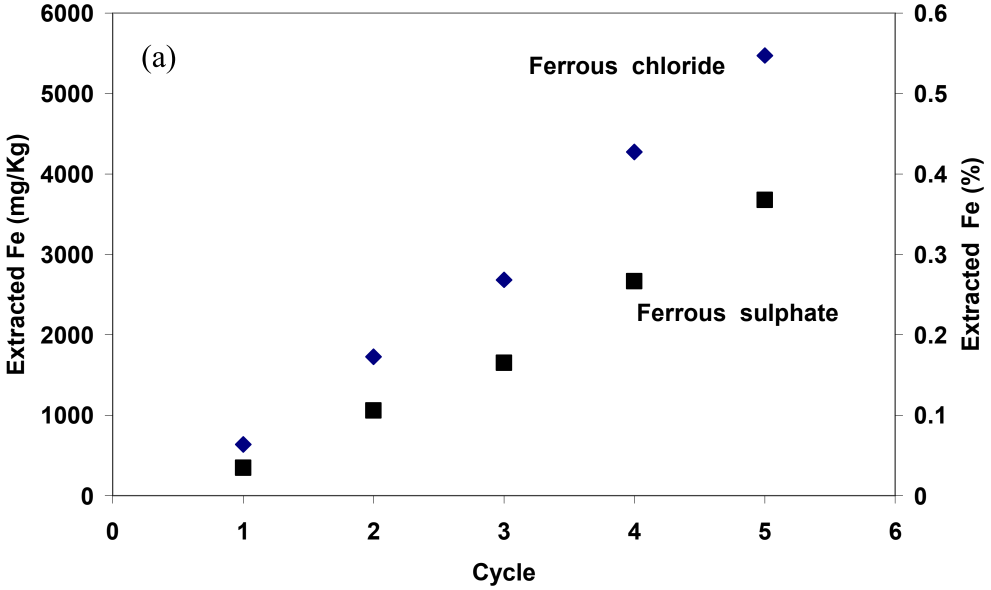

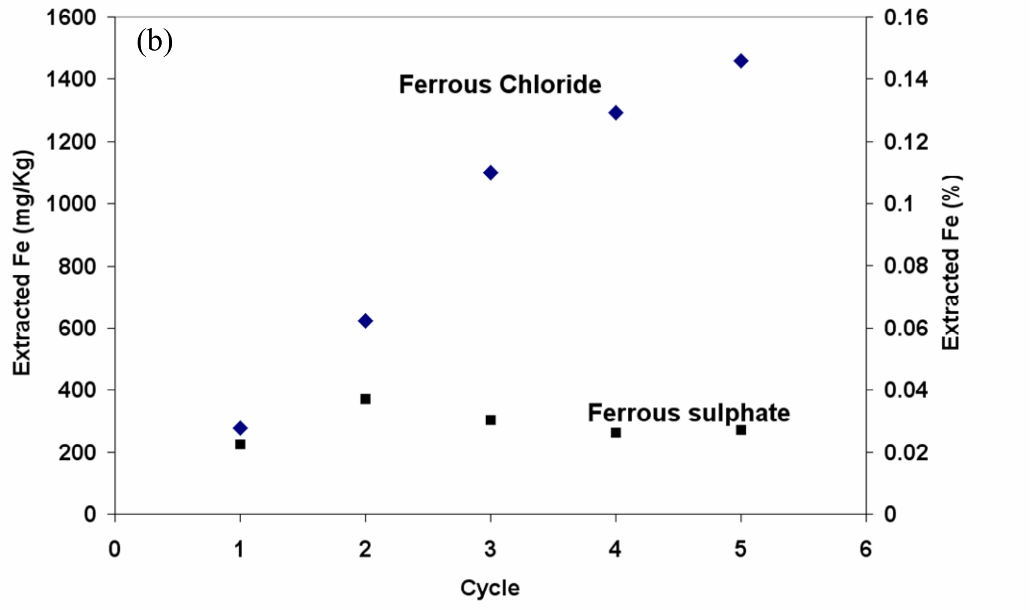

Figure 2.4 Influence of Fe^{2+} source on the (a) DCB and (b) AOD extractable Fe content of the coated sands in precipitation method.

In the case of the sand coated using the adsorption method, goethite crystals in the precipitate prepared during the first step of the process were confirmed based on their morphology (Fig. 2.5) and XRD pattern (Fig. 2.6). The SEM image of this coated sand is shown in figure 2.7. A closer view of the coated sand indicated bulk goethite deposition into the quartz pores (Fig. 2.8a). The pores here represents the surface ruptures that could have formed during the 1M acid wash performed before the coating process. The existence of about 8% of surface pores in quartz was reported by Xu and Axe (2005). However, the surface of the coated sand also showed broken goethite particles coated onto the bulk surfaces of the quartz (Fig. 2.8b). The SEM images and the corresponding EDS (Fig. 2.8a and 2.8b) of both the pores and bulk surface of the coated sand show the differences in the chemical environment between pores and regular surface, with Fe predominating in the pores and Si predominating on the free surface.

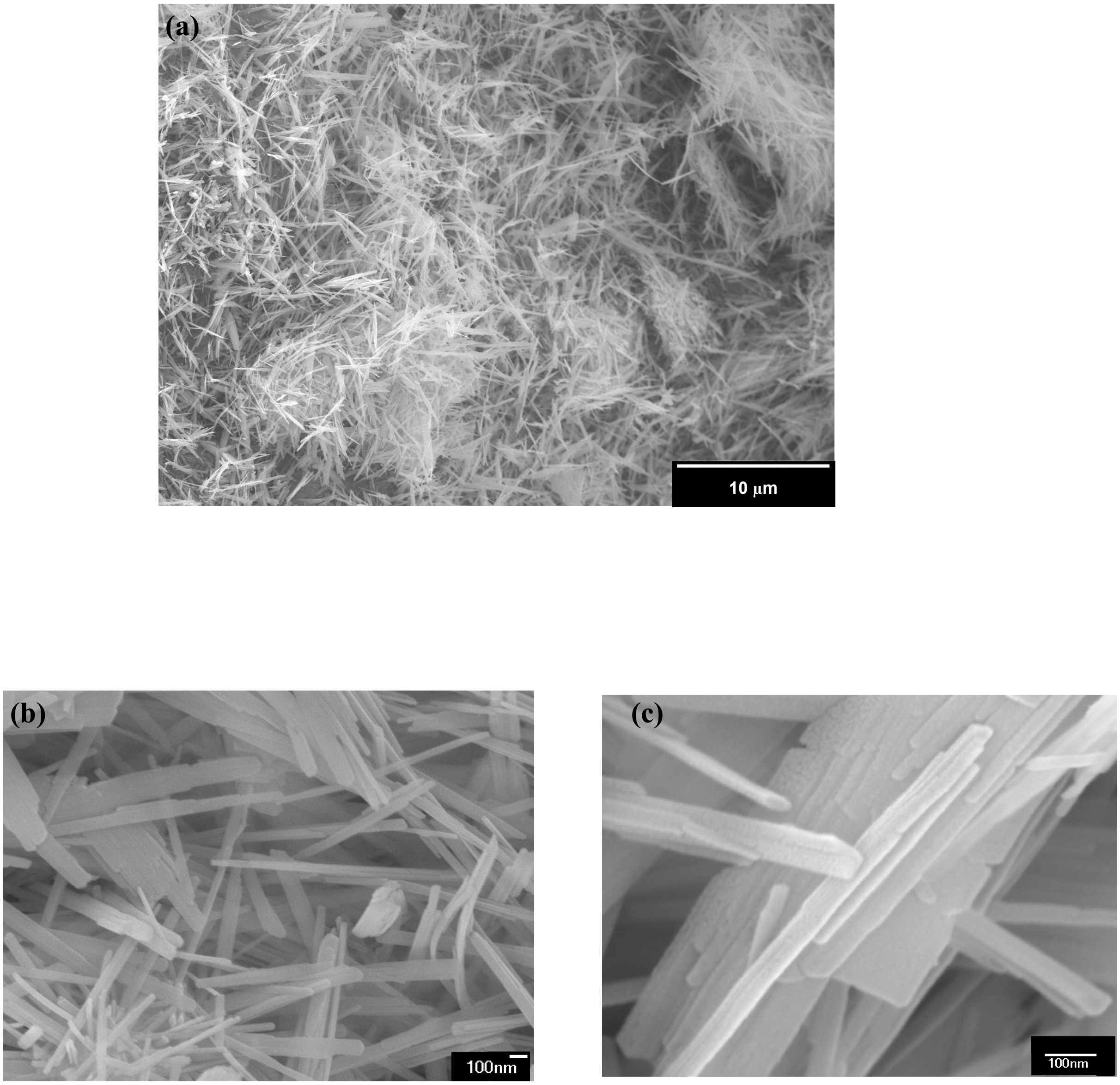

Figure 2.5 SEM images of the goethite precipitate formed during step 1 of the adsorption method at different magnifications.

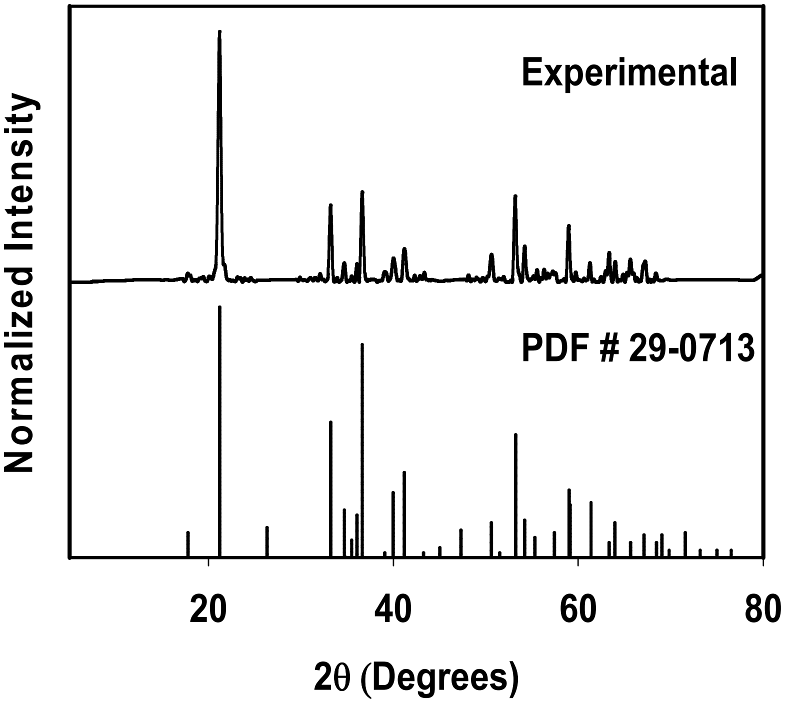

Figure 2.6 Powder XRD pattern of the goethite precipitate formed during step 1 of the adsorption method.

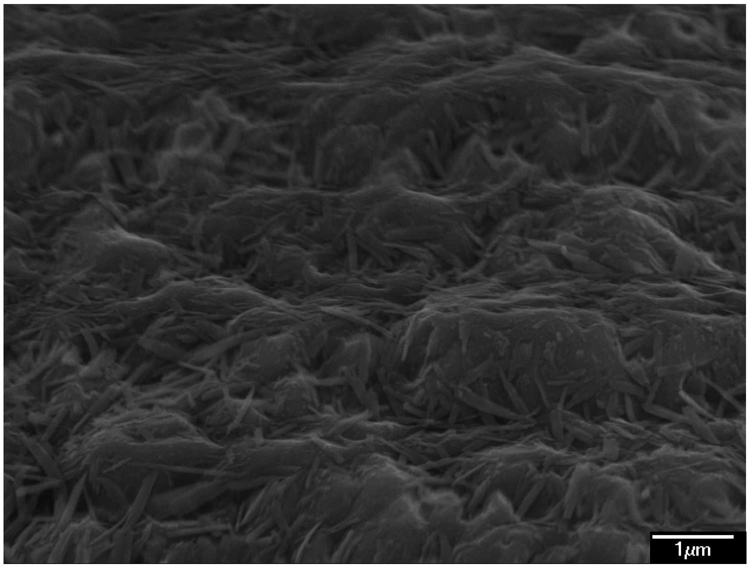

Figure 2.7 SEM image of the sand coated by the adsorption method.

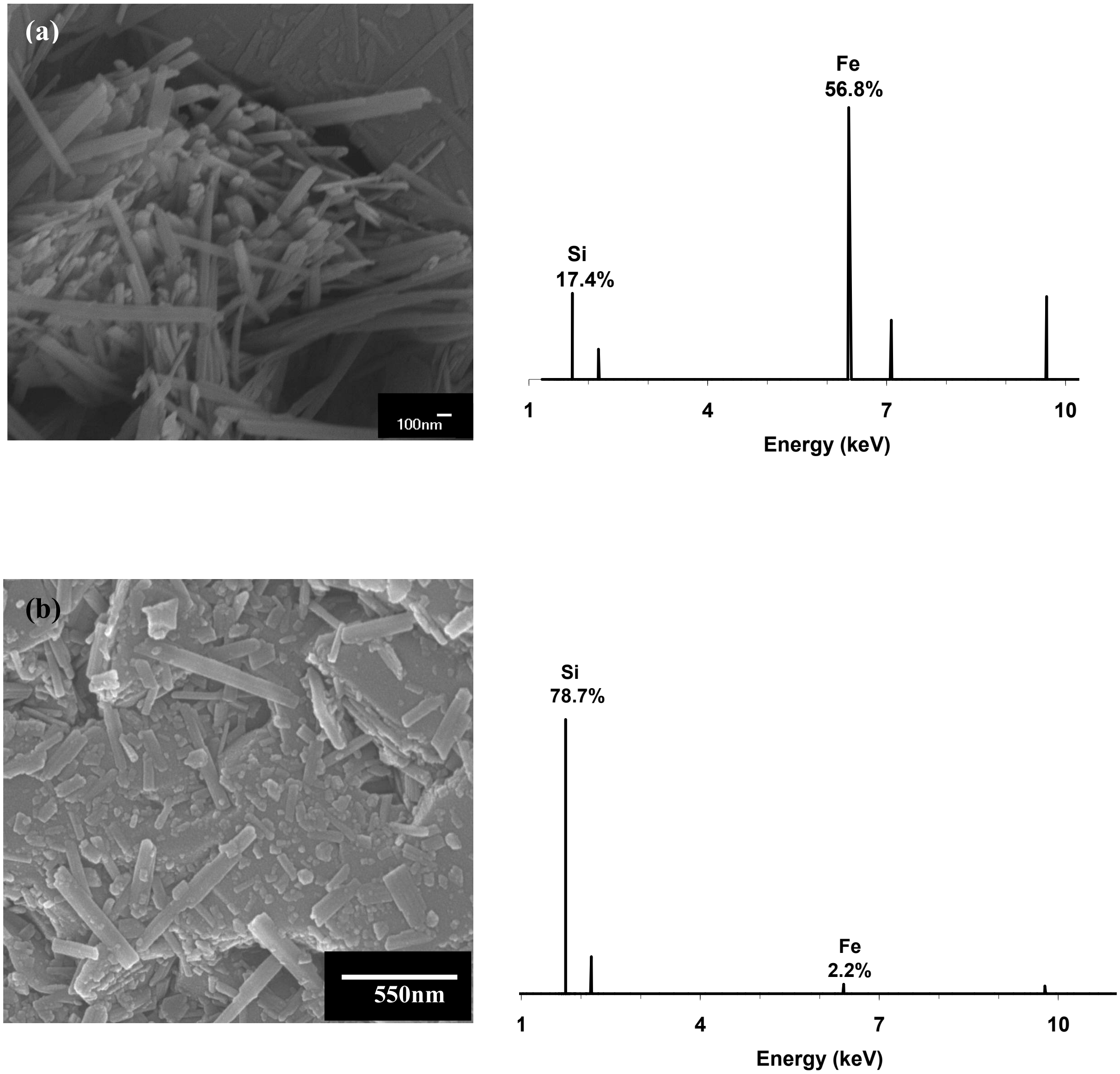

Figure 2.8 SEM images and corresponding EDS of a pore (a) and (b) regular surface of sand coated by the adsorption method.

The coating efficiency (percentage of available Fe coated onto sand) of the first step of the precipitation method was 14% compared to only 1.2% for the adsorption method. Previous studies of Filius et al. (1999) and Rennert et al. (2003) indicated that the adsorption method would result in an Fe content of ~ 0.02% on silica, similar to our results. In contrast, coated sands with Fe contents ranging between 0.06% and 2% were reported via the adsorption method by Xu and Axe (2005). However, they found that the coating temperature was an important factor controlling the level of adsorbing Fe, with the highest coating levels achieved at 60°C, well beyond the temperature we used (~ 21 ± 1°C). Furthermore, the study of Xu and Axe (2005) indicated that the sands with higher level of Fe coating had higher degree of detachment of the Fe particles under abrasion tests. In our study the coating was performed at room temperature so that the Fe coated sand is closer to the Fe coating on natural soils formed under environmentally relevant conditions.

The DCB Fe content and the BET surface area measurements of the coated sands exhibited a positive but nonlinear relationship to Fe content (Fig. 2.9). The higher specific surface areas compared to typical values for goethite, particularly for sands prepared using the precipitation method, suggests the presence of some amorphous Fe oxides in the coatings (Table 2.1), consistent with our interpretation above. The Fe content of the goethite prepared in the first step of the adsorption method had an Fe content of 61.4%, very close to its stoichiometric value. The surface area of this goethite was 53.3 m^2 g^{-1} of goethite, which falls within the range of the reported values for goethite (Kosmulski et al., 2004).

A comparative analysis between the two synthesis protocols indicates that the precipitation method had a higher coating efficiency but resulted in a less-crystalline coating with a corresponding higher specific surface area than the sand prepared using the adsorption method. The ammonium oxalate extraction indicated the presence of

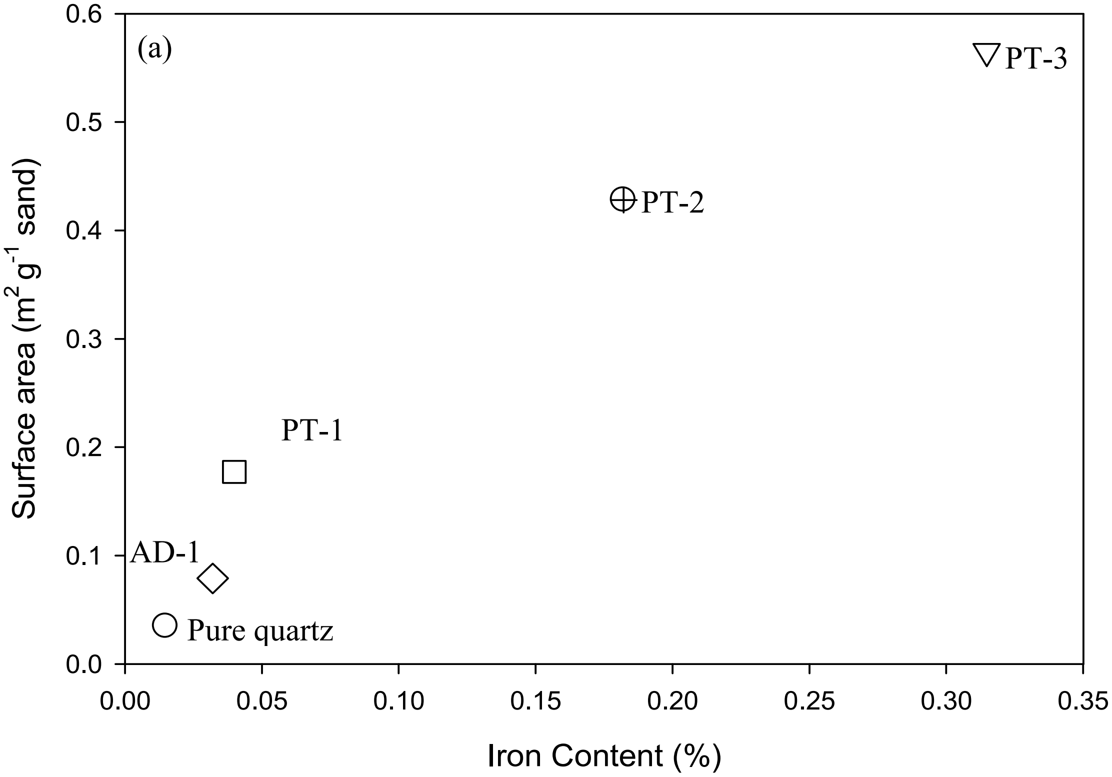

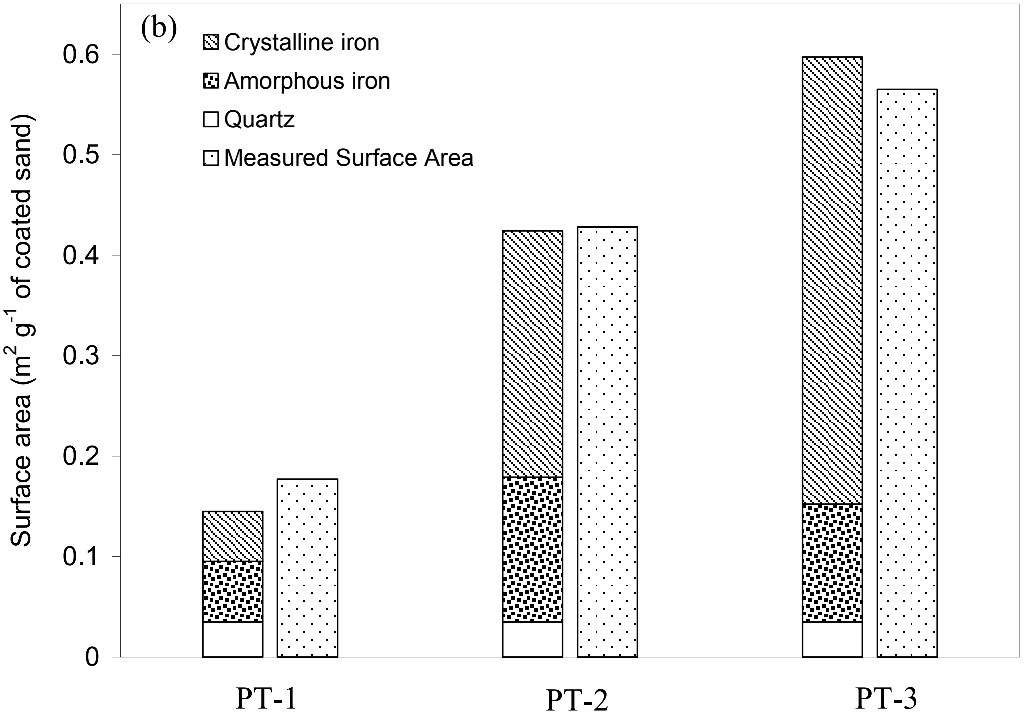

Figure 2.9 (a) Surface area versus Fe content of the synthesized sands.

(b) Calculated versus measured surface area of the coated sands.

amorphous Fe in PT sands (4% – 16%), with the crystallinity of the Fe increasing with Fe content (Table 2.1). A theoretical calculation was made assuming a specific surface area for crystalline goethite (90 $m^2 g^{-1}$) and amorphous HFO (600 $m^2 g^{-1}$) (Kosmulski et al., 2004; Weng et al., 2001; Dzombak and Morel, 1990). The theoretical estimation agreed with the measured surface area within 25% (Fig. 2.9b). The coated sand prepared using the adsorption method was expected to be essentially completely crystalline, as pure goethite prepared in the initial step (Fig. 2.5) was used in the subsequent coating step. However, the AOD measurements also indicate ~15% amorphous Fe in AD-1 (Table 2.1) as well. As a final point of comparison between the two methods, the adsorption was more time consuming (15-20 days minimum) when compared to the precipitation method (2-3 days). Both the ease of preparation of IOCS and the ability to manipulate the iron oxide coating by controlling the Fe source favored choosing sands prepared via precipitation method to perform adsorption studies with U(VI) subsequently.

2.4 Summary and Conclusion

Iron-coated sands were prepared via two common protocols, a precipitation method, where Fe was precipitated directly onto the sand in a single step, and an adsorption method, where pure goethite was prepared in the first step and then adsorbed onto the sand in a second step. Although neither of the methods produced a completely crystalline Fe coating, the precipitation method produced sands with larger portions of amorphous Fe than the adsorption method, with the fraction of amorphous Fe decreasing with increasing Fe content. Despite producing a less crystalline Fe coating, however, the precipitation method was a more efficient and less time consuming method of preparing Fe coated sand.

2.5 References

Anschutz, A.J., Penn, R.L., 2005. Reduction of crystalline iron(III) oxyhydroxides using hydroquinone: Influence of phase and particle size. Geochem. Trans. 6, 60-66.

Barnett, M.O., Jardine, P.M. and Brooks, S.C., 2002. U(VI) adsorption to heterogeneous subsurface media: Application of a surface complexation model. Environ. Sci. Technol. 36, 937-942.

Bruno, J., Depablo, J., Duro, L., Figuerola, E., 1995. Experimental-study and modeling of the U(VI)-$Fe(OH)_3$ surface precipitation coprecipitation equilibria. Geochim. Cosmochim. Acta 59, 4113-4123.

Cheng, T., Barnett, M.O., Roden, E.E., Zhuang, J.L., 2004. Effects of phosphate on uranium (VI) adsorption to goethite-coated sand. Environ. Sci. Technol. 38, 6059-6065.

Davis, J.A., Meece, D.E., Kohler, M., Curtis, G.P., 2004. Approaches to surface complexation modeling of uranium (VI) adsorption on aquifer sediments. Geochim. Cosmochim. Acta 68, 3621-3641.

Filius, J.D., Meeussen, J.C.L., Van Riemsdijk, W.H., 1999. Transport of malonate in a goethite-silica sand system. Colloids Surf., A 151, 245-253.

Gabriel, U., Gaudet, J.P., Spadini, L., Charlet. L., 1998. Reactive transport of uranyl in a goethite column: An experimental and modelling study. Chem. Geol. 151, 107-128.

Giammar, D.E., Hering, J.G., 2001. Time scales for sorption-desorption and surface precipitation of uranyl on goethite. Environ. Sci. Technol. 35, 3332-3337.

Hsi, C.K.D., Langmuir, D., 1985. Adsorption of uranyl onto ferric oxyhydroxides - application of the surface complexation site-binding model. Geochim. Cosmochim. Acta 49, 1931-1941.

Jackson M.L., Lim C.H., Zelazny L.W., 1986. Oxides, hydroxides, and aluminisilicates. In Klute A. (Ed.), Methods of soil analysis. Part I. 2nd ed. Madison, WI. ASA and SSA, pp113-119.

Kosmulski, M., Durand-Vidal, S., Maczka, E., Rosenholm, J.B., 2004. Morphology of synthetic goethite particles. J. Colloid Interface Sci. 271, 261-269.

Loganathan VA, Barnett MO, Clement TP, Kanel SR., 2009. Scaling of Adsorption Reactions: U(VI) Experiments and Modeling. Applied Geochem. 24, 2051-2060.

Meeussen, J.C.L., Kleikemper, J., Scheidegger, A., Borkovec, M., Paterson, E., Van Riemsdijk, W.H., Sparks, D.L., 1999. Multicomponent transport of sulfate in a goethite-silica sand system at variable pH and ionic strength. Environ. Sci. Technol. 33, 3443-3450.

Meeussen, J.C.L., Scheidegger, A., Hiemstra, T., Van Riemsdijk, W.H., Borkovec, M., 1996. Predicting multicomponent adsorption and transport of fluoride at variable pH in a goethite-silica sand system. Environ. Sci. Technol. 30, 481-488.

Mehra, O.P., Jackson, M.L., 1960. Iron oxide removal from soils and clays by dithionite-citrate system buffered with sodium bicarbonate. Clays Clay Miner. 7, 317–327.

Payne, T.E., Davis, J.A., Waite, T.D., 1994. Uranium retention by weathered schists - the role of iron minerals. Radiochim. Acta 66-7, 297-303.

Rennert, T., Mansfeldt, T., Totsche, K.U., Greef, K., 2003. Sorption and transport of iron-cyanide complexes in goethite-coated sand. Soil Sci. Soc. Am. J. 67, 756-764.

Roden, E.E., Urrutia, M.M., Mann, C.J. 2000. Bacterial reductive dissolution of crystalline Fe(III) oxide in continuous-flow column reactors. Appl. Environ. Microbiol. 66, 1062-1065.

Scheidegger, A., Borkovec, M., Sticher H., 1993. Coating of silica sand with goethite - preparation and analytical identification. Geoderma 58, 43-65.

Scheidegger, A., Burgisser, C.S., Borkovec, M., Sticher,H., Meeussen, H., Van Riemsdijk,W., 1994. Convective-Transport of Acids and Bases in Porous-Media. Water Resour. Res. 30, 2937-2944.

Schwertmann,U., Cornell, R.M., 2000. Iron Oxides in the Laboratory,. Wiley-VCH, Weinheim. pp. 67-92.

Waite, T.D., Davis, J.A., Payne, T.E., Waychunas, G.A., Xu, N., 1994. Uranium(VI) adsorption to ferrihydrite - application of a surface complexation model. Geochim. Cosmochim. Acta 58, 5465-5478.

Weng, L., Temminghoff, E.J.M., Van Riemsdijk, W.H. 2001. Contribution of individual sorbents to the control of heavy metal activity in sandy soil. Environ. Sci. Technol. 35, 4436-4443.

Um, W.R.J.S., Christopher F. Brown, George V. Last. 2007. U(VI) adsorption on aquifer sediments at the Hanford site. J. Contam. Hydrol. 93, 255-269.

Xu, Y., Axe, L., 2005. Synthesis and characterization of iron oxide-coated silica and its effect on metal adsorption. J. Colloid Interface Sci. 282, 11-19.

3. Scaling of Adsorption Reactions in Batch systems: U(VI) Experiments and Modeling

3.1 Introduction

Scaling is defined as the process of using observations made at one set of spatial and temporal scales to understand processes or postulate behaviors at another set of scales (Whipple et al., 2001). The experimental scales include the micrometer scale biogeochemical studies (microbial, colloidal), bench scale experiment adsorption studies (batch, transport scenarios in 1D column, 2D box, and 3D tank experiments), and more rarely field-scale vadose zone experiments. More often the data obtained from these experiments are used for predicting the long-term scenarios without considering their scale and the inherent limitations. The classic case of using a constant distribution coefficient obtained from batch experiments in transport models is a typical example. Hence, it is important to address the scaling issues observed in simple systems operative at centimeter/meter scale in the laboratory before solving the large-scale field transport problems that ranges in kilometer/mile scales.

Prikryl et al. (2001) showed experimental evidence of U(VI) adsorption onto silicate mineral mixtures that scaled to surface area. Similarly, Jang et al. (2007) developed a surface complexation model for U(VI) adsorption onto HFO and showed that the same model could describe the adsorption onto pure Fe oxide minerals like hematite if adjusted for the specific surface area of the minerals. However, the above studies did not show the application of scaling principles onto Fe oxide-coated media that are common in the environment.

Surface complexation models (SCM) have frequently been used to describe the adsorption of U(VI) to Fe oxides. A number of different models have proven capable of adequately simulating the adsorption of U(VI) onto a particular Fe oxide under a range of conditions (Cheng et al., 2004; Hsi and Langmuir, 1985; Jang et al., 2007; Waite et al., 1994). However, our review indicates that there is no unique set of parameters or surface complexation reactions that can describe the adsorption processes of U(VI) to a specific Fe oxide. Mathur and Dzombak (2006) have compiled an extensive database for metal and anion adsorption onto goethite and found similar intrinsic surface complexation constants for hydrous ferric oxide (HFO) and goethite. Hence, they suggested that adsorption onto different Fe oxides would be similar provided that the site density and surface area, which are typically higher for HFO than for goethite, were taken into account.

The study of Xu and Axe (2005) shows that surface area normalized adsorption of nickel onto pure goethite and goethite-coated sand could be different indicating that pure minerals and media coated with these minerals can behave quite differently. Accordingly, we focus on U(VI) interactions with laboratory-synthesized Fe oxide-coated sand under well-controlled conditions as an intermediate between pure Fe oxides and Fe-containing soils and sediments. As opposed to natural geomedia, Fe-coated sands synthesized in the laboratory under well-controlled conditions avoid other materials and species [e.g., pre-adsorbed phosphate (Bostick et al., 2002)] that can influence adsorption. Understanding the adsorption of U(VI) onto coated sands is an important step towards developing scalable reaction models that can ultimately describe and predict the fate and transport of U(VI) in the subsurface.

In this study, we hypothesize that the adsorption of U(VI) to Fe coated sand is predominantly a surface-area driven process as opposed to an Fe content-driven process. To test our hypothesis, we synthesized and characterized Fe coated sands and conducted U(VI) adsorption experiments under well-controlled conditions. The experimental data describing the interaction of Fe coated sand with U(VI) were tested by two different scaling approaches using SCM to verify our hypothesis.

3.2 Materials and Methods

Batch adsorption experiments:

Both isotherm and pH adsorption edge experiments were performed to identify the critical parameters involved in scaling U(VI) adsorption to the coated sands (Table 3.1). The experiments were conducted with three coated sands prepared using the precipitation method (PT–1, PT–2, and PT–3, see Chapter 2), which were sequentially coated to obtain increasing levels of Fe content (0.04%, 0.18%, and 0.32%, respectively). The measured surface areas of these coated sands are shown in Table 3.2. Since the coated sand from the adsorption method (AD-1, Chapter 2) had a low specific surface area (due to the lower, more crystalline Fe content), the surface area of quartz contributed significantly to the overall surface area. To keep the influence of quartz on U(VI) to a minimum, we chose the coated sand from the precipitation method to perform the scaling experiments. Batch adsorption isotherms were measured at relatively low pH (~4.5) in order to maintain a stable pH without the use of pH buffers and to minimize the influence of atmospheric CO_2(g), both of which could influence U(VI) adsorption. This pH is also similar to U(VI)-contaminated sediments at some U. S. Department of Energy facilities (Barnett et al. 2000). Uranium stock solutions were prepared from depleted uranyl nitrate salt (Alfa Aesar, MA). The primary working stock solutions were prepared in 10^{-3} M nitric acid. The initial concentration of U(VI) was varied between 0 (blank controls) to 5 μM in 40 mL polycarbonate tubes. The pH and ionic strength of the system were fixed at 4.45 ± 0.1 and 0.1 M with HNO_3 and $NaNO_3$, respectively. All the experiments were performed at room temperature (~ 21 ± 1°C). An equilibrium time of 48 hours was chosen based on the results of previous studies (Cheng et al., 2004; Giammar and Hering, 2001). After equilibration, the samples were filtered using 0.45 μm polytetrafluoroethylene filter units, acidified to pH 1, and analyzed using a kinetic phosphorescence analyzer (KPA, Chemchek Instruments, Inc. WA).

Table 3.1 Experimental setups

System	pH in 0.1 M $NaNO_3$	Loading		Total U(VI)
		(g Fe L^{-1})	(g sand L^{-1})	(μM)
	Batch isotherm experiment			
PT–1	4.45 ± 0.1	0.174	436	0 – 5
PT–2	4.45 ± 0.1	0.167	91.9	0 – 5
PT–3	4.45 ± 0.1	0.158	50.2	0 – 5
	pH edge experiment			
PT–1	3 – 8	0.158	396	4.2
PT–2	3 – 8	0.158	86.7	4.2
PT–3	3 – 8	0.158	50.2	4.2

Table 3.2 Iron content and surface area of coated sands

System	DCB Fe content	AOD Fe content	Surface Area	Surface Area
	(% of coated sand)	(% of coated sand)	$m^2\ g^{-1}$ of FeOOH	$m^2\ g^{-1}$ of Fe [a]
AD–1	0.021 ± 0.001	0.0030 ± 0.0003	95.5	152
PT–1	0.040 ± 0.001	0.0063 ± 0.0001	223.1	355
PT–2	0.182 ± 0.005	0.0151 ± 0.0003	135.8	216
PT–3	0.315 ± 0.007	0.0123 ± 0.0003	105.6	168
Quartz	n/a	n/a	n/a	n/a
Goethite	61.4 ± 0.9 (62.8[b])	3.40 ± 0.08	53.3	84.8

c. Ignoring surface area of quartz.

d. Theoretical value.

AD represents coated sand synthesized using adsorption method.

PT represents coated sand synthesized using precipitation method.

The pH adsorption edges were performed at a fixed total U(VI) concentration of 4.2 μM. During pH adjustment, humidified N_2(g) was passed through freshly prepared 0.1 M NaOH and bubbled into the test tubes to avoid CO_2(g) contamination. The interaction of U(VI) to Fe oxides is greatly influenced by the presence of carbonate, which forms both aqueous and surface complexes with U(VI) (Clark et al., 1995; Wazne et al., 2003; Phillippi et al., 2007), so particular care was taken to avoid CO_2(g) in the experiments at pH >4.5. The solid-to-solution ratio was adjusted such that all the batches had similar Fe content (Table 3.1) but different reactive surface areas. In all experiments, blanks and controls were included.

Modeling:

Although there are other U(VI) surface complexation models for goethite (Missana et al., 2003; Van Geen et al., 1994; Villalabos et al., 2001), Waite et al's (1994) model has successfully been used to describe the adsorption behavior of U(VI) onto both amorphous and crystalline Fe oxides (Romero-Gonzalez et al., 2007). Moreover, the model was previously tested on systems that used natural Fe-coated media as the adsorbent (Logue et al., 2004; Barnett et al., 2002). A preliminary analysis of several different surface complexation models revealed that the model of Waite et al. (1994) was best able to predict our results over the entire data range. The exercise included using Waite et al's (1994) model to predict literature data sets that used U(VI) adsorption onto goethite (Fig. 3.1). Based on spectroscopic evidence, Waite et al. (1994) reported that U(VI) adsorbed to ferrihydrite as an inner-sphere, bidentate surface complex with two different U-O equatorial bond distances. A similar coordination environment for U(VI) interacting with goethite was subsequently confirmed by Moyes et al. (2000). Based on these studies, Waite et al's (1994) model was chosen for our study.

The bidentate surface complex reaction of U(VI) adsorption onto ferrihydrite involves one mole of uranyl cation occupying two surface sites as shown in the reaction below.

$$\begin{matrix} > FeOH \\ > FeOH \end{matrix} + UO_2^{2+} = \begin{matrix} > FeO \\ > FeO \end{matrix}\rangle UO_2 + 2H^+ \qquad (3.1)$$

Whereas the stability constant is proportional to first order of the surface site (reaction 3.2).

$$K = \frac{[(> FeO)_2 UO_2^0][H^+]^2}{[UO_2^{2+}][> FeOH]} \qquad (3.2)$$

The above scenario requires input of separate mass action and mass balance stoichiometric coefficients. Hence, simulations were run using a modified MICROQL code (Westall, 1979a, 1979b) that allows for the specification of separate mass-action and mass-balance stoichiometric coefficients that are required by the model. The difference between the model predictions and experimental data was quantified using the root mean square error (RMSE).

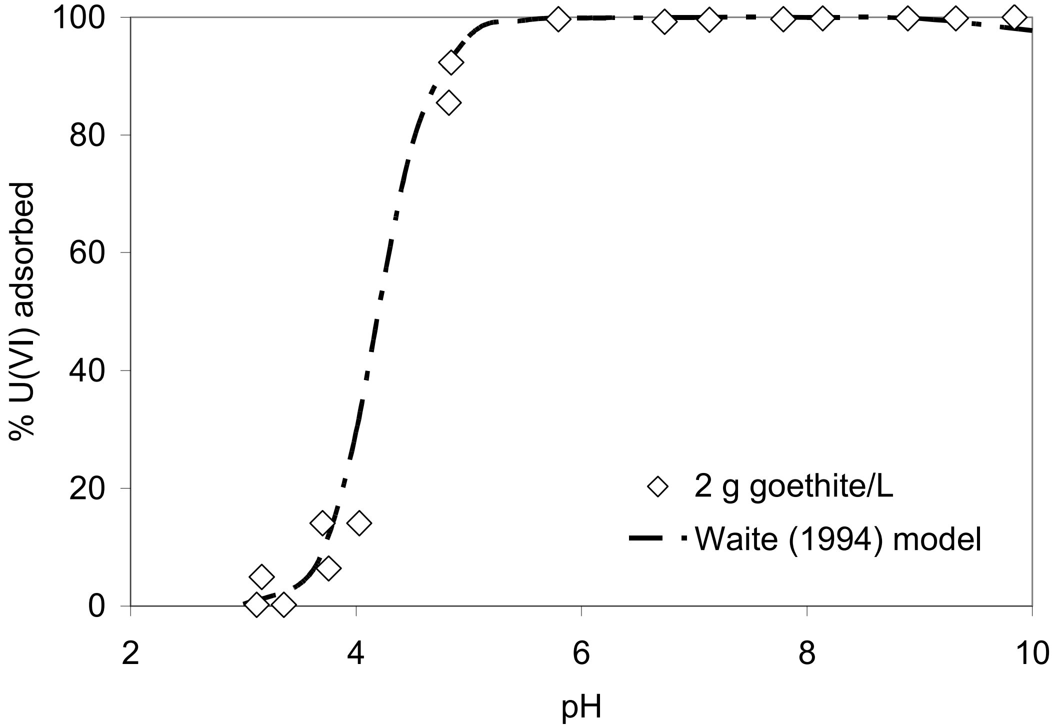

Figure 3.1 Prediction of literature dataset using Waite et al. (1994) model. The data of U(VI) adsorption on to pure goethite from Missana et al. (2003) is used here.

$$RMSE = \left(\frac{1}{n_d - n_p} \sum_{i=1}^{n_d} \left(\frac{C_i - \hat{C}_i}{C_0} \right)^2 \right)^{1/2} \tag{3.3}$$

where n_d is the number of data points, n_p is the number of adjustable parameters (zero in this case as the model was used in a purely predictive mode), i is an index, C and $\hat{C}$ are the measured and predicted aqueous equilibrium concentration (mol L^{-1}) at a total (solid + aqueous) concentration of C_0 (mol L^{-1}), respectively.

3.3 Results and Discussion

Experimental adsorption results:

The adsorption isotherms of the sands coated by the precipitation method are shown in Figure 3.2. Differences in the adsorption isotherms were observed, even after the U(VI) adsorption was normalized to Fe content (Fig. 3.2a). Sand PT–1 had approximately eight times less Fe than PT–3, but approximately twice the surface area per mole of Fe. As a result, the adsorption of U(VI) per mole of Fe was highest to PT-1 and lowest to PT-3. However, when the adsorption was scaled based on surface area rather than Fe content, very similar isotherms were obtained (Fig. 3.2b). Scaling based on surface area rather than Fe content minimizes the differences in surface area-driven adsorption between crystalline and amorphous Fe oxides.

The relative adsorption of U(VI) as a function of pH also varied between the sands (Fig. 3.3a). Note that by varying the mass of sand, the total Fe content of each experimental system was the same (0.158 g L^{-1}). As the U(VI) and Fe content of each system were approximately the same, if adsorption was governed solely by the Fe content, the percentage of U(VI) adsorbed in each system at a given pH should be the same (i.e., the curves in Fig. 3.3a should overlap).

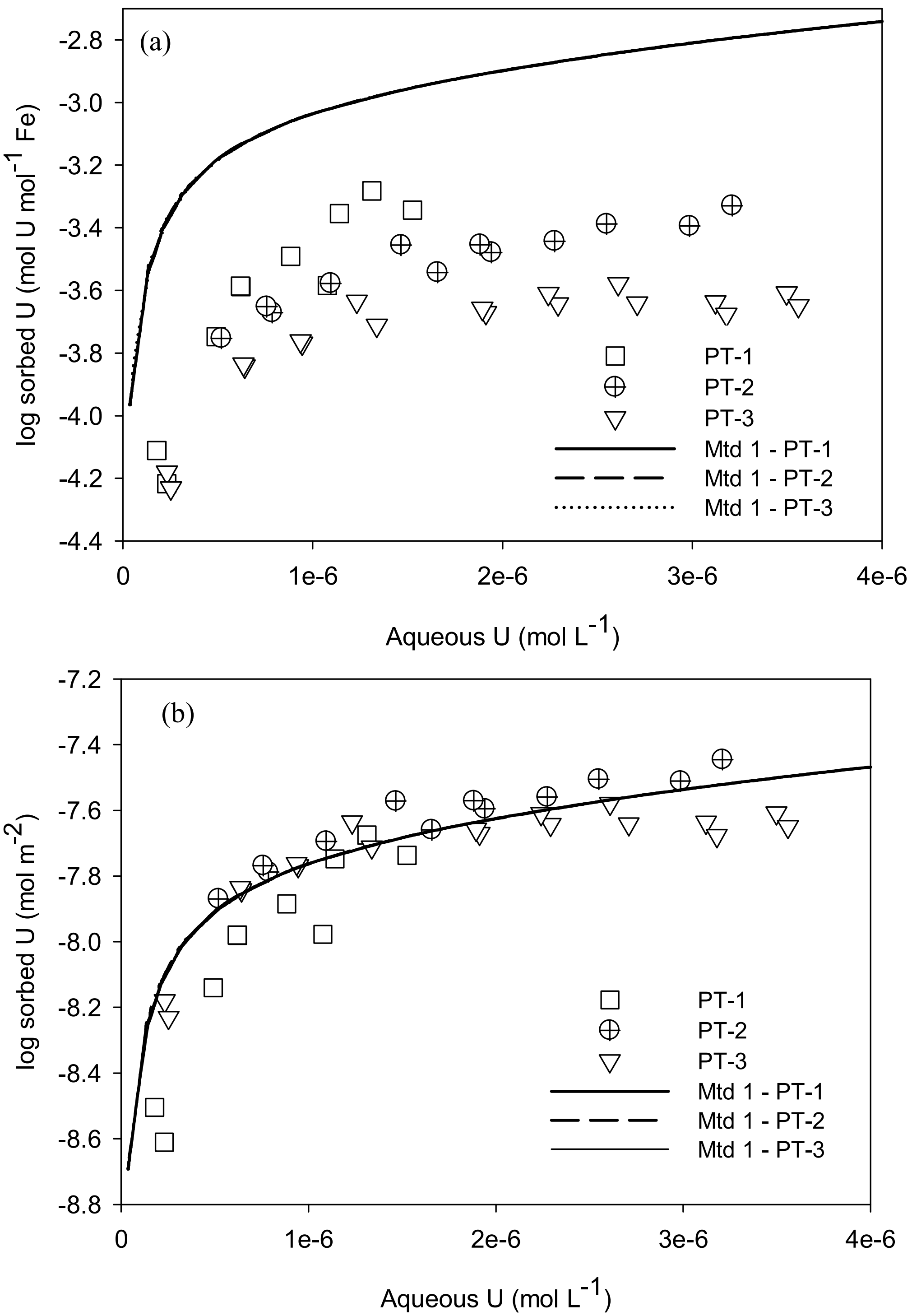

Figure 3.2 Adsorption of U(VI) to coated sand at pH 4.45 ± 0.1 and ionic strength of 0.1 M. (a) scaled to iron content; (b) scaled to specific surface area. The lines represent the scaled model prediction by method 1.

However, the adsorption of U(VI) to PT-1 was higher when compared to PT-2 and PT-3 as indicated by the shift in the pH adsorption curve towards the left. The higher degree of adsorption of PT-1 was again consistent with a larger fraction of amorphous Fe and corresponding larger specific surface area, although the adsorption of U(VI) to PT-2 and PT-3 were similar.

Similarly, differences in adsorption between the systems were observed, especially between PT-1 and the other sands, when the results were normalized to Fe (Fig. 3.4a). However, all three pH adsorption edges were similar when normalized to surface area (Fig. 3.4b).

We tested the hypotheses of scaling U(VI) adsorption onto Fe-oxides using the surface area on published datasets. The surface area normalized adsorption of U(VI) onto hematite and goethite from Jang et al (2007) is shown in figure 3.5a. Further, Logue et al's (2004) study on the adsorption of U(VI) onto natural sands rich in iron content was normalized to surface area and shown here in figure 3.5b. Both the literature datasets support our hypothesis of normalization of U(VI) adsorption based on the measured surface area.

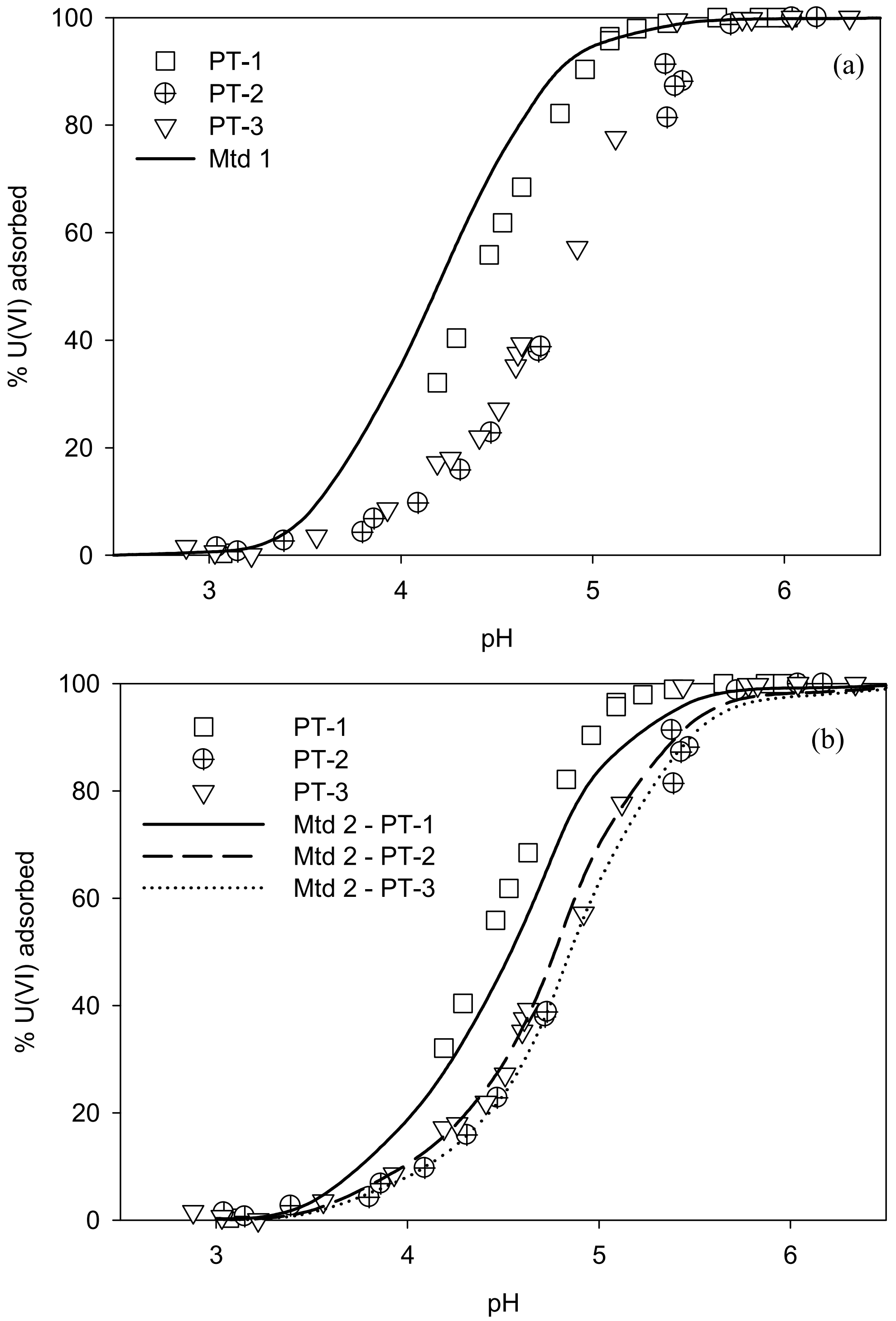

Figure 3.3 U(VI) adsorption edges onto coated sand at a total initial U(VI) concentration of 4.2 μM and ionic strength of 0.1 M; (a) Model prediction by method 1; (b) Model prediction by method 2.

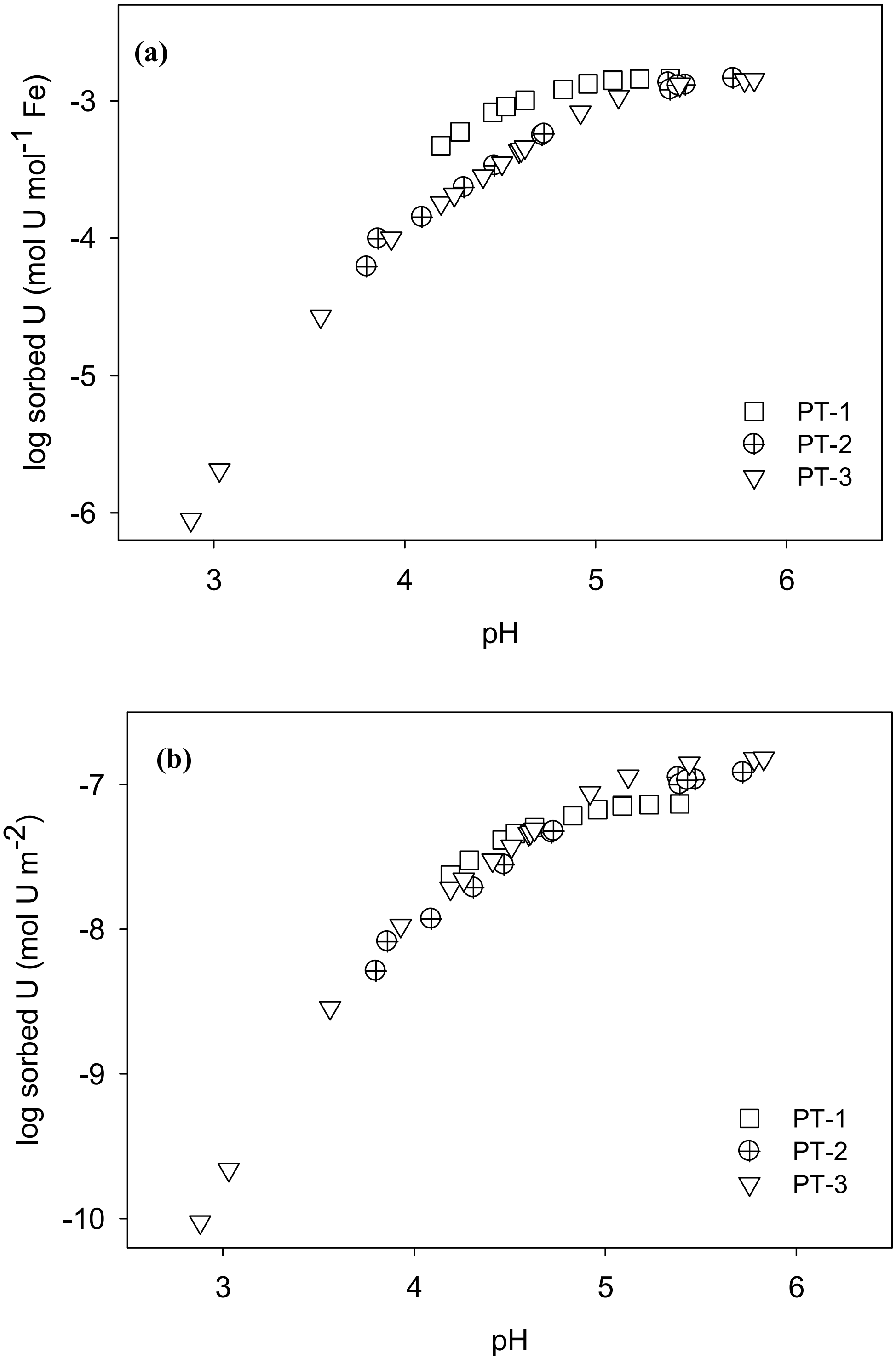

Figure 3.4 U(VI) adsorption edges onto coated sand at a total initial U(VI) concentration of 4.2 µM and ionic strength of 0.1 M; (a) Experimental data when scaled to iron content; (b) Experimental data when scaled to specific surface

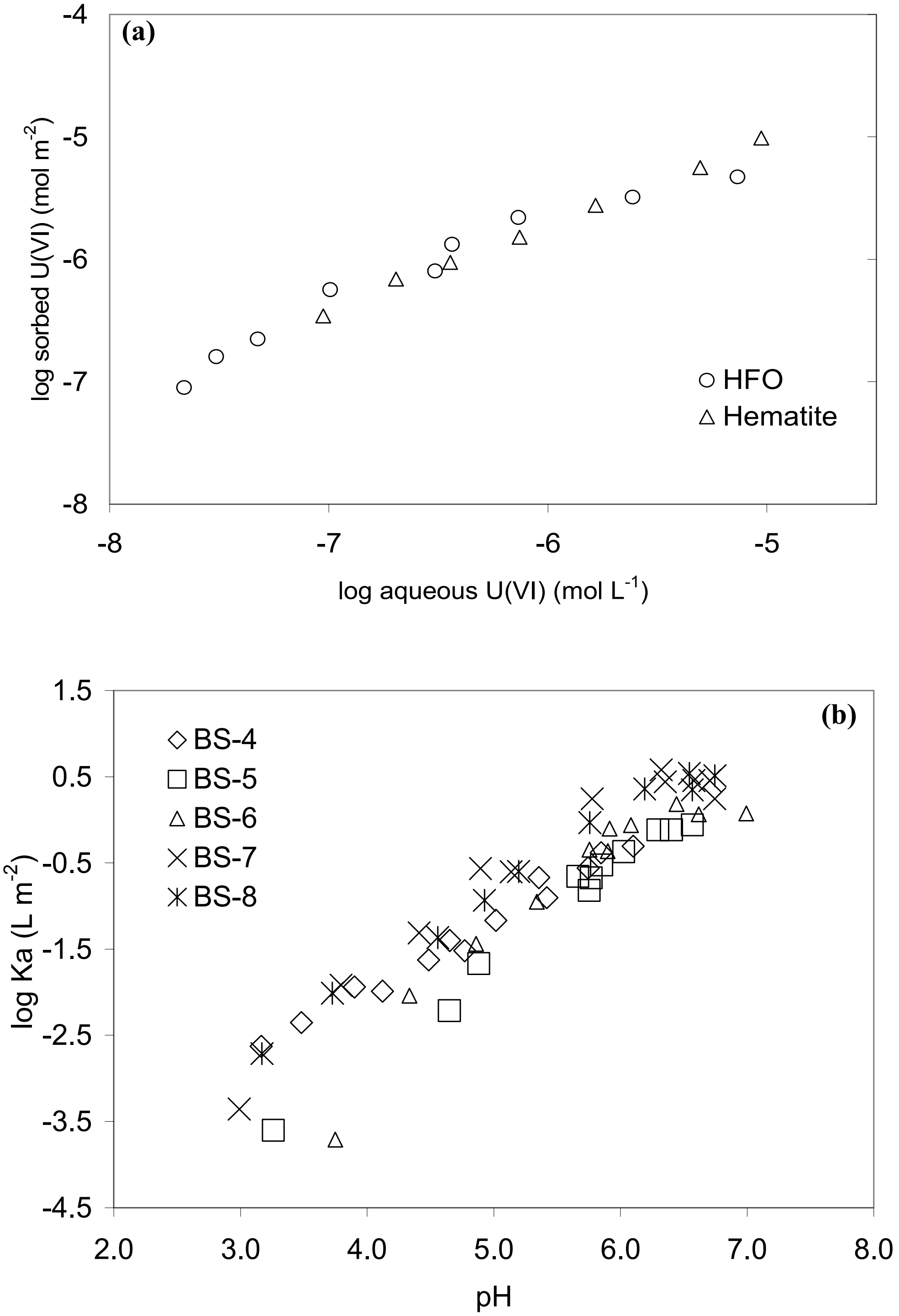

Figure 3.5 (a) Adsorption of U(VI) on to HFO and hematite when normalized to surface area (Jang et al.,2007). (b) Adsorption of U(VI) on to natural sands when normalized to surface area (Logue et al.,2004).

Modeling:

The diffuse double layer model developed by Waite et al. (1994) was used in a predictive mode to model our data. The reactions and constants used in the model are given in Table 3.3. The model was developed from U(VI) adsorption data on HFO with a nominal specific surface area of 600 m^2 g^{-1} and assumes adsorption of U(VI) onto two types of sites (strong and weak). The ratio of weak sites to strong sites specified in the model is ca. 485 with the site density being 0.8732 mole of weak sites per mole of Fe and 0.0018 mole of strong sites per mole of Fe. As the model was developed for amorphous HFO, it serves as a test of our hypotheses that adsorption of U(VI) to both amorphous and crystalline Fe oxides is approximately the same after correcting for surface area. Using the reported site density, specific surface area, molecular mass of HFO, and Avogadro's number, the surface site density was calculated to be 2.03×10^{-2} and 9.86 sites per nm^2 for strong and weak sites, respectively. The site density of pure goethite could range between 2.6 – 16.8 sites/nm^2 (Davis and Kent, 1990). A total site density of 10 sites per square nanometer was suggested by Hayes et al. (1991) for goethite based on potentiometric titration data supporting our hypothesis. For Fe oxide coated sand that contains both crystalline and amorphous Fe minerals, using the same intrinsic surface complexation constants was supported by similar intrinsic surface complexation constants for both amorphous (HFO) and crystalline (goethite) Fe oxides reported by Mathur and Dzombak (2006).

Table 3.3 Reactions included in model (T=25 °C, I=0.1M). Adapted from Barnett et al. (2002) and Waite et al. (1994).

No	U(VI) Aqueous Complexation Reactions	Log K
1	$UO_2^{2+} + H_2O \leftrightarrow UO_2OH^+ + H^+$	-5.41
2	$UO_2^{2+} + 2H_2O \leftrightarrow UO_2(OH)_2^0 + 2H^+$	-12.23
3	$UO_2^{2+} + 3H_2O \leftrightarrow UO_2(OH)_3^- + 3H^+$	-20.00
4	$UO_2^{2+} + 4H_2O \leftrightarrow UO_2(OH)_4^{2-} + 4H^+$	-32.57
5	$3UO_2^{2+} + 5H_2O \leftrightarrow (UO_2)_3(OH)_5^+ + 5H^+$	-16.22
6	$4UO_2^{2+} + 7H_2O \leftrightarrow (UO_2)_4(OH)_7^+ + 7H^+$	-22.62
7	$2UO_2^{2+} + 2H_2O \leftrightarrow (UO_2)_2(OH)_2^{2+} + 2H^+$	-5.79
8	$3UO_2^{2+} + 7H_2O \leftrightarrow (UO_2)_3(OH)_7^- + 7H^+$	-31.29
9	$2UO_2^{2+} + H_2O \leftrightarrow (UO_2)_2OH^{3+} + H^+$	-2.44
10	$3UO_2^{2+} + 4H_2O \leftrightarrow (UO_2)_3(OH)_4^{2+} + 4H^+$	-12.25
11	$UO_2^{2+} + H_2CO_3^* \leftrightarrow UO_2CO_3^0 + 2H^+$	-6.80
12	$UO_2^{2+} + 2H_2CO_3^* \leftrightarrow UO_2(CO_3)_2^{2-} + 4H^+$	-15.90
13	$UO_2^{2+} + 3H_2CO_3^* \leftrightarrow UO_2(CO_3)_3^{4-} + 6H^+$	-26.45
14	$2UO_2^{2+} + 3H_2O + H_2CO_3^* \leftrightarrow (UO_2)_2CO_3(OH)_3^- + 5H^+$	-18.07
	Other Aqueous Reactions	
15	$H_2O \leftrightarrow H^+ + OH^-$	-13.78

	U(VI) Surface Complexation Reactions[a]	
16	$2>\mathrm{Fe_wOH} + \mathrm{UO_2^{2+}} \leftrightarrow (>\mathrm{Fe_wO})_2\mathrm{UO_2^0} + 2\mathrm{H^+}$	-6.28
17	$2>\mathrm{Fe_sOH} + \mathrm{UO_2^{2+}} \leftrightarrow (>\mathrm{Fe_sO})_2\mathrm{UO_2^0} + 2\mathrm{H^+}$	-2.57
	Other Surface Complexation Reactions[a]	
18	$>\mathrm{Fe_{s,w}OH} + \mathrm{H^+} \leftrightarrow >\mathrm{Fe_{s,w}OH_2^+}$	+6.51
19	$>\mathrm{Fe_{s,w}OH} \leftrightarrow >\mathrm{Fe_{s,w}O^-} + \mathrm{H^+}$	-9.13

[a] $>\mathrm{Fe_S}$ and $>\mathrm{Fe_W}$ represent strong and weak surface Fe sites respectively.

Scaling model:

There are two reasonable approaches to scale surface complexation models (Table 3.4). The first approach (Method 1) is on the basis of Fe content (mol sites mole $\mathrm{Fe^{-1}}$) and the specific surface area (600 $\mathrm{m^2\ g^{-1}}$ HFO) specified in the original model, regardless of any independent experimental surface area measurement. Method 1 is the default method for many common surface complexation models (Waite et al., 1994; Dzombak and Morel, 1990). The second approach (Method 2) is to scale to specific surface area while keeping the original model site density constant (sites $\mathrm{nm^{-2}}$), which necessarily changes the number of moles of sites per mole of Fe specified in the original model. These above two modeling approaches are similar to the so-called generalized composite (GC) and the component additivity (CA) approaches (Davis et al., 1998; Payne et al., 2004; Waite et al., 2000). Method 1 can be reconciled with GC method since a uniform surface area value (600 $\mathrm{m^2/g}$ of HFO) was assumed for both the crystalline and amorphous Fe. Method 2 is similar to CA approach since the measured surface area (theoretically shown to be the summation of crystalline and amorphous surface areas) was used. Moreover, method 2 assumes similar site density for both the crystalline and amorphous Fe.

We examined the two methods of scaling surface complexation models for sands PT-1, PT-2, and PT-3, and examples of each method are detailed in Table 3.4. The model predictions for the experimental isotherm data are shown in Figures 3.2 and 3.6. Using the default scaling approach prescribed in the original model (Method 1), the model over-predicted U(VI) adsorption on a per mole Fe basis (Fig. 3.2a), which is consistent with the lower, independently measured specific surface area than used in the original model. Although the model over-predicted the adsorption on a per mole Fe basis, when the results were expressed on a per m^2 basis, the model and data agreed quite well (Fig. 3.2b).

When scaled on the basis of the measured surface area rather than the Fe content alone (Method 2) the model was able to predict the results on both a per mole Fe (Fig. 3.6a) and per m^2 (Fig. 7b) basis within an RMSE of 11%. In this approach, the model was scaled based on the independently measured specific surface area and the site density specified in the original model (2.03×10^{-2} and 9.86 sites per nm^2 for strong and weak sites, respectively), and the results were considerably better than Method 1. In addition, scaling Method 2 was also superior to Method 1 when predicting the pH adsorption edges as indicated by the RMSE in Table 3.4. In the case of the pH adsorption edges (Fig. 3.3a), the scaled model (Method 2) correctly predicted the shift towards higher adsorption for the system with higher surface area as observed in the experimental data (Fig. 3.3b).

Table 3.4 Potential scaling methods and results

Method	System	Site density		Fe loading	Site concentration	RMSE	Total [U]/ Total Sites[b]
		Strong	Weak				
		mol sites mol^{-1} Fe		g Fe L^{-1}	mol sites L^{-1}		mol mol^{-1}
				Model parameters used for isotherms			
1	PT-1	0.0018	0.8732	0.174	2.73×10^{-3}	0.323	1.83×10^{-3}
	PT-2	0.0018	0.8732	0.167	2.62×10^{-3}	0.407	1.91×10^{-3}
	PT-3	0.0018	0.8732	0.158	2.48×10^{-3}	0.511	2.02×10^{-3}
2	PT-1	0.0007	0.3247	0.174	1.01×10^{-3}	0.115	4.95×10^{-3}
	PT-2	0.0004	0.1975	0.167	5.92×10^{-3}	0.057	8.45×10^{-4}
	PT-3	0.0003	0.1539	0.158	4.36×10^{-3}	0.036	1.15×10^{-3}
				Model parameters used for pH edges			
1	PT-1	0.0018	0.8732	0.158	2.48×10^{-3}	0.083	1.69×10^{-3}
	PT-2	0.0018	0.8732	0.158	2.48×10^{-3}	0.234	1.69×10^{-3}
	PT-3	0.0018	0.8732	0.158	2.48×10^{-3}	0.249	1.69×10^{-3}
2	PT-1	0.0007	0.3247	0.158	9.21×10^{-4}	0.107	4.56×10^{-3}
	PT-2	0.0004	0.1975	0.158	5.60×10^{-4}	0.030	7.50×10^{-3}
	PT-3	0.0003	0.1539	0.158	4.36×10^{-4}	0.049	9.63×10^{-3}

[a] 955 m^2 per gram of Fe translates to ~600 m^2 per gram of HFO.

[b] For the isotherms this ratio was calculated for the highest U(VI) concentration. A surface site density of 9.86 sites nm^{-2} of weak sites and 0.02 sites nm^{-2} of strong sites was used.

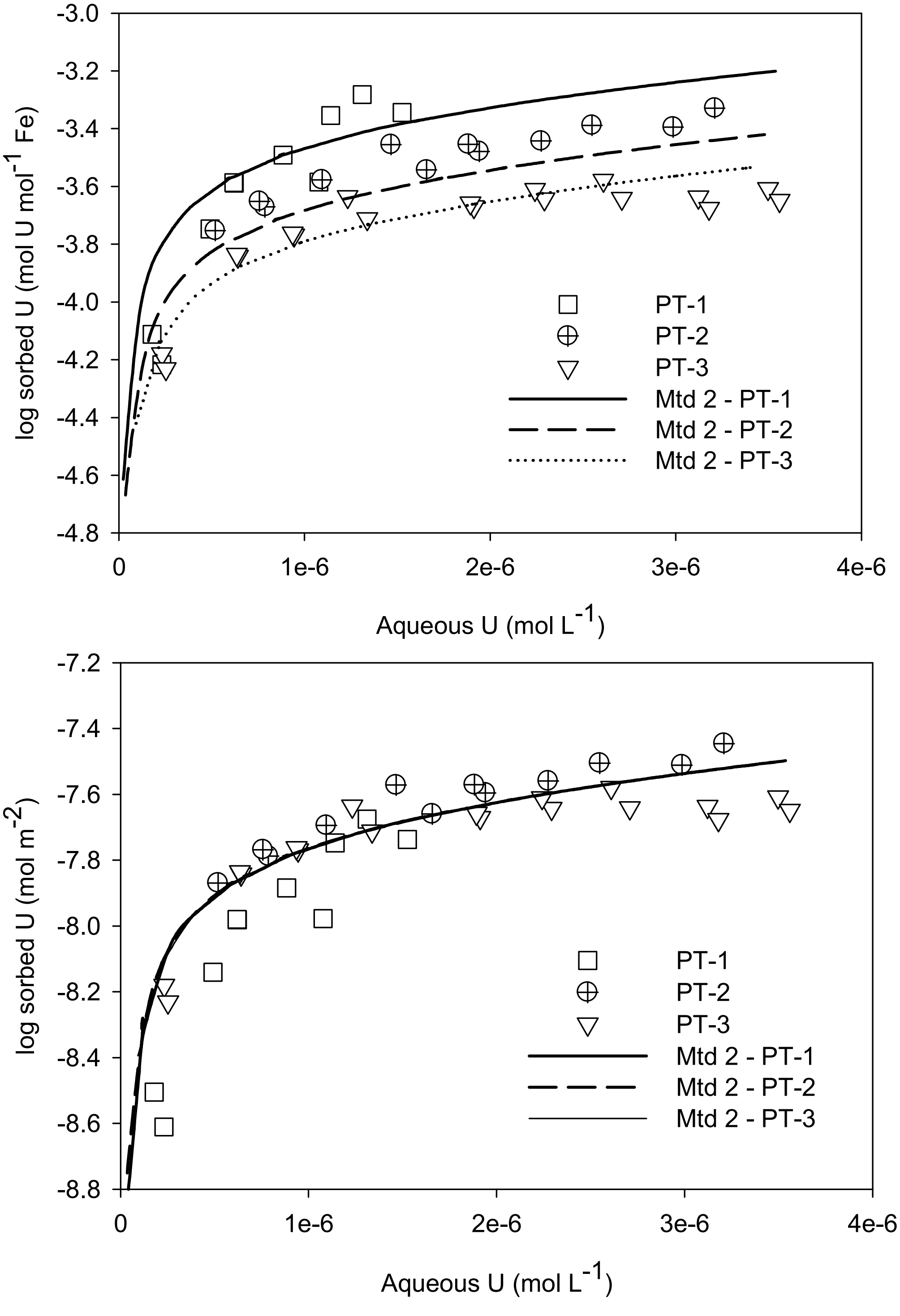

Figure 3.6 Scaled model prediction by method 2. (a) adsorption scaled to iron content; (b) adsorption scaled to specific surface area.

These results illustrate salient principles of adsorption scaling, as several common surface complexation models are parameterized only on a per molar Fe basis. Our findings show that U(VI) adsorption on Fe coated sand system representative of natural porous media scales better with surface area than Fe content alone. Moreover, the scaling processes can be predicted within the paradigm of surface complexation models.

3.4 Summary and Conclusions

U(VI) adsorption isotherms and pH adsorption edges were measured on three coated sands with Fe contents ranging from 0.04 to 0.3%. Experimentally, the adsorption of U(VI) onto the three sands was more comparable when normalized to surface area than when normalized to Fe content. We also examined the ability of several surface complexation models to predict our adsorption data. Although several different models could predict our data with a reasonable degree of accuracy, the model of Waite et al. (1994) predicted the complete range of data better than the other models we tested. As the model was developed for amorphous HFO, it also served as a test of our hypotheses that adsorption of U(VI) to both amorphous and crystalline Fe oxides is approximately the same after correcting for surface area.

Two different methods of scaling adsorption models were examined, an Fe content based method and a surface area based method. Consistent with the experimental data, scaling the adsorption model on the basis of surface area was the best approach. These findings are significant because many common surface complexation models are parameterized on the basis of Fe content rather than surface area. Finally, although the interactions of U(VI) and Fe coated sands were used as representative adsorbate and adsorbent, the general principles may be applicable to other adsorbate-adsorbent systems as well.

3.5 References

Barnett, M.O., Jardine, P.M., Brooks, S.C., Selim, H.M., 2000. Adsorption and transport of uranium(VI) in subsurface media. Soil Sci. Soc. Am. J. 64, 908-917.

Barnett, M.O., Jardine, P.M. and Brooks, S.C., 2002. U(VI) adsorption to heterogeneous subsurface media: Application of a surface complexation model. Environ. Sci. Technol. 36, 937-942.

Bostick, B. C., Fendorf, S. E., Barnett, M. O., Jardine, P. M., Brooks, S. C., 2002. Uranyl surface complexes formed on subsurface media from DOE facilities. Soil Sci. Soc. Am. J. 66, 99-108.

Cheng, T., Barnett, M.O., Roden, E.E., Zhuang, J.L., 2004. Effects of phosphate on uranium (VI) adsorption to goethite-coated sand. Environ. Sci. Technol. 38, 6059-6065.

Clark, D.L., Hobart, D.E., Neu, M.P., 1995. Actinide carbonate complexes and their importance in actinide environmental chemistry. Chem. Rev. 95, 25-48.

Davis, J.A., Kent, D.B., 1990. Surface complexation modeling in aqueous geochemistry. In: Hochella, M.F., White, A.F. (Ed.), Reviews in Mineralogy, 23, Mineralogical Society of America. pp. 177-260.

Davis, J.A., Coston, J.A., Kent, D.B., Fuller, C.C., 1998. Application of the surface complexation concept to complex mineral assemblages. Environ. Sci. Technol. 32, 2820-2828.

Dzombak, D.A., Morel, F.M.M, 1990. Surface complexation modeling: Hydrous Ferric Oxide. John Wiley & Sons.

Giammar, D.E., Hering, J.G., 2001. Time scales for sorption-desorption and surface precipitation of uranyl on goethite. Environ. Sci. Technol. 35, 3332-3337.

Hayes, K.F., Redden, G., Ela, W., Leckie, J.O., 1991. Surface complexation models an evaluation of model parameter-estimation using FITEQL and oxide mineral titration data. J. Colloid Interface Sci.142, 448-469.

Hsi, C.K.D., Langmuir, D., 1985. Adsorption of uranyl onto ferric oxyhydroxides - application of the surface complexation site-binding model. Geochim. Cosmochim. Acta 49, 1931-1941.

Jang, J.H., Dempsey, B.A., Burgos, W.D., 2007. A model-based evaluation of sorptive reactivities of hydrous ferric oxide and hematite for U(VI). Environ. Sci. Technol. 41, 4305-4310.

Logue, B.A., Smith, R.W., Westall. J.C., 2004. U(VI) adsorption on natural iron-coated sands: Comparison of approaches for modeling adsorption on heterogeneous environmental materials. Appl. Geochem.19, 1937-1951.

Mathur S.S., Dzombak, D.A., 2006. Surface complexation modeling: Goethite, In: Johannes Lutzenkirchen (Ed.), Surface complexation modeling. Elsevier, The Netherlands. pp. 443-468.

Missana, T., Garcia-Gutierrez, M., Maffiotte, C., 2003. Experimental and modeling study of the uranium (VI) sorption on goethite. J. Colloid Interface Sci. 260, 291-301.

Moyes, L.N., Parkman, R.H., Charnock, J.M., Vaughan, D.J., Livens, F.R., Hughes, C.R. Braithwaite, A., 2000. Uranium uptake from aqueous solution by interaction with goethite, lepidocrocite, muscovite, and mackinawite: An x-ray absorption spectroscopy study. Environ. Sci. Technol. 34, 1062-1068.

Payne, T.E., Davis, J.A., Ochs, M., Olin, M. and Tweed, C.J., 2004. Uranium adsorption on weathered schist - intercomparison of modelling approaches. Radiochim. Acta 9-11, 651-661.

Phillippi, J.M., Loganathan, V.A., McIndoe, M.J., Barnett, M.O., T.P. Clement, E.E. Roden. 2007. Theoretical solid/solution ratio effects on adsorption and transport: Uranium(VI) and carbonate. Soil Sci. Soc. Am. J. 71, 329-335.

Prikryl, J.D., Jain, A., Turner, D.R., Pabalan, R.T., 2001. Uranium(VI) sorption behavior on silicate mineral mixtures. J. Contam. Hydrol. 47, 241-253.

Romero-Gonzalez, M.R., Cheng, T., Barnett, M.O., Roden, E.E., 2007. Surface complexation modeling of the effects of phosphate on uranium(VI) adsorption. Radiochim. Acta 95:251-259.

Van Geen, A., Robertson, A.P. Leckie, J.O., 1994. Complexation of carbonate species at the goethite surface - implications for adsorption of metal-ions in natural-waters. Geochim. Cosmochim. Acta 58, 2073-2086.

Villalobos, M., Trotz, M.A., Leckie, J.O., 2001. Surface complexation modeling of carbonate effects on the adsorption of Cr(VI), Pb(II), and U(VI) on goethite. Environ. Sci. Technol. 35, 3849-3856.

Waite, T.D., Davis, J.A., Payne, T.E., Waychunas, G.A., Xu, N., 1994. Uranium(VI) adsorption to ferrihydrite - application of a surface complexation model. Geochim. Cosmochim. Acta 58, 5465-5478.

Waite, T.D., Davis, J.A., Fenton, B.R. and Payne, T.E., 2000. Approaches to modelling uranium(VI) adsorption on natural mineral assemblages. Radiochim. Acta 88, 687-693.

Wazne, M., Korfiatis, G.P., Meng, X.G., 2003. Carbonate effects on hexavalent uranium adsorption by iron oxyhydroxide. Environ. Sci. Technol. 37, 3619-3624.

Westall, J.C., 1979. MICROQL. I. A chemical equilibrium program in BASIC, Technical Report. Swiss Federal Institute of Technology, EAWAG, Dubendorf, Switzerland.

Westall, J.C., 1979. MICROQL. II. Computation of adsorption equilibria in BASIC, Technical Report. Swiss Federal Institute of Technology, EAWAG, Dubendorf, Switzerland.

Whipple, C.G., D.W. Berman, S.B. Clark, J.C. Fountain, L.W. Gelhar, L.C. Green, R.O. Hall, E.E. Herricks, B.D. Honeyman, S. Levy, J.K. Mitchell, L.T. Silver, L. Smith, and D.A. Stonestrom, Science and Technology for Environmental Cleanup at Hanford, National Academy Press, 2001. Review of the Hanford Site's Environmental Remediation Science and Technology Plan, Board on Radioactive Waste Management, National Research Council.185-193.

Xu, Y., Axe, L., 2005. Synthesis and characterization of iron oxide-coated silica and its effect on metal adsorption. J. Colloid Interface Sci. 282, 11-19.

4. Understanding the Adsorption Discrepancies between Batch and Column Scenarios

4.1 Introduction

In the early 1940's, the naturally occurring radioactive element, uranium, was heavily used in the nuclear weapons program and energy production. Ever since, the vast use of uranium has left a legacy of contaminants in the subsurface environment, especially at most of the U.S. Department of Energy (DOE) sites (Gee et al., 2007). Mainly, U is in the tetravalent (IV) or hexavalent (VI) state in the subsurface. The solubility of U(IV) is very low when compared to U(VI) and hence it is less mobile. Furthermore, the presence of oxic groundwater readily favors the conversion of U(IV) to U(VI), making U(VI) the most important form of uranium in groundwater.

Previous studies indicate that the sorption of U(VI) at contaminated sites occurs mainly onto metal oxides/oxy hydroxides. In particular, Fe(III) oxides/oxy hydroxides are found to be the dominant U adsorbing phase of geomedia (Um et al., 2007; Davis et al., 2004; Barnett et al., 2002). Various forms of Fe(III) oxides occur in nature and can be broadly classified into crystalline (e.g., goethite, hematite) and amorphous forms (e.g., hydrous ferric oxide, ferrihydrite). Crystalline Fe oxides exhibit lower specific surface area and microporosity compared to the non-crystalline, amorphous Fe oxides (Schwertmann and Cornell, 2000). At U(VI)-contaminated sites, Fe oxides often appear as coatings on other geomedia rather than discrete minerals (Davis et al., 2004; Payne et al., 1994; Um et al., 2007). In order to predict the field-scale transport of U(VI), its adsorption processes should be understood and be able to be scaled. Ultimately, this would also aid in the design of effective remediation strategies.

The critical parameter that describes the sorption of a contaminant to geomedia is typically obtained by performing batch sorption isotherms and is referred to as the distribution coefficient (K_d). Often, the simple laboratory-determined K_d fails to describe the field scale transport of contaminants (Relyea at al., 1980). Since the chemical conditions of the subsurface environment have a drastic influence on K_d, [e.g. a 0.5 unit change in pH can cause about 50% difference in the sorption of U(VI) onto geomedia (Barnett et al., 2000)], simple models of sorption (linear, Freundlich, Langmuir) may be replaced by surface complexation models (SCM). In the case of U(VI) adsorption to Fe oxides, a number of different SCM have proven capable of adequately simulating adsorption under a range of conditions (Cheng et al., 2004; Hsi and Langmuir, 1985; Jang et al., 2007; Waite et al., 1994).

More often, the adsorption of a solute onto the sorbent (either natural or laboratory synthesized) is quantified using batch scale experiments, which are then used to predict field-scale transport scenarios. One of the most perplexing and yet unresolved problems is the discrepancy observed between batch-derived and column-derived adsorption capacities. Even studies performed using pure mineral media/model sorbents showed such differences in sorption capacity. For example, Kohler et al. (1996) and Gabriel et al. (1998) reported batch-column discrepancies in U(VI) sorption onto pure quartz and goethite-coated sand, respectively. The issue could have serious implications when batch-measured sorption coefficients are used to estimate the retardation factor for field-scale U(VI) reactive transport.

The focus of this study is to understand the causes of the above problem using both a homogeneous synthetic adsorbent and a natural heterogeneous geomedia. The uncontaminated natural geomedia (designated OR) was acquired from Oak Ridge Reservation in East Tennessee, which is one of the primary DOE sites that is contaminated with U(VI). The OR soil used here is uncontaminated with respect to U(VI). The synthetic media, iron oxide-coated sand (IOCS), was prepared in the laboratory using the method described in Loganathan et al. (2009).

The two major objectives of this study were:

(i) To scale the adsorption reactions using U(VI) and iron oxide-coated sand as a model system.

(ii) To find the probable causes for the reported sorption discrepancies between the batch and column scales using both natural and synthetic media.

4. 2 Materials and Methods

Sorbate and sorbent:

U(VI) in the form of uranyl nitrate salt was used as the solute. The adsorbents used in this study were laboratory synthesized iron oxide-coated sand (IOCS) and Oak Ridge reservation soil. The IOCS was prepared using pure white quartz as a substrate onto which goethite (FeOOH) was coated using the precipitation method. The details of the coating protocol are discussed elsewhere (Loganathan et al., 2009). The iron content of the synthetic media thus obtained was measured using the dithionate-citrate-bicarbonate (DCB) method (Mehra and Jackson, 1960) and it is 0.431 ± 0.010 mg Fe g^{-1} of sand . The BET surface area of the sand was 0.107 m^2 g^{-1} as measured using N_2 gas.

Accounting for the surface area of quartz, the surface area of the coated sand on an Fe basis was calculated to be 164 m^2 g^{-1} Fe. The DCB Fe content of the OR soil was 24.6 ± 4.2 mg Fe g^{-1} of soil. The organic matter in OR soil was reported to be ca. 0.55 g kg^{-1} (Barnett et al., 2000). The extraction of phosphate from OR soil was performed using the Mehlich-1 method as outlined in Beck at al. (2004). Briefly, approximately 2 grams of OR soil was mixed with 0.0125M H_2SO_4 and 0.05M HCl for about 2 hours. At the end of the extraction phase, samples were centrifuged and filtered using 0.45 μm polytetrafluoroethylene filter units. The filtered samples were analyzed using ICP-OES.

Batch experiments:

Batch kinetic and isotherm experiments in IOCS were performed at two solid-to-solution ratios (SSR), 50 and 500 g L^{-1}. The ionic strength was fixed at 0.1 M using $NaNO_3$ and the experiments were performed at pH 5.0±0.2. In the case of OR soil, batch experiments were performed at low SSR's (1.67, 3.33, and 16.7 g L^{-1}) because of its higher Fe content.

1D-transport experiments:

Column experiments were performed in a 15 × 2.5 cm or 10 × 1.0 cm glass column. Preliminary experiments were performed in an empty column to check the adsorption of U(VI) to the glass column. In the case of IOCS, column experiments were performed at a pH of 4.9±0.2, wherein the background ionic strength was maintained at 0.1 M using $NaNO_3$, which is similar to the batch experimental conditions. In order to derive sorption isotherms from transport experiments, a multi-step column experiment was designed and conducted at a fixed pH and varying U(VI) concentration (1.05 – 5.25 μM), wherein

IOCS was used as the adsorbent. In the case of OR soil, as the Fe content of the OR soil is very high (ca. 2.4% Fe) strong sorption to U(VI) was expected. Hence to obtain breakthrough in a practical time frame, a smaller column (10 cm x 1.0 cm) was used, which was packed with 2 grams of OR soil. Since the natural pH of the OR soil was ~ 4.7, a similar pH condition (4.6-4.8) was maintained in both batch and column experiments without the use of any external buffers.

4.3 Results and Discussion

Batch experiments:

The adsorption kinetics of U(VI) onto IOCS at two different SSR is shown in Figure 4.1. In the case of low SSR (50 g L^{-1}) about 20% of the initial U(VI) [4.2 μM] was adsorbed within 15 days whereas at high (500 g L^{-1}) SSR about 80% of the initial U(VI) was adsorbed within 15 days. Based on the kinetic experiments, an equilibrium time of 3 days was chosen for the batch isotherm experiments. A lesser equilibrium time of 2 days was found to be sufficient for U(VI) experiments with OR soil (Barnett et al., 2000). The adsorption of U(VI) on to both IOCS and OR soil followed a typical Freundlich isotherm (Figs 4.2a and b).

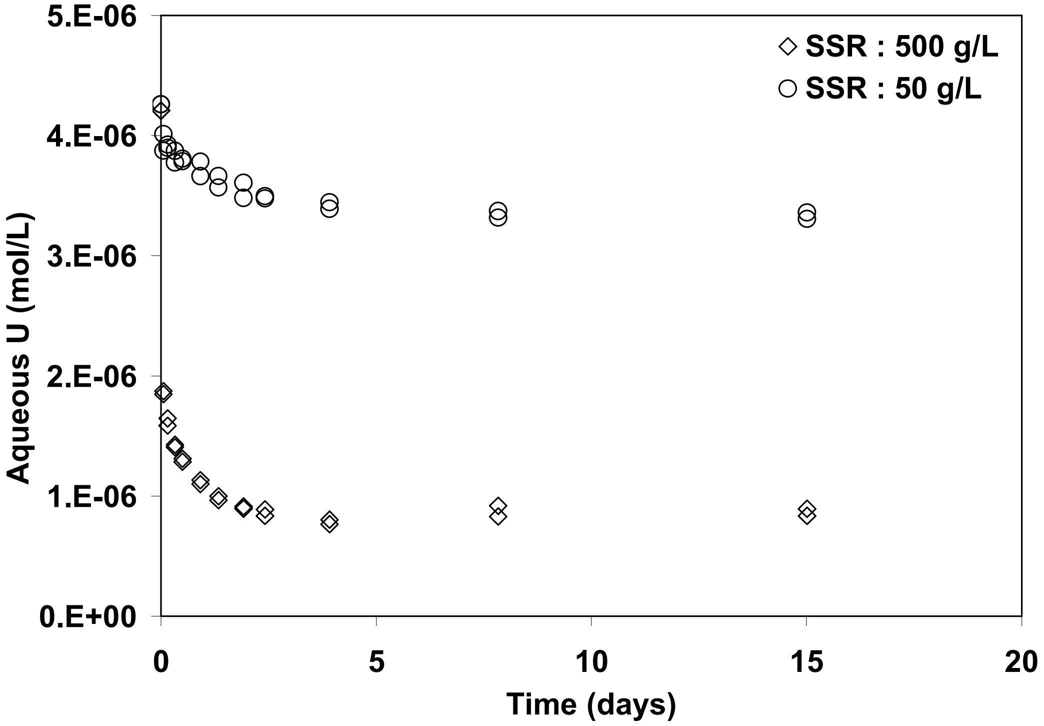

Figure 4.1 Batch kinetics of U(VI) adsorption onto IOCS at two different solid to solution ratios at pH 5.0 ± 0.2, I =0.1 M.

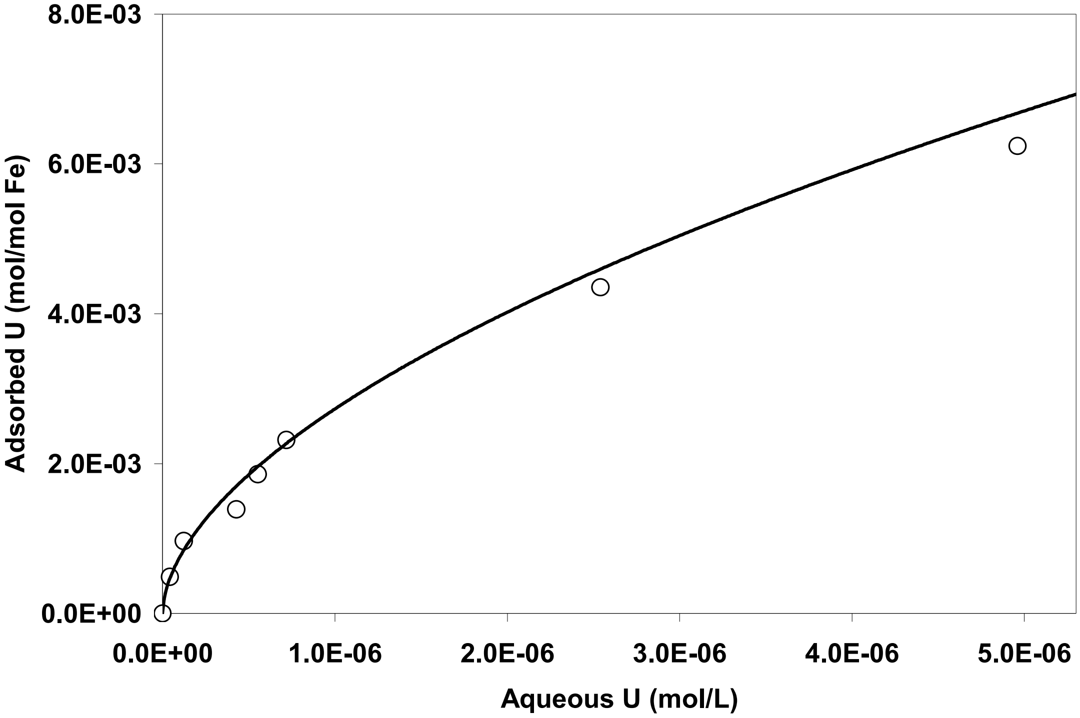

Figure 4.2a Batch adsorption isotherm of U(VI) on to IOCS (pH 5.0±0.2; I: 0.1 M).

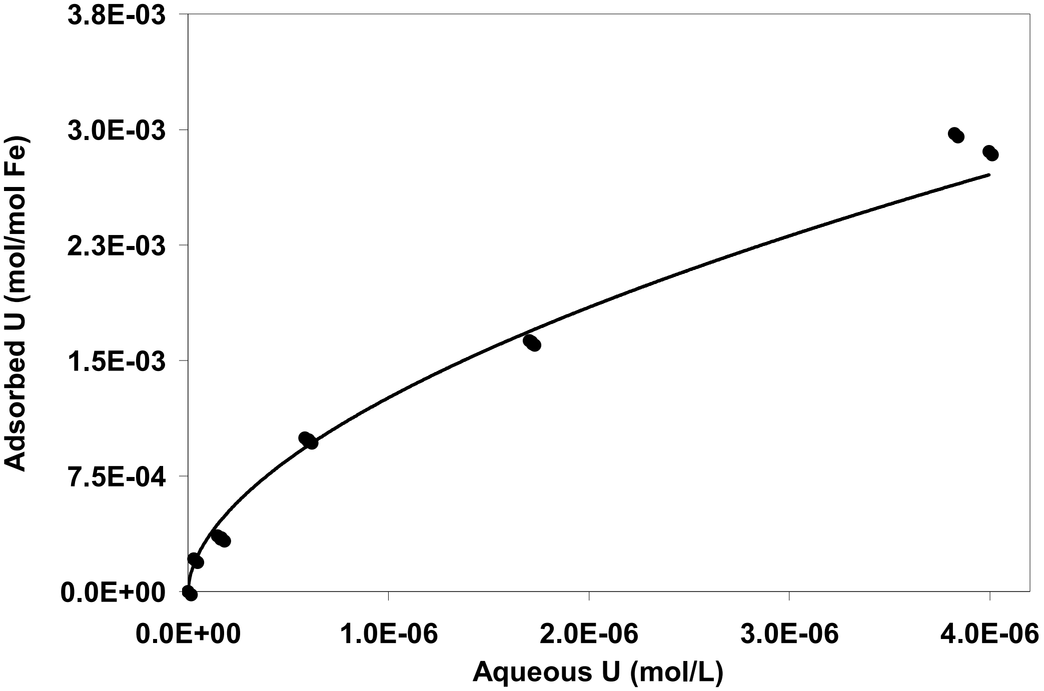

Figure 4.2b Adsorption isotherm of U(VI) onto Oak Ridge soil from batch experiment (pH 4.8±0.2; I :0.1 M; SSR: 3.33 g L^{-1}).

Column experiments:

The adsorption of U(VI) onto IOCS is shown in Figure 4.3a. The experiment was performed at very low flow rate of 4.2 mL hr^{-1}, resulting in a specific discharge of 0.09 cm min^{-1}. The U(VI) pulse of ~400 mL at a concentration of ca. 4.2 μM resulted in an adsorption of about 20% of the influent U(VI) mass. In the case of the OR soil, the input pulse required to achieve near saturation (C/C_0 = 0.9) was about 2800 pore volumes (Figure 4.3b). Although the OR soil column was packed with about 5 times less mass of sorbent, the huge difference in adsorption was mainly due to the higher amount of Fe in the OR soil.

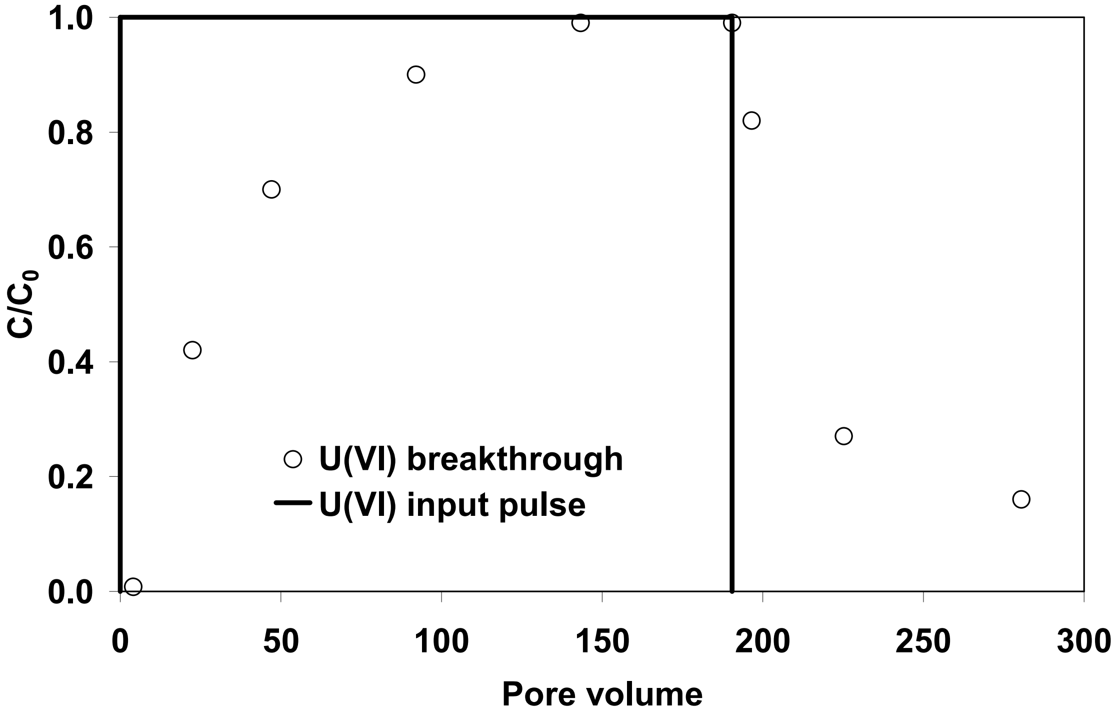

Figure 4.3a Breakthrough profile of U(VI) in IOCS column at a pH of 4.9 ± 0.2, I = 0.1 M; Flow rate = 4.2 mL hr^{-1}; C_0 = 4.2 E-6 M; Mass of IOCS in the column ~ 10 grams.

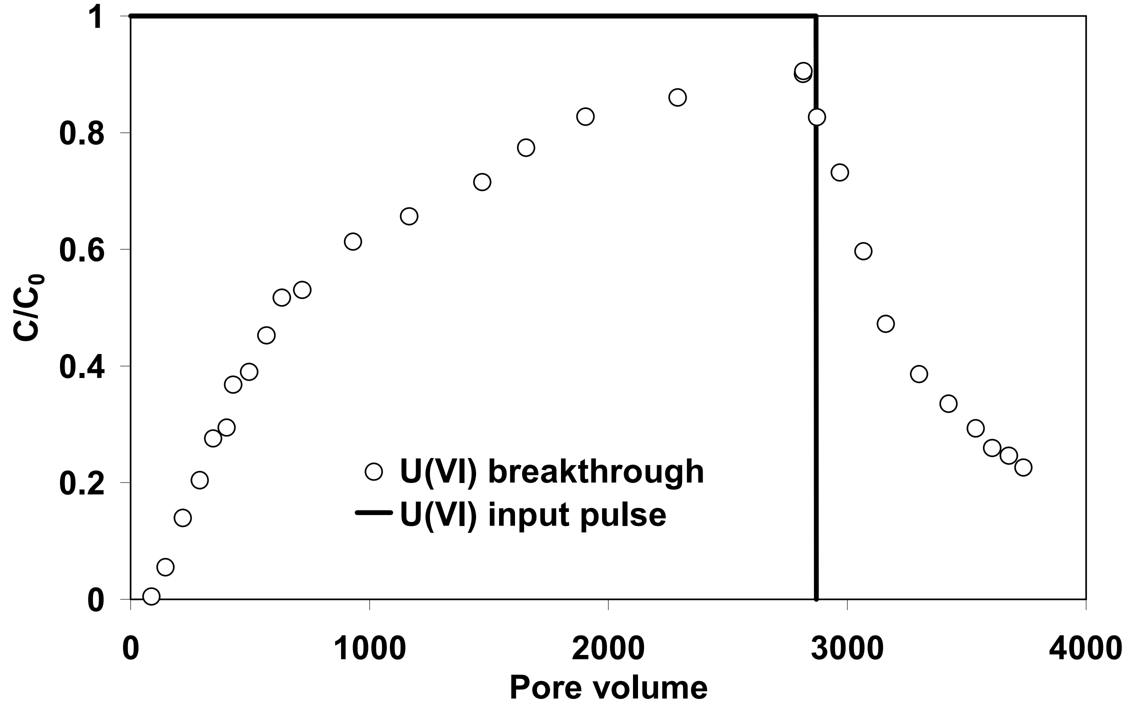

Figure 4.3b Breakthrough profile of U(VI) in OR soil packed column at an initial U(VI) concentration of ~4.2E-6 M (I: 0.1 M $NaNO_3$, pH: 4.7 ± 0.2)

A multi-step column experiment was performed using IOCS. The multi-step column experiment involved a step-wise increase in the influent concentration once the breakthrough at a given concentration was achieved. Figure 4.4 shows the overall breakthrough profile of the step-wise column experiment along with the influent U(VI) pulse indicated in solid lines. The adsorption of U(VI) at each step was calculated by fitting the breakthrough profile using linear interpolation of successive data points.

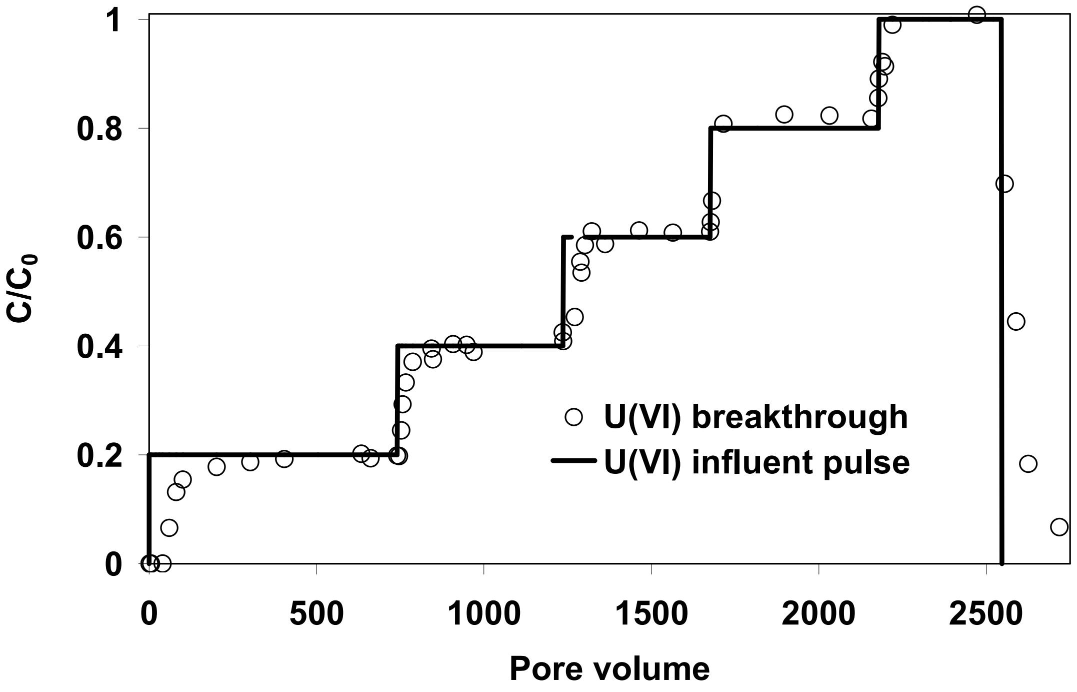

Figure 4.4 Breakthrough profile of U(VI) in IOCS column at a pH of 5.0 ± 0.2, I = 0.1 M; flow rate = 4.2 mL hr^{-1}; Mass of IOCS in the column ~ 10 grams.

The sorption capacity obtained from the multi-step column and the batch isotherm experiments indicate a similar adsorption capacity of U(VI) on to synthetic IOCS (Fig. 4.5a). Moreover, the batch U(VI) adsorption to IOCS obtained at two different solid-to-solution ratios (50 and 500 g L^{-1}) showed similar sorption. The results confirm that in the case of IOCS, the adsorption of U(VI) is independent of soild-to-solution ratio. Hence, in the case of IOCS, the sorption capacity obtained from the batch experiments correctly scales to column-observed sorption capacity (Fig. 4.5b). These results also confirm the lack of kinetic effects in our experimental scenario.

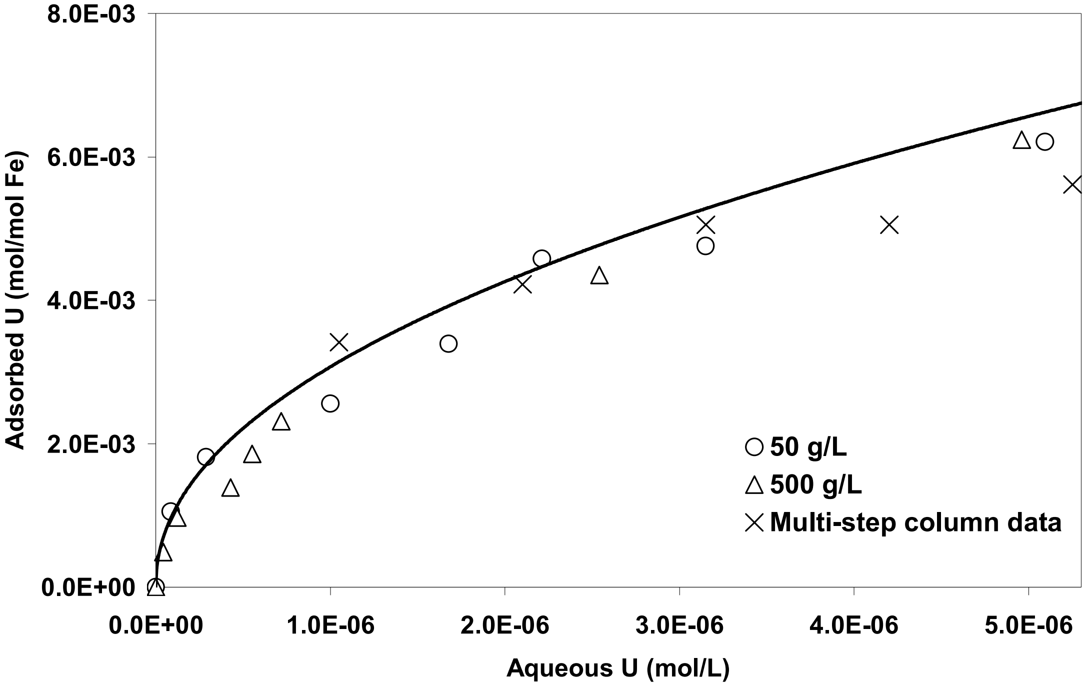

Figure 4.5a Effect of soil-to-solution ratio in U(VI) adsorption on to IOCS in batch (SSR: 50 g L^{-1} and 500 g L^{-1}) and column scenarios. pH 5.0 ± 0.2; I = 0.1 M $NaNO_3$.

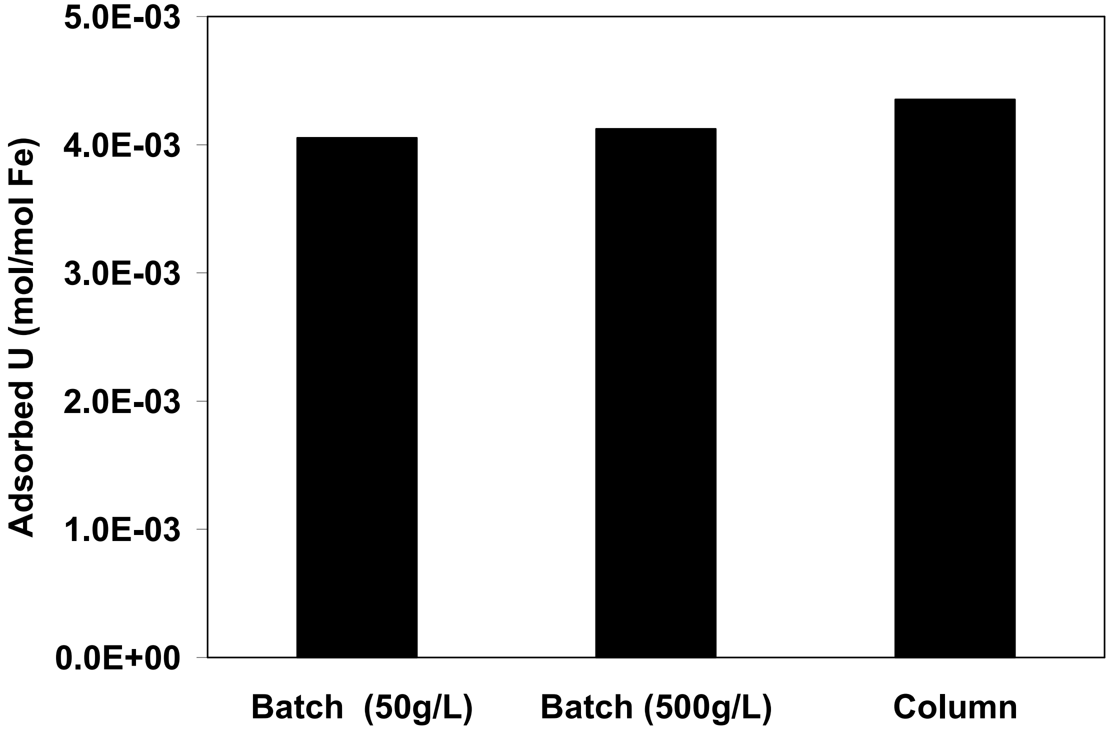

Figure 4.5b Comparison of U(VI) adsorption capacity derived from batch and column scenarios in IOCS system. Aqueous U(VI): 4.2E-6 M; pH ca. 5.0 (after Kurbatov correction); I: 0.1 M.

In the case of OR soil column experiments, a sorption capacity of ~ 5.77E-3 M U mol^{-1} of Fe was calculated based on the U(VI) breakthrough profile (Fig. 4.3b). When compared to the batch sorption capacity at the corresponding U(VI) concentration (Fig 4.6a), a 100% increase in adsorption capacity is observed in the 1D-column experiment. These results are contrary to the one observed on the IOCS and indicate the complex nature of heterogeneous media, but consistent with the result observed by Barnett et al. (2002).

Some of the possible causes for the above observed anomaly could be differing kinetic scenarios between batch and column environment, the presence of a competing solute/ligand, the difference in solid-to-solution ratio between the batch and column experiments, etc. All the experiments were performed at low flow rate conditions possible with the use of HPLC pumps. Further, based on the results from the IOCS column and batch experiment, kinetic effects could be ignored. To check the SSR effect in the OR soil, batch isotherms were obtained in systems that had an order of magnitude difference in SSR. The experiment resulted in two different Freundlich isotherms indicating the dependency of adsorption on SSR (Fig. 4.6a). The comparison between batch adsorption and column adsorption capacity for the OR soil at similar experimental condition is shown in Figure 4.6b.

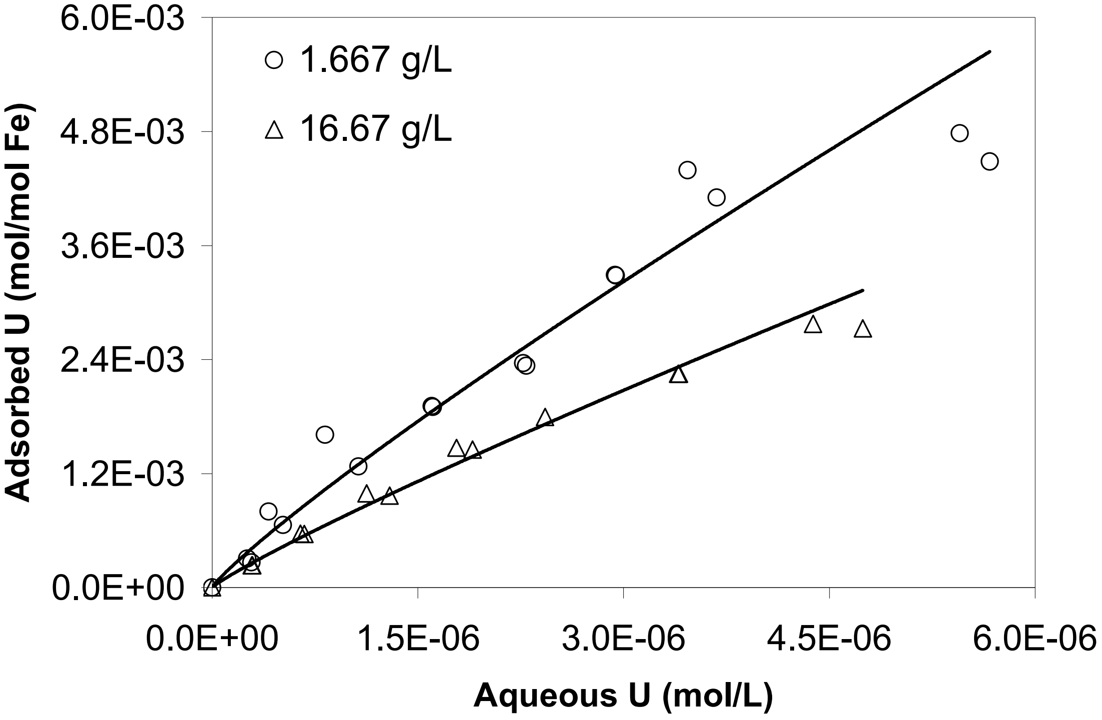

Figure 4.6a Effect of soil-to-solution ratio in U(VI) adsorption on to OR soil in batch (SSR: 1.667 g L^{-1} and 16.67 g L^{-1}) system. pH 4.6 ± 0.2; I = 0.1 M $NaNO_3$.

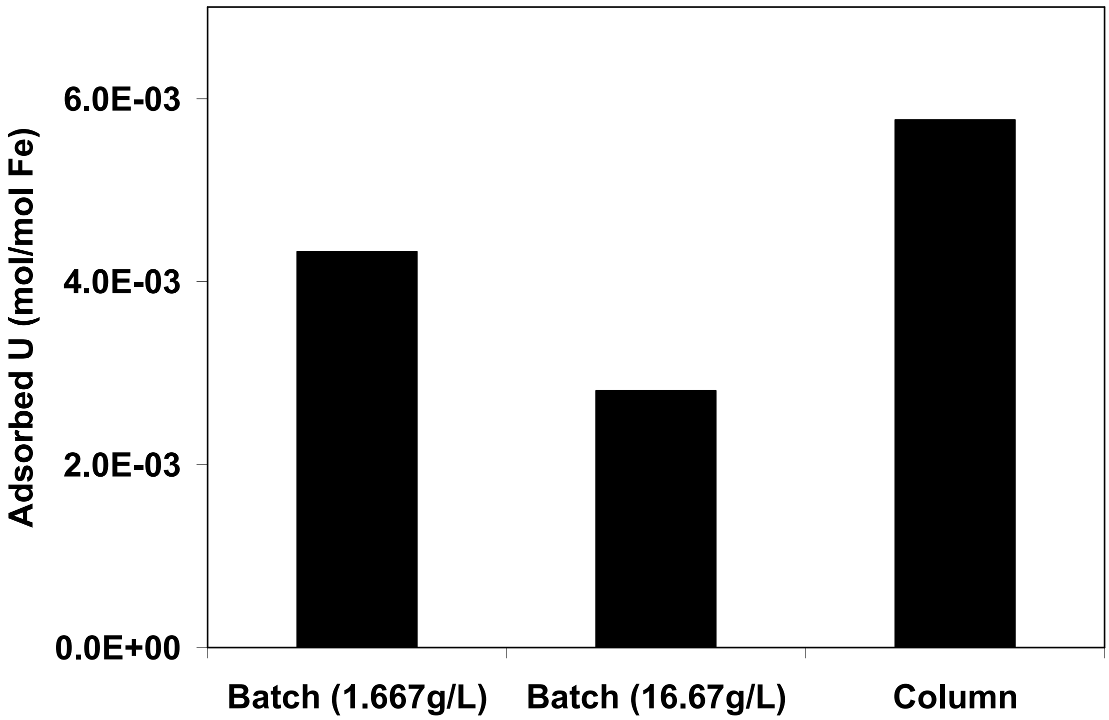

Figure 4.6b Comparison of U(VI) adsorption capacity derived from batch and column scenarios in OR soil system. Aqueous U(VI): 4.2E-6 M; pH ca. 4.6; I: 0.1 M.

Based on the trend in the adsorption (lower adsorption at higher SSR), the aqueous complexation of U(VI) by carbonate was eliminated. A theoretical study on the effect of solid-to-solution ratio on U(VI) adsorption in U(VI)-carbonate system should result in the opposite trend (Phillippi et al., 2007). Moreover, the OR soil had a low pH (ca. 4.7) and the soil has been characterized with the absence of carbonate minerals (Barnett 2000). Hence, one of the plausible explanations for the observed SSR effect could be adsorption of U(VI) via a ternary surface complex formation. The effect of small amount of phosphate on U(VI) adsorption has been well documented, and was expected to result in lower adsorption at high SSR (Cheng et al., 2002; Cheng et al., 2004), contrary to the aqueous complexation effect. A Mehlich-1 phosphate extraction from OR soil indicated the presence of about 2.81E-4 mmol extractable phosphate in OR soil.

4.4 Summary and Conclusion

In this work, the scaling of adsorption capacity in batch and transport modes was explored in both synthetic adsorbent and natural geomedia. Here we have used a more homogeneous adsorbent as a control system to decipher the confounding processes that could influence adsorption in a highly heterogeneous system. In the case of IOCS, the adsorption capacity observed in the batch experiments was comparable with the adsorption capacity obtained from the column experiments. But in the case of a natural geomedia, a marked discrepancy between the batch and column adsorption capacity was observed. On analysis, the experiments at two differing solid-to-solution ratio resulted in differing adsorption isotherms in OR soil but not in the IOCS. Based on the trend in the adsorption of U(VI) with respect to SSR in OR soil, and the evolving body of literature in this research area, the plausible reason for the observed phenomena could be a solute that could influence U(VI) adsorption onto Fe oxides via forming a ternary surface complex (e.g. Phosphate).

4.5 References

Barnett, M.O., P.M. Jardine, S.C. Brooks, and H.M. Selim. 2000. Adsorption and transport of uranium(VI) in subsurface media. Soil Science Society of America Journal 64:908-917.

Barnett, M.O., P.M. Jardine, and S.C. Brooks. 2002. U(VI) adsorption to heterogeneous subsurface media: Application of a surface complexation model. Environmental Science & Technology 36:937-942.

Beck, M.A., L.W. Zelazny, W.L. Daniels, and G.L. Mullins. 2004. Using the Mehlich-1 extract to estimate soil phosphorus saturation for environmental risk assessment. Soil Science Society of America Journal 68:1762-1771.

Bostick, B. C., S. E. Fendorf, M. O. Barnett, P. M. Jardine and S. C. Brooks. 2002. Uranyl surface complexes formed on subsurface media from DOE facilities. Soil Science Society of America Journal 66: 99-108.

Cheng, T., M.O. Barnett, E.E. Roden, and J.L. Zhuang. 2004. Effects of phosphate on uranium(vi) adsorption to goethite-coated sand. Environmental Science & Technology 38:6059-6065.

Davis, J.A., D.E. Meece, M. Kohler, and G.P. Curtis. 2004. Approaches to surface complexation modeling of uranium (VI) adsorption on aquifer sediments. Geochimica et Cosmochimica Acta 68:3621-3641.

Gabriel, U., J.P. Gaudet, L. Spadini, and L. Charlet. 1998. Reactive transport of uranyl in a goethite column: An experimental and modelling study. Chemical Geology 151:107-128.

Gee, G. W. Oostrom, M., Freshley, M. D., Rockhold, M. L., Zachara, J. M. 2007. Hanford site vadose zone studies: An overview. Vadose zone journal. 6: 899-905.

Hsi, C.K.D., and D. Langmuir. 1985. Adsorption of uranyl onto ferric oxyhydroxides - application of the surface complexation site-binding model. Geochimica et Cosmochimica Acta 49:1931-1941.

Jang, J.H., B.A. Dempsey, and W.D. Burgos. 2007. A model-based evaluation of sorptive reactivities of hydrous ferric oxide and hematite for U(VI). Environmental Science & Technology 41:4305-4310.

Kohler, M., Curtis, G. P., Kent, D. B., Davis, J. A. 1996. Experimental investigation and modeling of uranium(VI) transport under variable chemical conditions. Water Resour. Res. 32: 3539-3551.

Loganathan VA, Barnett MO, Clement TP, Kanel SR., 2009. Scaling of Adsorption Reactions: U(VI) Experiments and Modeling. Applied Geochem. 24, 2051-2060.

Payne, T.E., J.A. Davis, and T.D. Waite. 1994. Uranium retention by weathered schists - the role of iron minerals. Radiochimica Acta 66-7:297-303.

Phillippi, J.M., V.A. Loganathan, M.J. McIndoe, M.O. Barnett, T.P. Clement, and E.E. Roden. 2007. Theoretical solid/solution ratio effects on adsorption and transport: Uranium(vi) and carbonate. Soil Science Society of America Journal 71:329-335.

Relyea, J.F., R.J. Serne., D. Rai. 1980. Methods for determining radionuclide retardation factors: Status report. Pacific Northwest National Laboratory.

Schwertmann,U., and Cornell,R.M., "Iron Oxides in the Laboratory.", pp. 67-92. Wiley-VCH, Weinheim, 2000.

Um, W., R.J.S., Christopher F. Brown, George V. Last. 2007. U(vi) adsorption on aquifer sediments at the hanford site. Journal of Contaminant Hydrology 93:255-269.

Waite, T.D., J.A. Davis, T.E. Payne, G.A. Waychunas, and N. Xu. 1994. Uranium(vi) adsorption to ferrihydrite - Application of a surface complexation model. Geochimica et Cosmochimica Acta 58:5465-5478.

5. An Assessment of U(VI) Removal from Groundwater using Biochar Produced from Hydrothermal Carbonization

5.1 Introduction

Uranium contamination in groundwater is a serious matter of concern to the U.S. Department of Energy (DOE) sites where it has been released to the environment or remains in storage (Davis et al., 2004). Moreover, ground water contamination caused by radionuclides, in particular uranium, is also a global environmental problem as countries increasingly move towards cleaner energy sources (Srivastava et al., 2010). Uranium, a radiotoxic element also possesses risk related to chemical toxicity. Among the various oxidation states of uranium, IV and VI oxidation states are the most important states in geological environments (Ervanne, 2003). The chemical toxicity of uranium is predominantly caused by the highly reactive hexavalent uranyl ions (Vandenhovea et al., 2006).

In the last few years, biosorption of radionuclides by different raw biomasses such as cork, rice and tea leaves, straw, coco shaving, coir pith, peat moss, etc. have been increasingly studied (Parab et al., 2005; Psarevaa et al., 2005). Numerous other materials such as zeolite (Camacho et al., 2010), hematite (Zeng et al., 2009), diatomite (Aytas et al., 1999), etc. have also been tested for the same purpose. Activated carbon, a form of high temperature biochar that has been treated with steam or CO_2 to maximize porosity, are the oldest and most widely used adsorbents (Mellah et al., 2006; Suhas and Carrott, 2007). However, this adsorbent is relatively expensive owing to its higher production cost associated with the activation process (Savovaa et al., 2001b).

Biochar, which is a byproduct of biorefineries, has attracted much attention recently due to its proven role in environmental management issues. In view of the government focus on renewable and alternative fuels, the biofuel industry of the US is on a tremendous growth path. . In fact, Renewable Fuel Standard (RFS) as part of Energy Independence and Security Act (EISA) of 2007 requires 36 billion gallon per year (BGY) of biofuels by 2022 (National Biofuels Action Plan, 2008). In this scenario, the abundantly available lignocellulosic biomasses are being considered as the major biomass feedstock. Moreover, the billion ton vision report concludes that the land resources of the US are capable of producing a sustainable supply of biomass (Perlack et al., 2005).

Biomass may be converted to fuels by many different thermochemical processes such as gasification, pyrolysis, hydrothermal liquefaction/carbonization (Kumar and Gupta, 2009). Biochar, a non-liquefied carbonaceous solid byproduct results from the thermochemical conversion processes. This carbonaceous material is being extensively studied for their application as a soil amendment (Laird et al., 2009). Historically, biochar has been used in soil to enhance plant growth. It also helps in improving soil water quality by increasing soil retention of nutrients and agrochemicals for plant and crop utilization. The leaching of nutrients from soil, which is one of the causes of ground water pollution, is retarded in the presence of biochar (Gaunt and Lehmann, 2008).

The yield of biochar (Table 5.1) mainly depends on the processing condition and type of biofuels being produced. The properties and composition of biochar change based on the production routes. For example, ash contents are higher in biochar produced from gasification/pyrolysis routes, whereas hydrothermally produced biochars are richer in carbonaceous materials. Through HTC, a carbon-rich black solid is obtained from biomass as an insoluble product in the temperature range of 180-350 ºC (Savovaa et al., 2001a; Titirici et al., 2007). Furthermore, during the process of biochemical conversion of biomass for bioethanol production, lignin-rich wet residues are generated which may be potentially converted to biochar. This is an environmentally friendly process because of its mere simplicity of using water as the sole reaction medium under pressure and heat, that leaves no further hazardous chemical waste or by product (Hu et al., 2008). It has attracted much attention due its versatility to utilize mixed biomass feedstock without any pretreatment or drying, at a comparatively low temperature (Kumar and Gupta, 2009).

Biochar produced from lignocellulosic biomass has potential to adsorb both organic pollutants and heavy metals. Studies have been reported on the use of biochar for removing metal contaminants such as lead, mercury, and arsenic from aqueous solution (Amuda et al., 2007; Budinova et al., 2006; Kalderis et al., 2008). Biochar derived from dairy manure was reported to sorb both heavy metals and organics (Cao et al., 2009). Biochar strongly adsorbs dissolved organic compounds from soil solution and makes them less bioavailable (Laird et al., 2009; Loganathan et al., 2009). In fact, pyrogenic organic matters (e.g. biochar, charcoal, soot and activated carbon) have been studied extensively for their high affinity and capacity for absorbing organic compounds (Smernik, 2009). As early as 1948, it was reported that the bioavailability of 2,4-chlorophenoxyacetic acid to sweet potatoes were decreased with the addition of activated carbon, presumably due to the strong sorption property of this biochar-like material. This very property of biochar is the reason why activated carbon has long been used to strip organic compounds from polluted air and water. Polycyclic aromatic hydrocarbons (PAH) have been reported to be sorbed strongly to biochar surfaces (Smernik, 2009).

Table 5.1 Biochar yield from thermochemical conversion processes of biomass

Process	Temperature and Time	Biochar Yield (%)
Gasification	750°C, ~ 10-20 s	10
Pyrolysis		
• Fast	500°C, ~ 1 s	12
• Moderate	500°C, ~ 10-20 s	20
• Slow	500°C, ~ 5-30 min.	35
• Flash Carbonization	> 400°C	40-45
Hydrothermal Carbonization	250-350°C, 10-60 min.	45-60

High molecular weight PAH shows high affinity for biochar (Dachs, 2000). The study showed that adsorption of aromatic contaminants to wood char was assisted by π-electron interactions and pore-filling mechanism (Chen and Chen, 2009). Moreover, nonpolar (naphthalene) and polar (nitrobenzene, *m*-dinitrobenzene, and 1-naphthol) aromatic compounds were used to understand the sorption mechanism of biochar produced at different pyrolytic temperatures (Chen and Chen, 2009; Chen et al., 2008). Biochar is porous with oxygen functional groups and aromatic surfaces. Because of its high surface-to-volume ratio and strong affinity to non-polar substances such as PAHs, dioxins, furans etc. biochar can be a potential sorbent for organic pollutants and pesticides, particularly planar aromatic compounds (Shrestha et al., 2010; Yu et al., 2009).

Though the scientific literature is replete with the use of biochar as an adsorbent for environmental pollutants, these studies deal with organic contaminants. Relatively fewer studies have reported on the use of biochar for removing metal contaminants such as lead, mercury, and arsenic from aqueous solution (Amuda et al., 2007; Budinova et al., 2006; Kalderis et al., 2008). Recently, Liu et al. (2010) have characterized the biochar produced via HTC (at 300ºC) and pyrolysis process (at 700ºC) and compared their adsorption capacity for copper ions. In this study, we hypothesize that hydrothermally produced biochar contain oxygen-rich functional groups on the surface and so are expected to show better affinity towards adsorption of dissolved U(VI). Considering that U(VI) is one of the major pollutants of concern in many U.S. Department of Energy sites, and the lack of literature on U(VI)-biochar interaction, a study of this nature is warranted to provide better alternative remediation technologies.

The major objective of this work was to assess the adsorption of uranium onto biochar produced from switchgrass, a major energy crop, by HTC. The physical and chemical characteristics of biochar were examined by X-ray diffraction (XRD), elemental analysis, Fourier transform infra-red spectroscopy (FTIR), and scanning electron microscopy (SEM) techniques. Our objective was to investigate the use of this environmentally friendly and benign sorbent for treating uranium contaminated groundwater. Batch adsorption studies were designed to assess the sorption potential of biochar for U(VI). The study examines the adsorption kinetics and equilibrium, and the effect of solid (biochar) loading and pH on U(VI) adsorption. In addition, the feasibility of biochar as a permeable reactive barrier medium was investigated using column experiments.

5.2 Experimental Section

Conversion of switchgrass (chopped to 5-10 mm length) to biochar was conducted in a high-pressure batch reactor in the presence of de-ionized water. The apparatus consisted of a 500 mL high-temperature, high- pressure metal reactor equipped with proportional-integral-differential controllers. Biomass and water (7:1) were charged into the reaction vessel and the reactor temperature was raised to 300° C with a heating rate of 7° C min^{-1}. After maintaining the temperature at 300° C for 30 minutes under autogeneous pressure conditions, the reactor was rapidly cooled to ambient conditions using water through a cooling coil. The product biochar was separated from the liquid after the reaction and further washed with deionized water. The resulting biochar was air dried and used for further characterization.

5.3 Product Characterization

Elemental analysis:

Both switch grass and biochar samples were dried in a forced-air oven at 60ºC. About 0.1-0.2 grams of each sample was weighed into tin foil cups and combusted with an oxygen catalyst at 1150º C. The total carbon was measured by the thermal conductivity method (Kirsten, 1979) using an Elementar Vario Macro CNS analyzer. For quantifying macro and micronutrients and metals, approximately 1.0 gram of dried sample was weighed into ceramic crucibles. The samples were then ashed for 8 hours in a muffle furnace at 500º C. This was followed by digestion on a hot plate using 1 N HNO_3 and 1 N HCl. Finally, the digested samples were filtered into 50 mL volumetric flasks and brought to volume with deionized water. All samples were analyzed using a Varian Vista-MPX Axial Spectrometer (Issac and Johnson, 1985). Analysis was set for 2 exposures (repetitions) per sample and the average results were reported.

SEM analysis:

The samples were held onto adhesive carbon tape on an aluminum stub followed by sputter coating with gold. Surface morphology of the sample was studied using an environmental scanning electron microscopy system (Zeiss EVO 50).

XRD analysis:

Rigaku Miniflex powder X-ray diffractometer equipped with a Cu $K\alpha_1$ radiation source at 30 kV voltages, 15 mA current and a miniflex goniometer was used for the XRD analysis. Diffraction patterns were collected in the 2θ range of 12-35° at a scan speed of 1° min^{-1} and step size of 0.05°.

FTIR analysis:

Infrared spectra (4000-400 cm^{-1}) were recorded using a Nicolet IR100 FTIR spectrometer that was equipped with a TGS/PE detector and a silicon beam splitter with 1

cm^{-1} resolution. The sample discs were prepared by mixing oven-dried (at 105°C) samples with spectroscopy-grade KBr in an agate mortar.

BET surface area measurement:

The method of Brunauer, Emmett, and Teller (BET) is commonly used to determine the total surface area of materials. The BET analysis was carried out using NOVA 2200e surface area and pore size analyzer (Quantachrome Instruments). Raw switchgrass and biochar samples were analyzed for multipoint BET surface area using nitrogen as the adsorbing gas at 77 K. The analysis involved outgassing the switch grass samples at 105°C for 3 hours and biochar samples at 75°C for 22 hours. In the case of biochar, the pore volume and pore radius was measured along with surface area. Selected samples were analyzed in duplicate and the results agreed within 5%.

5.4 Adsorption Studies

Batch adsorption kinetic experiments:

Batch kinetic experiments were performed at two different solid-to-solution ratios (SSR: 4 and 5 g L^{-1}) and initial U(VI) concentrations (ca. 30 and 10 mg L^{-1}) to estimate the equilibrium time for the adsorption reaction. The experiments were performed at the natural pH of biochar (ca. pH 3.9 ± 0.2) in 0.1 M $NaNO_3$. The experiments were carried out for 72 hours and samples were taken at regular intervals by sacrificing the tubes. U(VI) was measured using a kinetic phosphorescence analyzer (KPA, Chemchek Instruments, Inc.) after filtration of the samples through 0.45 μm polytetrafluoroethylene filter units and acidifying the samples to pH 1.0. The difference between the initial U(VI) concentration and aqueous U(VI) concentration was attributed to the adsorption of U(VI) onto biochar. Both the experiments had duplicate test tubes for each sampling interval, blanks [no U(VI)], and controls (no biochar).

Batch adsorption equilibrium experiment:

A batch isotherm experiment was performed at a solid loading of 5 g L^{-1} and at a pH of 3.9 ± 0.2. The initial concentration of U(VI) was varied between 5 to 30 mg L^{-1} and the experiment was conducted in a 0.1 M $NaNO_3$ background solution. Moreover, to study the effect of solid-to-solution ratio on adsorption, biochar was loaded at 1 g L^{-1} containing an initial U(VI) concentration of 10 mg L^{-1}. The test tubes were prepared in duplicates and tumbled for about 34 hours at 25°C, as 34 hours was found to be sufficient to attain equilibrium from the kinetic experiments. At the end of the equilibrium time, aqueous samples were filtered and acidified and analyzed as described above. Similar to the kinetic experiments, the difference between the initial U(VI) concentration and aqueous U(VI) concentration was attributed to the adsorption of U(VI) onto biochar. Further, the pH-dependent adsorption of U(VI) on to biochar was also studied by varying the pH (3-8).

Permeable reactive barrier (PRB) experiment:

Approximately 0.25 g of biochar was packed into a 1.0 cm × 10 cm glass column as an interlayer of about 0.8 cm depth between two quartz zones of 0.6 cm and 5.4 cm. The column was initially flushed with the background solution, 0.1 M $NaNO_3$, adjusted to pH 3.9 ± 0.2 at a flow rate of 4.1 mL $hour^{-1}$. After a few pore volumes of $NaNO_3$ flushing, U(VI), prepared in 0.1 M $NaNO_3$, and adjusted to pH 3.9 ± 0.2, at an initial concentration of ca. 3 mg L^{-1} was flushed through the column. Samples were collected at regular intervals and the pH was checked frequently. A stable pH of about 3.9 ± 0.2 was maintained in the effluent solution throughout the course of the experiment. At the end of the biochar site saturation, which was estimated based on the batch experiment results, the influent solution was changed back to U(VI)-free $NaNO_3$. A control for the permeable reactive barrier column was simultaneously run wherein the entire column was packed with pure white quartz with a particle size ranging between 0.210 and 0.297 mm, which was pre-washed with 0.1 M nitric acid. The experimental protocol for the control column was similar to the PRB column except for it was fully packed (6.8 cm) with pure quartz. In the case of the control column, a stable pH of 3.9 ± 0.2 was also maintained in the effluent solution throughout the course of the experiment. The residence time for the control column was calculated to be ca. 76.4 min whereas, in the case of PRB column, the residence for the PRB zone (0.8 cm) was ca. 8.99 min. At the end of the experiments selected samples were acidified and analyzed for U(VI) in KPA.

5.5 Results and Discussion

The oxygen content in raw switchgrass is typically 40-43 wt% (Berg and Visser, 2001), which was reduced to about 22-23 wt% in biochar. The elemental carbon in biochar was increased to 70.5 wt% compared to switchgrass that had 44.6 wt% (Table 5.2). Though the ash content did not change significantly, some of the inorganic compounds (e.g. K, Mg, P, and Na) decreased due to their solubilization in subcritical water. As result of carbonization process in subcritical water, more than 70 wt% of oxygen present in switchgrass could be removed and the product biochar became richer in carbon content. The formation of the carbon-rich solid through the carbonization of biomass in water medium is the consequence of dehydration, condensation, polymerization, and aromatization reactions (Funke and Ziegler, 2010). The biochar yield (dry weight basis) and higher heating value (measured in a IKA-C200 Calorimeter) of biochar produced from switchgrass was 42.9 wt% and 28.7 MJ/kg on an oven-dry basis. Three separate experiments were conducted to produce biochar under the same process condition at 300°C for confirming the reproducibility of the process. The relative standard deviation of biochar yield and its heating value were 3.3% and 1.1%, respectively. The effect of temperature, pressure, and residence time on the yield and the oxygen-to-carbon ratio (O/C) of biochar has been studied separately (Kumar, 2010). The study showed that reaction temperature has more influence on the carbonization process compared to the effect of reaction time and pressure. With an increase in temperature, the mass yield of biochar decreased, but the heating value increased.

Table 5.2 Composition of switchgrass and biochar

Elements	C	Ash	Ca	K	Mg	P	Fe
	(wt%)		(ppm)				
Switchgrass	44.6	4.5	2105	4082	4514	941	115
Biochar	70.5	3.7	2029	665	2215	481	258

Typically, at higher temperatures dehydration reactions start dominating though water is present in excess in the reactor resulting in lower O/C ratios of the biochar (Patrick et al., 2001). The O/C ratio of switchgrass is about 0.9, which decreased to 0.37 for the biochar produced at 300 °C in subcritical water. The SEM images for switchgrass and biochar are shown in the Figure 5.1. These images indicated that biochar has different macromolecular structure than raw switchgrass, and the average particle sizes became smaller after treatment. Further, the images show that biochar has an irregular surface and porous structure compared to raw switchgrass. These results are reflected in the higher surface area of biochar when compared to raw switch grass. The specific surface area of switchgrass and biochar were 1.0 and 2.9 m^2 g^{-1}, respectively. It has been reported that char surface area greatly depended on treatment temperature (Liu et al., 2010). Due to the high temperature and long residence time of the reaction conditions, the porous structure of biochar was cracked and the pores were partially blocked as a result of the repolymerization/recondensation of water soluble compounds. This could have resulted in the lesser increase in surface area for biochar. The total pore volume of the biochar was found to 7.2E-3 cm^3 g^{-1} with an average pore radius of 50.02 Å, indicating that it is rich in micropores. The cross-linked structure, which was made up of cellulose, hemicellulose, and lignin in switchgrass, was broken through fragmentation, decarboxylation, and dehydration reaction in subcritical water. Here, water acts as both a reactant and the reaction medium. Water as a reactant leads to hydrolysis reactions and rapidly degrades the polymeric structure of biomass. With the removal of polymeric components during the reactions, additional pores and terrains were created.

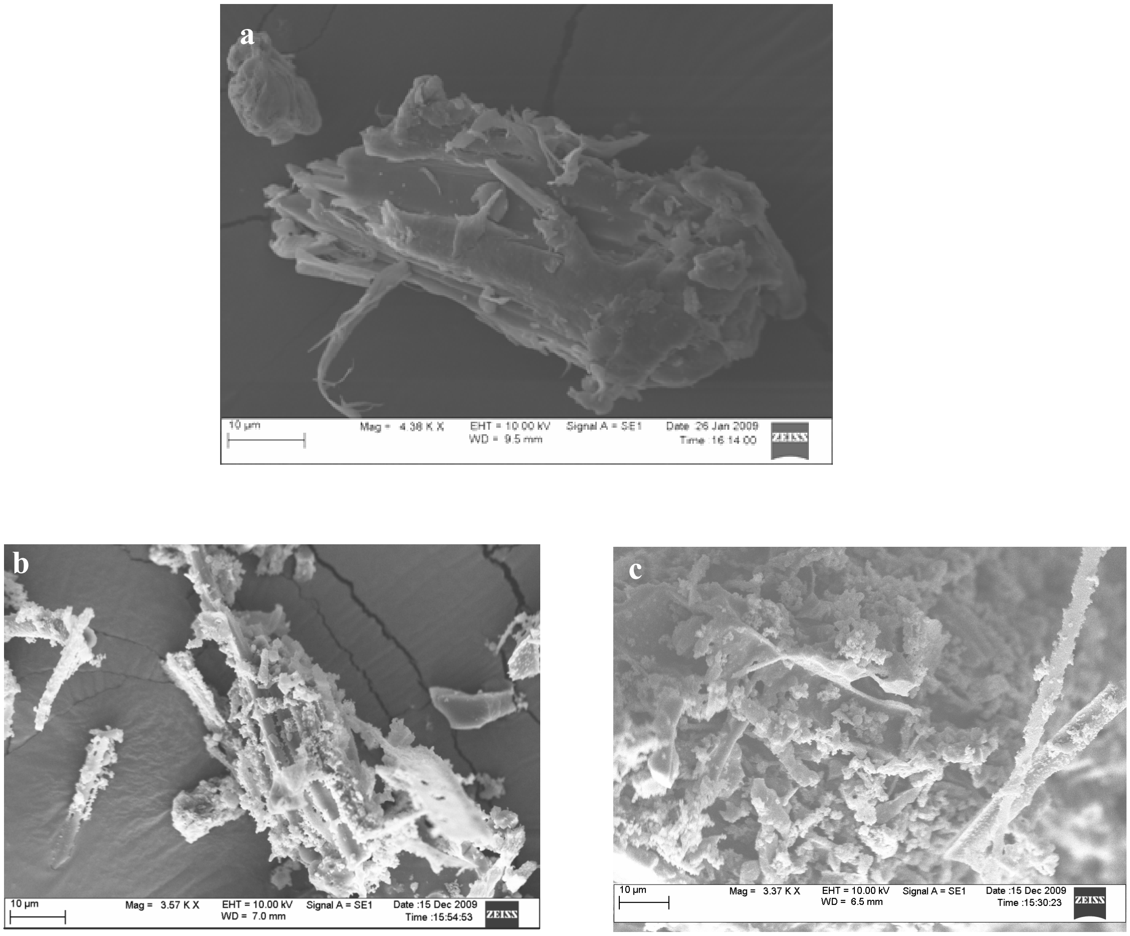

Figure 5.1 SEM image of switchgrass (a), biochar (b, and c).

The XRD patterns for switchgrass and biochar are shown in Figure 5.2. The distinct sharp crystalline cellulosic peak [2θ = 22.7°] that comes from the crystal structure of cellulose (Segal et al., 1959) was displayed in the switchgrass, whereas this peak was absent in the biochar. The absence of any crystalline peak of cellulose in the biochar XRD pattern confirms that it contained mainly the amorphous components as a result of decomposition of cellulose.

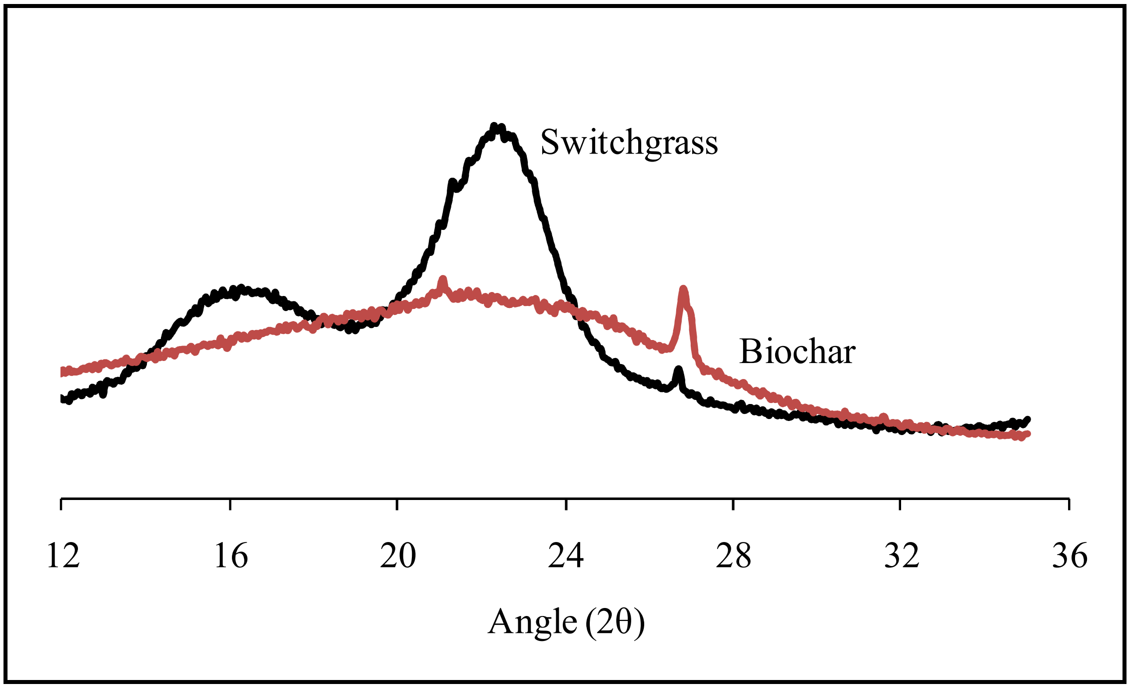

Figure 5.2 XRD patterns of switchgrass and biochar.

The biochar was characterized by FTIR in the near IR region (wave number: 4000–400 cm^{-1}). A typical FTIR spectrum of biochar is shown in Figure 5.3. Various band assignments in the FTIR spectrum for the samples are listed in Table 5.3. The change in absorbance peaks mainly appeared in the range of 1800 - 800 cm^{-1}. The FTIR spectrum of biochar was similar to that of switchgrass with respect to the peaks of lignin. The ether linkages present in switchgrass around 1200 cm^{-1} and 1000 cm^{-1} between the cellulose skeleton units were hydrolyzed. As seen in the spectra, most of the lignin fractions were retained in the biochar. The results were confirmed by the lignin peaks at 1270, 1424 and 1510 cm^{-1} in the FTIR. In addition, at 1613 and 1701 cm^{-1}, the peaks of polymeric product were also seen in the spectra. The results indicate that biochar is composed mainly of aromatic cores derived from the lignin fraction and polymeric product that was produced in the hydrothermal carbonization process. The peak at 893

cm^{-1} is characteristic of β-anomers or β-linked glucose polymers and the peak at 1053 cm^{-1} is C–O stretching. These peaks are present in the switchgrass but are absent in biochar. Further, the absence of a peak around 1635 cm^{-1} indicated that the moisture retention capability of biochar has drastically reduced (Baeza and Freer, 2001; Cheng et al., 2009; Kobayashi et al., 2009). The presence of several oxygen functional groups (carboxylic, hydroxyl/phenolic, carbonyl) in biochar are confirmed from the FTIR spectra.

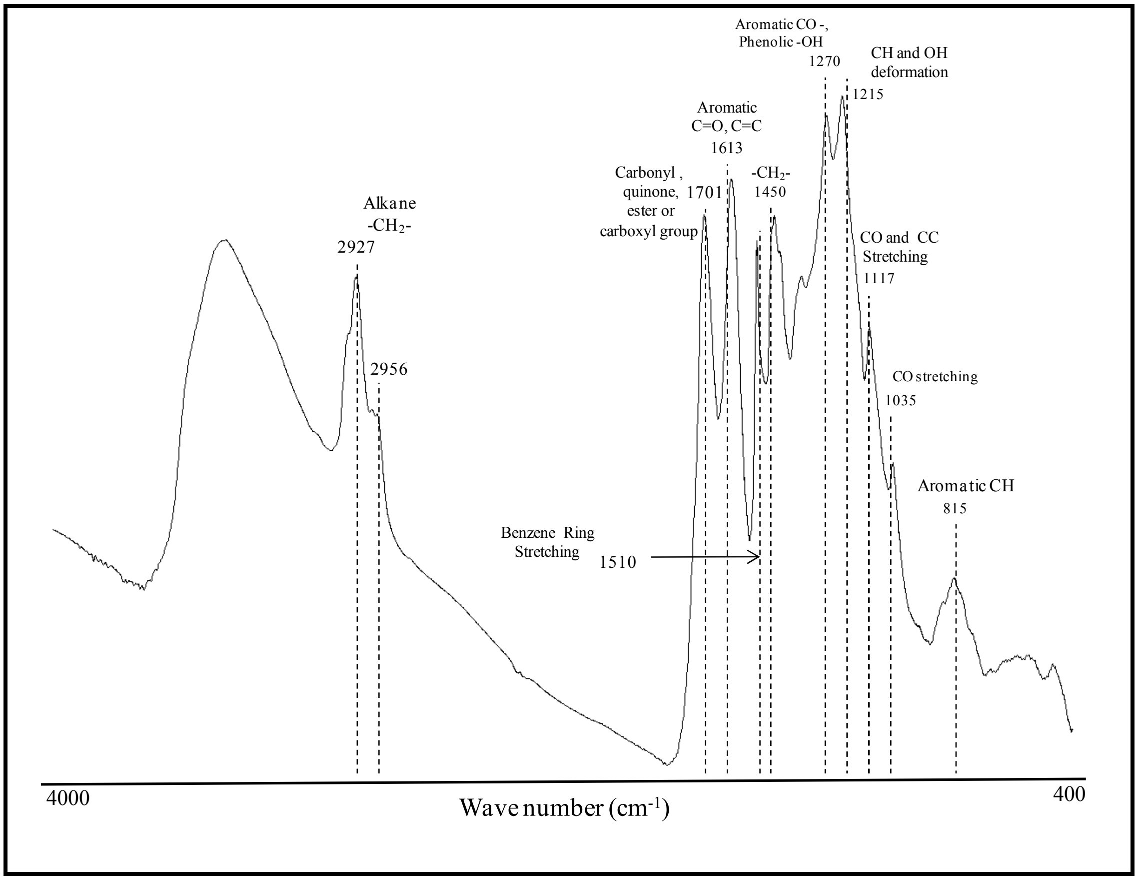

Figure 5.3 FTIR spectrum of biochar.

As observed in the FTIR analysis, the presence of oxygen-rich organic compounds on the biochar surfaces adds substantial cation exchange capacity. For example, the biochar-amended soil has been reported to have 5-20% higher cation exchange capacity during a 500-day soil column leaching/incubation study conducted by Laird et. al (2009).

Table 5.3 Band assignments in FTIR spectrum of biochar sample

Wave number (cm^{-1})	Band assignments	Reference
2927, 2867	- CH_2- Alkane	Chen and Chen, 2009
1701	Carbonyl , quinone, ester or carboxyl group	Liu et al., 2010; Sevilla and Fuertes, 2009
1613	C=O, C=C Aromatic intense because of the presence of oxygen containing polar substituents	Chen and Chen, 2009; Varhegyi et al., 1998
1510	Benzene ring stretching, C=C ring stretching vibration of lignin	Chen et al., 2008
1450	- CH_2-	Chen et al., 2008
1270	Aromatic CO- and phenolic –OH stretching	Chen et al., 2008
1215	CH and OH deformation	
1117	CO and CC Stretching and CH_2 rocking	Baeza and Freer, 2001
1035	CO stretching	Baeza and Freer, 2001
815	Aromatic CH out of plane deformation	Chen et al., 2008
3000-3700	Presence of oxygen group	Sevilla and Fuertes, 2009

Carboxylic groups present and also formed over time on the surface of biochar increases its nutrient holding capacity and also reduces the leaching of pollutants such as dissolved phosphates and nitrates into groundwater. The nanoporous structure of biochar with available oxygen functional groups on the surface provides an excellent opportunity to adsorb heavy metal ions from the aqueous solution (Hu et al., 2008; Sevilla and Fuertes, 2009; Tan et al., 1993). Typically, hydrothermally produced biochar has relatively more O/C and hydrogen-to-carbon (H/C) ratio and undergoes lesser carbonization processes compared to the biochar produced via pyrolysis process.

Biochar produced at higher temperature showed high pH, cation exchange capacity and surface area (Lehmann, 2007). On the contrary, biochar produced at low temperature showed availability of more actives sites and the existence of stable carbon-oxygen complexes. In a recent study on the HTC of model compound cellulose (a major component of lignocellulosic biomass), Sevilla and Fuertes (2009) showed that biochar consists of a high amount of oxygen (22-23 wt%) that is present in the core and in the shell of carbonaceous particles. Their analysis concluded that oxygen in the inner part probably consists of less reactive groups (i.e. ether, quinone, pyrone), whereas the shell contains more reactive/hydrophilic groups (i.e. hydroxyl, carbonyl, carboxylic, ester).

Raw biomass such as peat, poplar sawdust, and coconut shells have also been reported to show affinity towards metal ions particularly at low ion concentrations (McKay, 1997; Sciban et al., 2007). However, the use of raw biomass as adsorbents are associated with the risk of leaching of the organic pollutants due to the presence of extractable compounds. As supported by TG analysis (Kumar, 2010), biochar, which is more thermally stable as an adsorbent, will avoid such risks.

Batch adsorption results

The kinetic experiments indicated about 90% of initial U(VI) adsorption resulting within 8 hour, at both solid-to-solution ratios (Figure 5.4). A similar fast adsorption reaction was reported for Pb (II) sorption onto biochar produced via HTC (Liua and Zhang, 2009). Based on the reaction kinetics, about 34 hours of equilibrium time was chosen for the batch isotherm experiments.

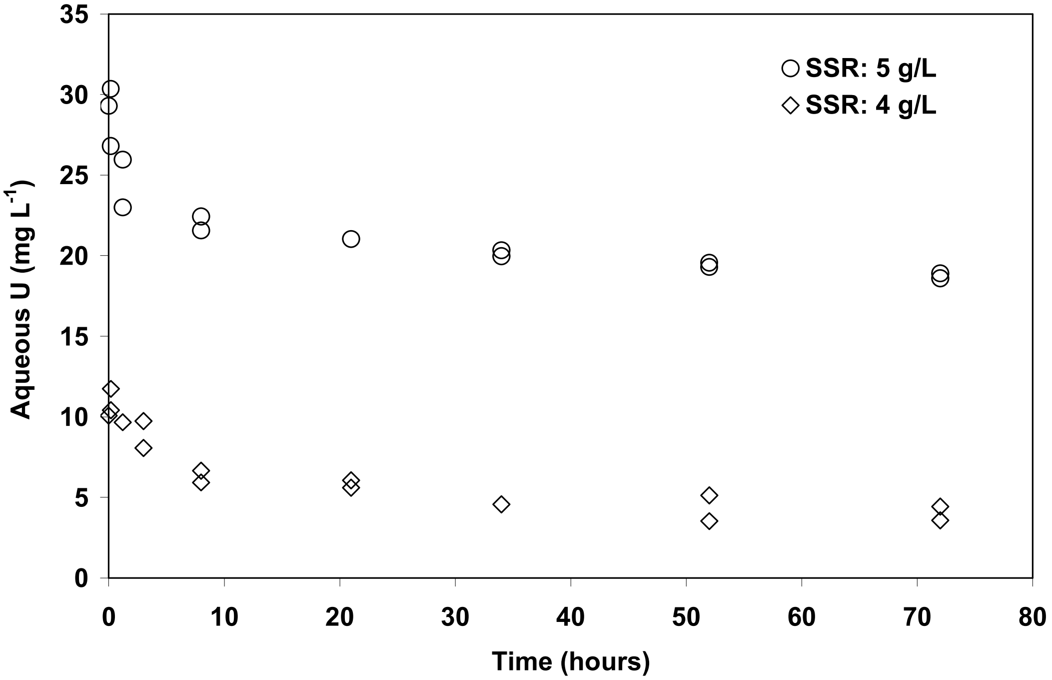

Figure 5.4 Kinetics of U(VI) adsorption onto biochar at initial U(VI) concentrations. SSR: 5 or 4 grams of biochar per litre, pH: 3.9 ± 0.2, and I: 0.1 M $NaNO_3$.

The batch adsorption isotherm is shown in Figure 5.5a. The adsorption of U(VI) on to biochar followed an H-type isotherm (Limousin et al., 2007). A complete adsorption of 10 mg L^{-1} of initial U(VI) by 0.1 g of biochar was observed, beyond which the adsorption plateaus sharply. The shape of the isotherm indicates that this could have

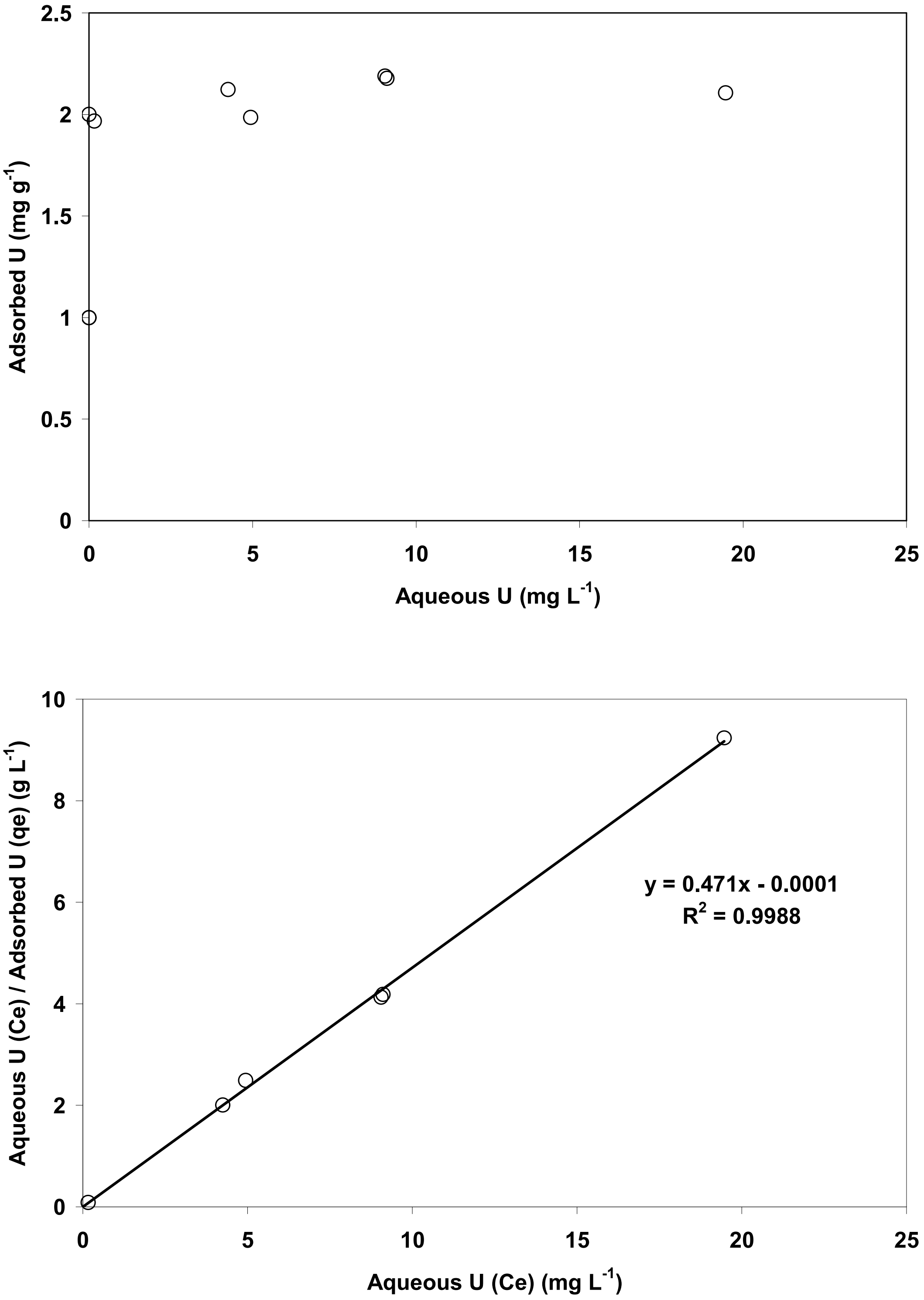

Figure 5.5 (a) Adsorption isotherm of U(VI) onto biochar. SSR: 5 g L^{-1} pH: 3.9 ± 0.2; I: 0.1 M $NaNO_3$. (b) Isotherm data fitted using Langmuir model.

been due to the binding of uranyl cation onto biochar sites/pores. Once the adsorption sites get completely filled, the biochar ceases to adsorb more uranium resulting in a plateau. The adsorption data was fitted using a Langmuir isotherm model (Figure 5.5b) and the sorption capacity of biochar was estimated to be ca. 2.12 mg U g^1 of biomass (0.2% w/w). Moreover, a similar distribution coefficient [K_d, where $K_d = q/c$; q (mg g^{-1}) is the equilibrium adsorbed-phase concentration and c (mg L^{-1}) is the equilibrium aqueous-phase concentration] was observed over a range of solid loading indicating a constant amount of adsorption sites in biochar structure (Figure 5.6). At the end of the batch sorption experiment, biochar was recovered, dried, and tested for crystalline peaks under x-ray diffraction. Lack of sharp peaks in the diffraction spectra suggested an adsorption phenomena rather than U(VI) precipitation (figure not shown). When compared to the studies reported on other heavy metals (Cu(II), Pb(II)), U(VI), the adsorption onto biochar showed similar adsorption potential (Liu and Zhang, 2009; Liu et al., 2010).

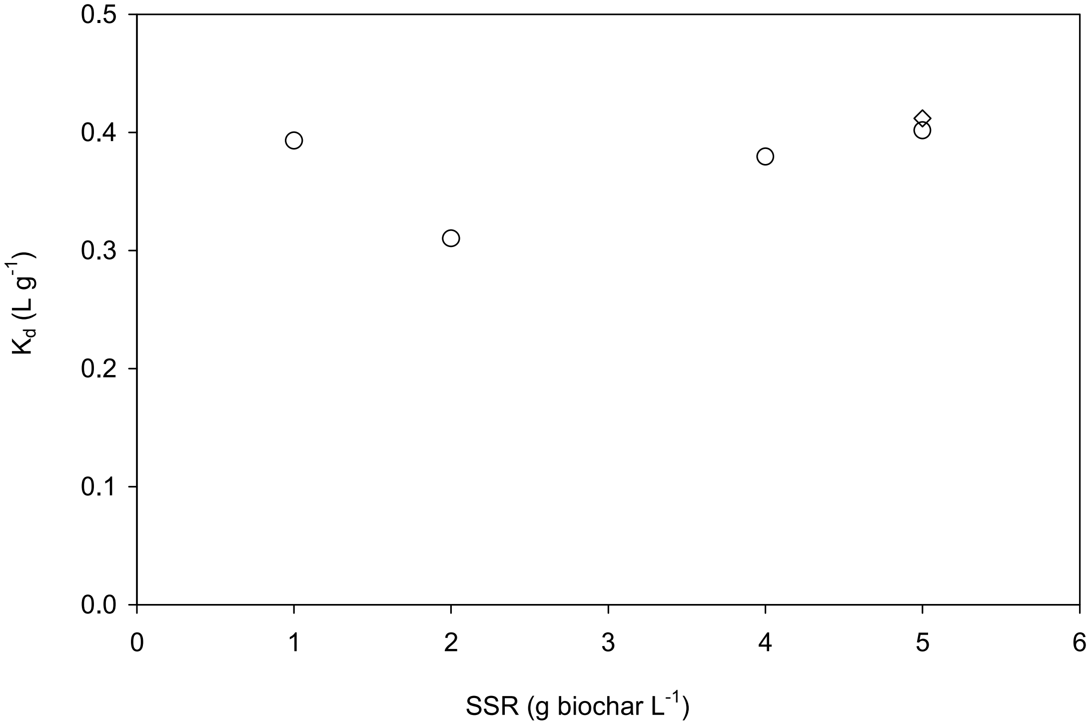

Figure 5.6 Adsorption of U(VI) onto biochar at different SSR. pH: 3.9 ± 0.2; ionic strength: 0.1 M $NaNO_3$. (◊) indicate the distribution coefficient of independently obtained new batch of biochar.

The adsorption of uranium was highly dependent on the solution pH. The pH edge (Figure 5.7) indicated that a unit increase in pH from 3.9 (natural pH of biochar) to 4.8 would result in ~100% more U(VI) adsorption. Hence, a maximum adsorption of about 90% of U(VI) occurred at about pH 5.9. Increasing the pH beyond 6.2 resulted in decreasing adsorption. These results indicate that adsorption of U(VI) on to biochar was highly dependent on U(VI) speciation.

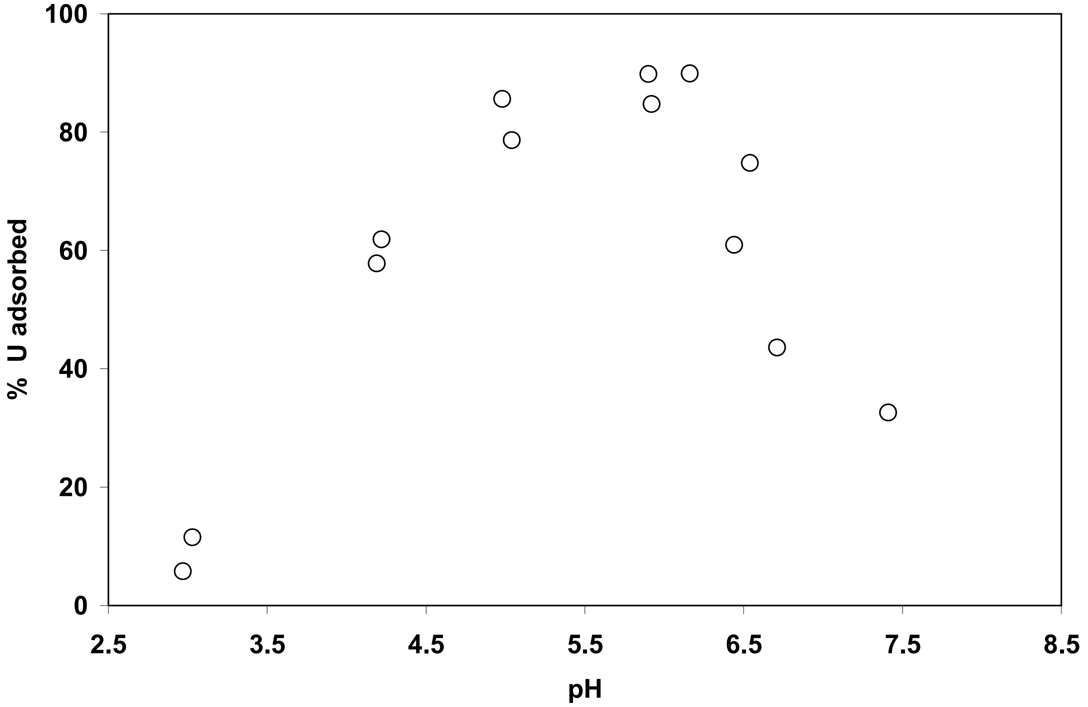

Figure 5.7 Adsorption of U(VI) on to biochar with respect to pH. Initial concentration of U(VI): 30 mg L^{-1}. Ionic strength: 0.1 M NaNO$_3$.

The speciation of uranium with respect to pH at 20 mg L^{-1} in 0.1 M NaNO$_3$ system was calculated using Visual MINTEQ 3.0 (Figure 5.8). At low pH, the biochar surface was expected to be protonated and hence positively charged (< pH 3.5). Hence, adsorption of UO_2^{2+} ions was less preferred at low pH. An increase in pH resulted in a less positive biochar surface that adsorbed the cationic uranium species [$(UO_2)_2(OH)_2^{2+}$, UO_2OH^+, $(UO_2)_3(OH)_5^+$]. Around the circumneutral pH, U(VI) speciation was dominated by anionic uranyl carbonate [$(UO_2)_2CO_3(OH)^{3-}$, $UO_2(CO_3)_3^{4-}$, $UO_2(CO_3)_2^{2-}$] and hence adsorption on to biochar decreased beyond pH 6.2. These results indicate that by adjusting the solution pH, the adsorption efficiency of biochar could be optimized.

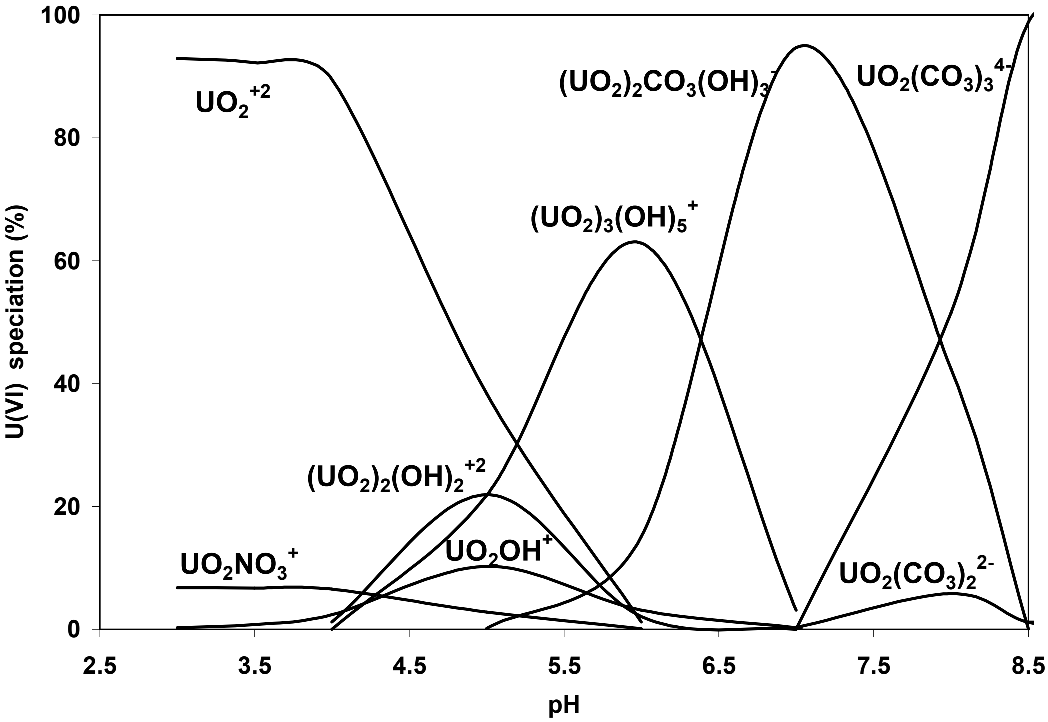

Figure 5.8 Aqueous speciation of U(VI) with respect to pH at a total U(VI) concentration of 20 mg L^{-1}; I: 0.1 M $NaNO_3$; pCO_2: $10^{-3.5}$ atm.

Column adsorption results

The permeable reactive barrier setup and the corresponding results from the experiments are shown in Figures 5.9a and b. The U(VI) breakthrough from the PRB column (Figure 5.10a) indicated a biochar adsorption capacity of 0.52 mg U g^{-1} of biochar. When compared to the adsorption of U(VI) onto quartz at similar conditions (Figure 5.10b), U(VI) adsorbed to biochar was 473 times more, on a per gram basis. Though the U(VI) adsorption capacity for biochar observed in the PRB column was about four times less than what was observed in the batch adsorption experiment, it was still significantly higher than pure quartz.

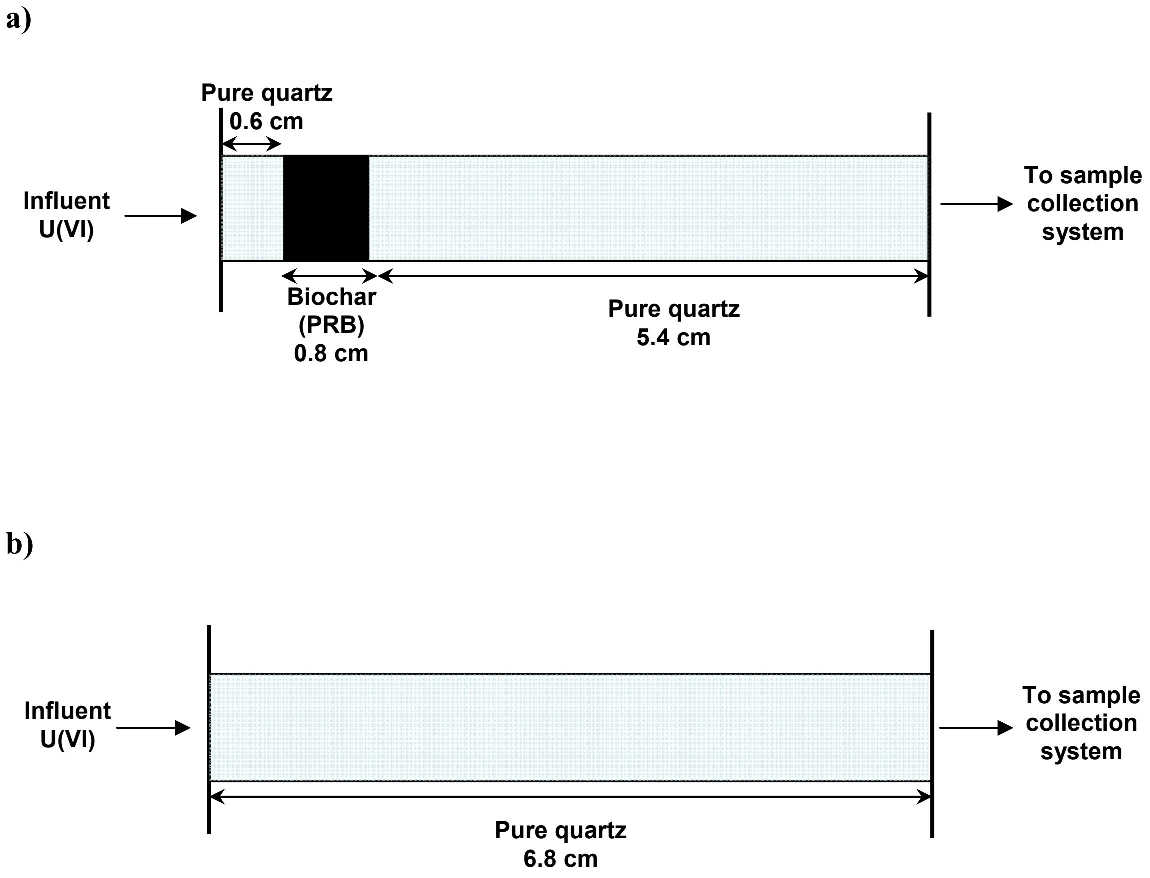

Figure 5.9 (a) Schematic of the column filled with biochar as a permeable reactive barrier (PRB) medium. (b) Schematic of a column filled with pure quartz that was used as a control for permeable reactive barrier experiment.

Moreover, the low U(VI) adsorption onto biochar in the column setting (relative to the results expected from the batch experiments) could be due to preferential flow scenarios in the column resulting in lesser surface reactive surface when compared to batch conditions. Furthermore, in the PRB column, the adsorbent material, biochar, was packed to a depth of about 0.80 cm which is similar to the thickness of the column itself 1.0 cm. Hence, a relatively lesser U(VI) adsorption to biochar was expected in the column setting when compared to the batch setting due to considerable loss of reactive surface to the glass column surface. However, the experimental conditions for U(VI) adsorption can be optimized for maximum U(VI) removal, by increasing the pH (Figure 5.7).

Liua and Zhang (2009) reported a similar trend in adsorption for Pb(II) and Cu(II) binding onto the biochar produced via hydrothermal treatment. They showed that the adsorption was a physical endothermic process where irregular oxygen-containing surfaces proved to be beneficial. They further compared the adsorption properties of biochar produced via the hydrothermal carbonization and pyrolysis process. For the case of copper removal from wastewater, it was concluded that the biochar produced from HTC showed better adsorption properties (4.46 mg g^{-1}) than that from pyrolysis (2.75 mg g^{-1}) (Liu et al., 2010). Contrary to the hydrothermal process, pyrolysis resulted in much less oxygen-containing groups on the biochar surface due to deeper carbonization of biomass. The sorption properties of these materials are due to the presence of functional groups such as carboxyl, carbonyl, and hydroxyl, which have a high affinity for metal ions.

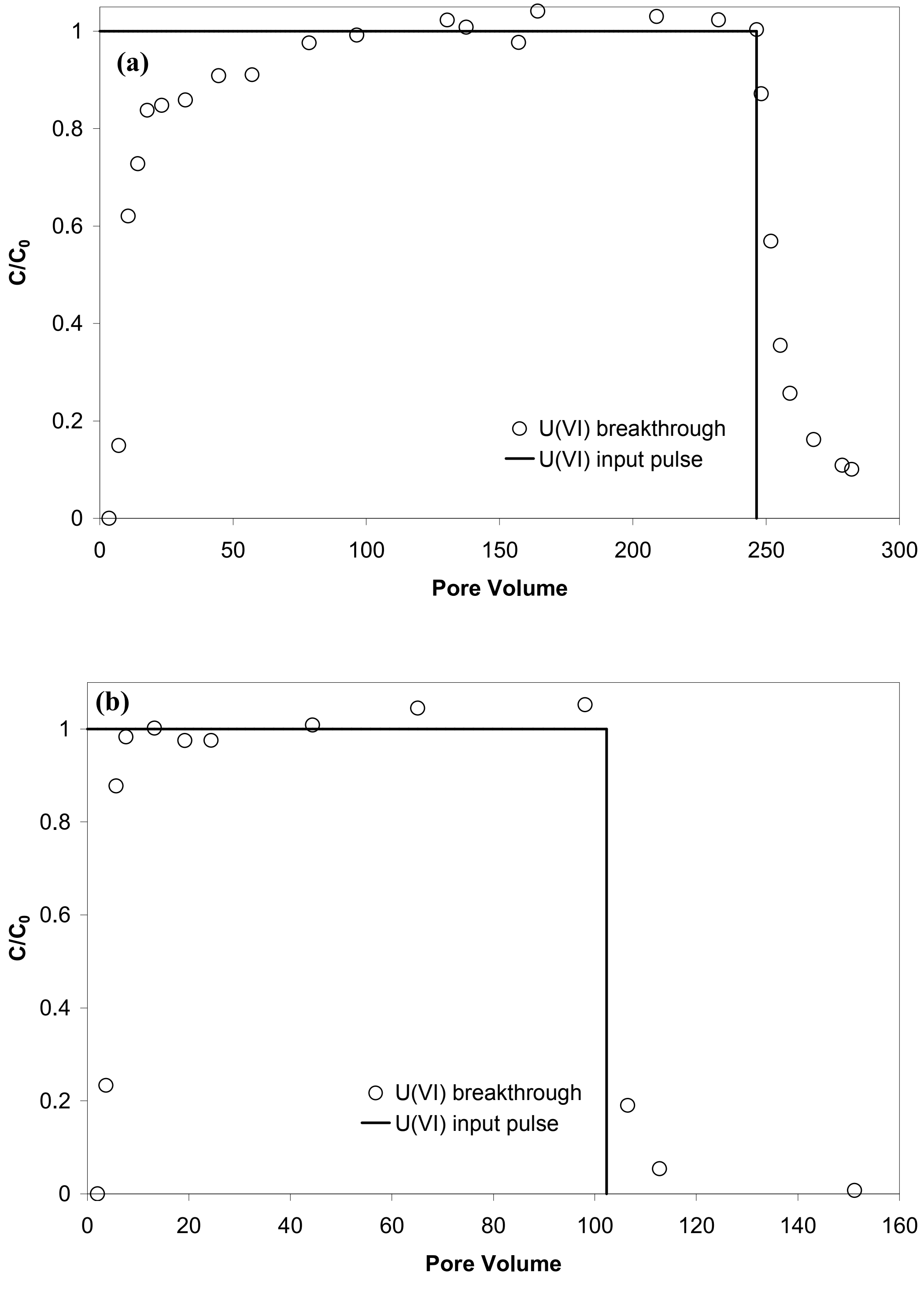

Figure 5.10 (a) U(VI) breakthrough profile in a column wherein biochar was used as a PRB medium. C_0: 3 mg L^{-1}; pH: 3.9 ± 0.2; I: 0.1 M $NaNO_3$. (b) Breakthrough profile in a column filled with pure quartz, serves as a control for PRB column.

A recent review shows the importance of adsorbent materials (activated carbon, ionic exchange resins, zero-valent iron, etc.) as a permeable reactive barrier (PRB) to treat U(VI)-contaminated groundwater (Maria et al., 2009). The results show that biochar could be considered as a potentially competitive low cost and efficient PRB medium for U(VI), which also provides the opportunity for long-term storage of carbon in soil (Shrestha et al., 2010). Besides being free of toxic or carcinogenic compounds, the carbonaceous material is also water-wettable. In view of the growing biofuels industry, it is important to add value to the byproduct, biochar, collected at the end of bioenergy cycle. If not utilized properly, biochar can be an atmospheric pollutant (Shrestha et al., 2010). The effective use of biochar for contaminant remediation would also enhance the goal of the green processes. Considering the cost factor, biochar produced via the HTC process is relatively less energy intensive and can be viewed as a potential low cost process for obtaining efficient adsorbents. Moreover, when compared to other PRB medium, for example zero valent iron, biochar is expected to be more stable under changing redox conditions. When compared to bone char or apatite which sequesters U(VI) by forming stable uranyl precipitates, biochar entraps U(VI) by sorption mechanism even at low pH as encountered in many U(VI) contaminated sites (Bostick et al., 2002). These properties of support its utility as a highly beneficial contaminant remediation strategy.

5.6 Summary and Conclusion

This study indicates that hydrothermally produced biochar is a porous and amorphous solid rich in active functional groups (hydroxyl/phenolic, carboxylic, and carbonyl groups). The adsorption of uranium onto biochar is also an attractive alternative to treat U(VI)-contaminated groundwater. The kinetics of the sorption process was fast and the extent of adsorption resembles a H-type isotherm. Moreover, the adsorption capacity is highly dependent on the system pH. A column experiment supported the use of biochar as a permeable reactive barrier medium. Compared to other remediation strategies, the feasibility of biochar as U(VI) adsorbent is supported by its environmentally benign nature. The major advantage of biochar is that it could serve as an effective and green adsorbent for U(VI) without causing environmental damages.

5.7 References

Amuda, O.S., A.A. Giwa, and I.A. Bello. 2007. Removal of heavy metal from industrial wastewater using modified activated coconut shell carbon. Biochem. Eng. J. 36:174-181.

Aytas, S., S. Akyil, M.A.A. Aslani, and U. Aytekin. 1999. Removal of uranium from aqueous solutions by diatomite. J. Radioanal. Nucl. Ch. 240:973-976.

Baeza, J., and J. Freer. 2001. Chemical characterization of wood and its components, p. 275-384, *In* D. N.-S. Hon and N. Shiraishi, eds. Wood and cellulosic chemistry, second ed. Marcel Dekker, Inc., New York. Basel.

Berg, D.V.D., and P.D. Visser. Final Report FAIR 5-CT97-3701. 2001 “Switchgrass”. BTG (Biomass Technology Group), Enschede, The Netherlands. Chapter 7, pp 48-50.

Bostick, B.C., S. Fendorf, M.O. Barnett, P.M. Jardine, and S.C. Brooks. 2002. Uranyl surface complexes formed on subsurface media from DOE facilities. Soil Sci. Soc. Am. J. 66:99-108.

Budinova, T., E. Ekinci, F. Yardim, A. Grimm, E. Bjornbom, V. Minkova, and M. Goranova. 2006. Characterization and application of activated carbon produced by H3PO4 and water vapor activation. Fuel Process. Technol. 87:899–905.

Camacho, L.M., S. Deng, and R.R. Parra. 2010. Uranium removal from groundwater by natural clinoptilolite zeolite: Effects of pH and initial feed concentration. J Hazard. Mater. 175:393-398.

Cao, X., L. Ma, B. Gao, and W. Harri. 2009. Dairy-Manure Derived Biochar Effectively Sorbs Lead and Atrazine. Environ. Sci. Technol. 43:3285-3291.

Chen, B., and Z. Chen. 2009. Sorption of naphthalene and 1-naphthol by biochars of orange peels with different pyrolytic temperatures. Chemosphere 76:127-133.

Chen, B., D. Zhou, and L. Zhu. 2008. Transitional adsorption and partition of nonpolar and polar aromatic contaminants by biochars of pine needles with different pyrolytic temperatures. Environ. Sci. Technol. 42:5137-5143.

Cheng, L., X.P. Ye, R. He, and S. Liu. 2009. Investigation of rapid conversion of switchgrass in subcritical water. Fuel Process. Technol. 90:301-311.

Dachs, J. 2000. Adsorption onto aerosol soot carbon dominates gas-particle partitioning of polycyclic aromatic hydrocarbons. Environ. Sci. Technol. 34:3690.

Davis, J.A., D.E. Meece, M. Kohler, and G.P. Curtis. 2004. Approaches to surface complexation modeling of Uranium(VI) adsorption on aquifer sediments. Geochim. Cosmochim. Ac. 68:3621-3641.

Ervanne, H. 2003. Interferences in uranium oxidation states during dissolution of solid phases J. Radioanal. Nucl. Ch. 256:497-500.

Funke, A., and F. Ziegler. 2010. Hydrothermal carbonization of biomass: A summary and discussion of chemical mechanisms for process engineering. Biofuel. Bioprod. Bior. 4:160-177.

Gaunt, J.L., and J. Lehmann. 2008. Energy balance and emissions associated with biochar sequestration and pyrolysis bioenergy production. Environ. Sci. Technol. 42:4152-4158.

http://www.biochar-international.org/biochar [Online] (verified February, 2010).

Hu, B., S.-H. Yu, K. Wang, L. Liu, and X.-W. Xu. 2008. Functional carbonaceous materials from hydrothermal carbonization of biomass: an effective chemical process. Dalton T. 40: 5414-5423.

Isaac, R.A. and W.C. Johnson, 1985, Elemental Analysis of Plant Tissue by Plasma Emission Spectroscopy: Collaborative Study. J. Assoc. Off. Anal. Chem. 68(3), 499- 505.

Kalderis, D., D. Koutoulakis, P. Paraskeva, E. Diamadopoulos, E. Otal, J.O. Valle d., and C. Fernandez-Pereira. 2008. Adsorption of polluting substances on activated carbons prepared from rice husk and sugarcane bagasse. Chem. Eng. J. 144.

Kirsten,W.J.,1979.Automated Methods for the determination of carbon,hydrogen, nitrogen,and sulfur,and sulfur alone in organic and inorganic materials. Anal.Chem.51:1173-1179.

Kobayashi, N., N. Okada, A. Hirakawa, T. Sato, J.Kobayashi, S. Hatano, Y. Itaya, and S. Mori. 2009. Characteristics of solid residues obtained from hot-compressed-water treatment of woody biomass. Ind. Eng. Chem. Res. 48:373-379.

Kumar,S, 2010. Dissertation on "Hydrothermal Treatment for Biofuels: Lignocellulosic Biomass to Bioethanol, Biocrude, and Biochar". Department of Chemical Engineering, Auburn University, Auburn, AL, USA.

Kumar, S., and R.B. Gupta. 2009. Biocrude Production from Switchgrass using Subcritical Water. Energ. Fuels 23:5151-5159.

Laird, D.A., R.C. Brown, J.E. Amonette, and J. Lehmann. 2009. Review of the pyrolysis platform for coproducing bio-oil and biochar. Biofuel. Bioprod. Bior. 3:547-562.

Lehmann, J. 2007. Bio-energy in the black. Front. Ecol. Environ. 5:381-387.

Limousin, G., J.P. Gaudet, L. Charlet, S. Szenknect, V. Barthes, and M. Krimissa. 2007. Sorption isotherms: A review on physical bases, modeling and measurement. Appl. Geochem. 22:249-275.

Liu, Z., and F.-S. Zhang. 2009. Removal of lead from water using biochars prepared from hydrothermal liquefaction of biomass. J. Hazard. Mater. 167:933-939.

Liu, Z., F.-S. Zhang, and J. Wu. 2010. Characterization and application of chars produced from pinewood pyrolysis and hydrothermal treatment. Fuel 89:510-514.

Liua, Z., and F.-S. Zhang. 2009. Removal of lead from water using biochars prepared from hydrothermal liquefaction of biomass. J. Hazard. Mater. 167:933-939.

Loganathan, V.A., Y.C. Feng, G.D. Sheng, and T.P. Clement. 2009. Crop-Residue-Derived Char Influences Sorption, Desorption and Bioavailability of Atrazine in Soils. Soil. Soc. Am. J. 73:967-974.

Maria, G., P.L. Vasile, and C. Igor. 2009. Characterization and remediation of soils contaminated with uranium. J. Hazard. Mater. 163:475-510.

McKay, J.F.P.G. 1997. Equilibrium parameters for the sorption of copper, cadmium and zinc ions onto peat. J. Chem. Technol. Biotechnol. 69:309-320.

Mellah, A., S. Chegrouche, and M. Barkat. 2006. The removal of uranium(VI) from aqueous solutions onto activated carbon: Kinetic and thermodynamic investigations. J. Colloid Interf. Sci. 296:434-441.

National Biofuels Action Plan, October 2008.
http://www1.eere.energy.gov/biomass/pdfs/nbap.pdf

Parab, H., S. Joshi, N. Shenoy, R. Verma, A. Lali, and M. Sudersanan. 2005. Uranium removal from aqueous solution by coir pith: equilibrium and kinetic studies. Bioresour. Technol. 96:1241-1248.

Patrick, H.R., K. Griffith, C.L. Liotta, and C.A. Eckert. 2001. Near critical water: A benign medium for catalytic reactions. Ind. Eng. Chem. Res. 40:6063-6067.

Perlack, R.D., L.L. Wright, A.F. Turhollow, R.L. Graham, B.J. Strokes, and D.C. Erbach. 2005. Biomass as a feedstock for a bioenergy and bioproducts industry: The technical feasibility of a billion-ton annual supply. A Joint report sponsored by U.S. Department of Energy and U.S. Department of Agriculture:78.

Psarevaa, T.S., O.I. Zakutevskyya, N.I. Chubara, V.V. Strelkoa, T.O. Shaposhnikovaa, J.R. Carvalhob, and M.J.N. Correia. 2005. Uranium sorption on cork biomass. Colloid Surface A. 252:231-236.

Savovaa, D., E. Apakb, E. Ekincib, F. Yardimb, N. Petrova, and T. Budinovaa. 2001a. Biomass conversion to carbon adsorbents and gas. Biomass Bioenerg. 21:133-142.

Savovaa, D., E. Apakb, E. Ekinci, F. Yardimb, N. Petrov, T. Budinovaa, M. Razvigorovaa, and V. Minkovaa. 2001b. Biomass conversion to carbon adsorbents and gas. Biomass Bioenerg. 21:133-142.

Sciban, M., B. Radetic, Z. Kevresan, and M. Klasnja. 2007. Adsorption of heavy metals from electroplating wastewater by wood sawdust. Bioresour. Technol. 98:402-409.

Segal, L., J.J. Creely, A.E. Martin, and C.M. Conrad. 1959. An empirical method for estimating the degree of crystallinity of native cellulose using the X-ray diffractometer. Textile Res. J. 29:786-794.

Sevilla, M., and A.B. Fuertes. 2009. The production of carbon materials by hydrothermal carbonization of cellulose. Carbon 47:2281-2289.

Shrestha, G., S.J. Traina, and C.W. Swanston. 2010. Black carbon's properties and role in the environment: a comprehensive review. Sustainability 2:294-320.

Smernik, R.J. 2009. Biochar and sorption of organic compounds, p. 289-300, *In* J. Lehmann and A. Joseph, eds. Biochar for Environmental Management: Science and Technology. Earthscan, London.

Spokas, K.A., W.C. Koskinen, J.M. Baker, and D.C. Reicosky. 2009. Impacts of woodchip biochar additions on greenhouse gas production and sorption/degradation of two herbicides in a Minnesota soil. Chemosphere 77:574-581.

Srivastava, S., K.C. Bhainsa, and S.F. D'Souza. 2010. Investigation of uranium accumulation potential and biochemical responses of an aquatic weed Hydrilla verticillata (L.f.) Royle. Bioresour. Technol. 101:2573-2579.

Suhas, P.J.M.C., and M.M.L.R. Carrott. 2007. Lignin-from natural adsorbent to activated carbon: A review. Bioresour. Technol. 98:2301-2312.

Tan, W.T., S.T. Ooi, and C.K. Lee. 1993. Removal of Cr(VI) from solution by coconut husk, palm pressed fibers. Environ. Technol. 14:277–282.

Titirici, M.M., A. Thomas, and M. Antonietti. 2007. Back in the black: hydrothermal carbonization of plant material as an efficient chemical process to treat the CO_2 problem. New J. Chem. 31:787-789.

Vandenhovea, H., A. Cuypersb, M.V. Heesa, G. Koppenc, and J. Wannijna. 2006. Oxidative stress reactions induced in beans (Phaseolus vulgaris) following exposure to uranium. Plant Physiol. Bioch. 44:795-805.

Varhegyi, G., P. Szabo, F. Till, B. Zelei, M.J.J. Antal, and X. Dai. 1998. TG, TG-MS, and FTIR Characterization of high-yield biomass charcoals. Energ. Fuels 12:969-974.

Yu, X.Y., G.G. Ying, and R.S. Kookana. 2009. Reduced plant uptake of pesticides with biochar additions to soil. Chemosphere 76:665-671.

Zeng, H., A. Singh, S. Basak, K.-U. Ulrich, M. Sahu, P. Biswas, J.G. Catalano, and D.E. Giammar. 2009. Nanoscale Size Effects on Uranium (VI) Adsorption to Hematite. Environ. Sci. Technol. 43:1373-1378.

6. Summary, Implications, and Recommendations

This dissertation investigated the scaling of adsorption reactions in systems that involved uranium as a solute and iron oxide-rich media as the adsorbent. The primary objectives of this work were: 1) To synthesize and characterize iron oxide-coated sand (IOCS) and use it as a model system to perform U(VI) adsorption experiments. 2) To design and perform batch adsorption experiments and identify the key scaling parameters. 3) To implement the scaling procedure in surface complexation models and predict experimental results. 4) To compare the adsorption parameters between batch and column transport experiments using a model system and a natural media. 5) To decipher the causes for the adsorption discrepancies that exist between batch and column experimental modes. These objectives were addressed with a combination of experiments with synthetic media (iron oxide-coated sand), natural geomedia (Oak Ridge Reservation soil), and surface complexation modeling. Moreover, the dissertation assessed the adsorption properties of biochar obtained via hydrothermal carbonization (HTC) for U(VI) adsorption. Here, we made one of the first attempts to test the use of carbonized waste as a permeable reactive barrier material for uranium contaminated sites.

6.1 Summary

In Chapter 2 of the dissertation, the two common protocols to synthesize iron oxide-coated sand, a precipitation method where Fe was precipitated directly onto the sand in a single step, and an adsorption method where pure goethite was prepared in the first step and then adsorbed onto the sand in a second step were described in detail. Although neither of the methods produced a completely crystalline Fe coating, the precipitation method produced sands with larger portions of amorphous Fe than the adsorption method, with the fraction of amorphous Fe decreasing with increasing Fe content. Despite producing a less crystalline Fe coating, however, the precipitation method was a more efficient and less time-consuming method of preparing IOCS. The coated sands from both the systems were characterized using scanning electron microscopy, energy dispersive spectroscopy, X-ray diffraction, and selective Fe extraction.

In Chapter 3, the adsorption properties of the IOCS were assessed to identify the key scaling parameters in batch systems. U(VI) adsorption isotherms and pH adsorption edges were measured on three coated sands with Fe contents ranging from 0.04 to 0.3%. Experimentally, the adsorption of U(VI) onto the three sands was more comparable when normalized to surface area than when normalized to Fe content. We also examined the ability of several surface complexation models to predict our adsorption data. Although several different models could predict our data with a reasonable degree of accuracy, the model of Waite et al. (1994) predicted the complete range of data better than the other models we tested. As the model was developed for amorphous HFO, it also served as a test of the hypotheses that adsorption of U(VI) to both amorphous and crystalline Fe oxides is approximately the same after correcting for surface area. Two different methods of scaling adsorption models were examined, the traditional method wherein the surface area of the adsorbents were assumed and a hybrid method wherein the measured surface area of the adsorbents were used. Consistent with the experimental data, scaling the adsorption model on the basis of surface area was the best approach. These findings are significant because many common surface complexation models are parameterized solely on the basis of measured Fe content rather than both measured Fe content and measured surface area.

In Chapter 4, the dissertation addressed one of the most perplexing and yet unresolved problems of adsorption anomalies that exists between batch and column-derived distribution coefficients (K_d). Several previous studies have indicated the existence of these discrepancies, especially when U(VI) has been used as an adsorbate. In this study, we attempted to understand the causes of the above problem using both natural heterogeneous geomedia and a homogeneous synthetic adsorbent. The uncontaminated natural geomedia was obtained from the Oak Ridge Reservation (OR) and the synthetic media, iron oxide-coated sand (IOCS), was prepared in the laboratory. The OR soil and IOCS were used to perform adsorption experiments with U(VI) as a solute in both batch and column modes. Moreover, a multi-step column experiment was conducted to obtain an adsorption isotherm that could be juxtaposed with the batch adsorption isotherm. Efforts were made to maintain similar experimental conditions in both batch and column scenarios. In particular, to eliminate CO_2 contamination, all the experiments were conducted at a $pH < 5$. The results obtained from the batch and column experiments indicated a large discrepancy (>100%) in the adsorption capacity of U(VI) onto OR soil. Whereas, in the case of IOCS, the batch-derived and column-derived isotherm indicated similar adsorption capacity for U(VI). Further experiments were designed at understanding the effect of solid-to-solution ratio on U(VI) adsorption in the batch systems involving the adsorbents. The results indicated that the adsorption of U(VI) on to IOCS was found to be independent of soil-to-solution ratio, whereas the adsorption of U(VI) onto OR soil was highly dependent on soil-to-solution ratio. When adsorption is dependent on solid-to-solution ratio, multiple adsorption isotherms could be obtained. This could lead to the observed batch and column adsorption discrepancy.

In Chapter 5 of the dissertation, one of the first attempts to test the use of carbonized waste, biochar obtained via HTC, as a permeable reactive barrier material for U(VI) contaminated sites was probed. In the study, biochar was produced from switchgrass at 300°C in subcritical water and characterized using X-ray diffraction, Fourier transform infrared spectroscopy, scanning electron micrcoscopy, and thermogravimetric analysis. The physiochemical properties indicated that biochar could serve as an excellent adsorbent to remove uranium from groundwater. A batch adsorption experiment at the natural pH (~ 3.8) of biochar indicated an H-type isotherm with a maximum sorption capacity of 2 mg g^{-1}. The adsorption process was highly dependent on the pH of the system. An increase towards circumneutral pH resulted in the maximum U(VI) adsorption of ca. 4 mg g^{-1}. The results indicated a strong relationship between the speciation of U(VI) and its adsorption onto biochar. Our study demonstrated that biochar could be used as an effective adsorbent medium for U(VI). Overall, the biochar produced via HTC is environmentally benign, carbon neutral, and efficient in removing U(VI) from groundwater.

6.2 Implications and recommendations

An assessment of the existing protocols to synthesize iron oxide coated-sand indicated that the sands from precipitation method would produce Fe coated media that would resemble natural material found at Department of Energy (DOE) sites. It has been reported that many of the DOE sites contain both crystalline and amorphous forms of iron oxides. Hence, sands from the precipitation method, which can be manipulated to produce different levels of iron oxide, can serve as a reasonable surrogate to represent natural iron oxide-coated geomedia for future studies that would aim at understanding field scale U(VI) transport. Moreover, our study indicated that a surface complexation model, although originally developed for U(VI) adsorption onto amorphous Fe oxide, can be tweaked to capture the differences in adsorption when adjusted for the surface area. Our results support one of the two methods adopted for modeling the adsorption processes at some U(VI) contaminated sites, namely the general composite (GC) method. Since many of U(VI) contaminated sites are rich in Fe-oxide coated geomedia, our method of using the measured surface area normalized to Fe content could serve as a reasonable approximation to predict those adsorption processes.

The results from the studies that addressed the batch-column adsorption discrepancy suggest that the frequently observed adsorption discrepancy between batch and column setting exists in systems containing highly heterogeneous adsorbents. Since in the case of heterogeneous adsorbents, reactions that would interfere with a hard metal like uranium would prevail (e.g., a multitude of sorption surfaces or dissolution of ligands that would interfere in U(VI) adsorption reaction etc.) that could result in adsorption being dependent on solid-to-solution ratio. Hence, scaling of adsorption processes that involves a strongly interacting solute like uranium should be done after thoroughly assessing the adsorption properties of the natural geomedia at different experimental conditions. Although the interactions of U(VI) and Fe-coated sands were used as representative adsorbate and adsorbent, the general principles may be applicable to other adsorbate-adsorbent systems well.

Since the ever increasing growth of biorefineries is expected to produce huge amounts of lignocellulosic biochar as a byproduct, its application as a permeable reactive barrier medium would help solve both carbon sequestration and contaminant remediation issues. The dissertation demonstrated the potential of biochar obtained via HTC as a uranium adsorbent media. Though our results indicate that biochar obtained via HTC can be used to adsorb uranium as is, future studies could focus on studying the adsorption properties of this carbonized media after activation and optimizing the experimental conditions for U(VI) adsorption.